1-1-2014

Development Of Silicon-Based Anodes And In-Situ Characterization Techniques For Lithium Ion Batteries

Jinho Yang
Wayne State University,

Recommended Citation

Yang, Jinho, "Development Of Silicon-Based Anodes And In-Situ Characterization Techniques For Lithium Ion Batteries" (2014). *Wayne State University Dissertations.* Paper 1034.

DEVELOPMENT OF SILICON-BASED ANODES AND IN-SITU CHARACTERIZATION TECHNIQUES FOR LITHIUM ION BATTERIES

by

JINHO YANG

DISSERTATION

Submitted to the Graduate School

of Wayne State University,

Detroit, Michigan

in partial fulfillment of the requirements

for the degree of

DOCTOR OF PHILOSOPHY

2014

MAJOR: ELECTRICAL ENGINEERING

Approved by:

Advisor Date

DEDICATION

To my family.

ACKNOWLEDGEMENTS

First of all, I would like to acknowledge my advisor Prof. Mark Ming-Cheng Cheng. He has provided me with great opportunities, environments, and insights for doing research. I appreciate him being stern and letting me know what I was doing wrong. Additionally, I appreciate him giving me input with which I could confront my mistakes. Prof. Cheng has been a supportive mentor during my PhD career with his enthusiasm and passion to my research. I would not be who I am without you.

I would like to thank our team members of Prof. Cheng's lab: Hyeun Joong Yoon, Xuebin Tan, Jing Yang, Chad Huard, Wasif Khan, Peng Zeng, Wenwen Yi, Ali Shahini, Ehsan Majidi, Jimmy Ching-Ming Chen, Nirul Masurkar, and Ramandeep Singh. I especially thanks to my former senior, Hyeun Joong Yoon, who helped me to settle in Michigan when I started here in 2010. All of the other lab members have been a great team to work with. They shared their perspective and helped me to solve many problems. You guys are my best friends. Jimmy Ching-Ming Chen deserves special thanks for helping me to build a model analysis and to fabricate a home-made cell chamber for the in-situ measurements presented in this thesis.

I would like to thank Dr. Simon Ng and Dr. Steven Salley from the Alternative Energy Technology Laboratory at Wayne State University. I am honored to collaborate with them on the development of the next generation anode materials. Rhet de Guzman is their former graduate student. We have collaborated on many works from journal articles to conference papers.

I also want to thank Bill Funk and Dan Durisin for their assistance in using the nFab facility. I thank to Chris Thrush for the operation of XPS and Li Li for AFM imaging. Thanks to Dr. Yong Xu for the help of Parylene deposition system. Thanks to Dr. Mike Mei from CIF for an operational assistance of SEM. Thanks to Polytec Inc. and TESCAN Inc. for the vibration test and the access of FIB and TEM, respectively. I also would like to thank all of my committee members, Dr. Simon Ng, Dr. Yong Xu, and Dr. Amar Basu for giving me great suggestions about experimental approaches.

I would like to thank my parents, Chang Soo Yang and Young Hwa Jang who supported me throughout my PhD career. None of these accomplishments would have been possible without their sincere care. Thanks to my whole family, my sisters, and my parents-in law. They have always encouraged me to stay motivated. Lastly, I owe my special thanks to my lovely wife, Aeri Chang standing next to me and embracing me whenever and wherever I am. Four and half years of my career has been enriched by her devotion. You are my power source. I love you.

TABLE OF CONTENTS

Dedication ii

Acknowledgements iii

List of Tables ix

List of Figures x

CHAPTER 1. INTRODUCTION 1

- 1.1 Energy storage systems 1
- 1.2 Battery technology 3
- 1.3 Lithium ion batteries 5

CHAPTER 2. DEVELOPMENT OF HIGH PERFORMANCE ANODES 9

- 2.1 Challenges of Si anodes 9
- 2.2 Literature review of Si-based anodes 11
  - 2.2.1 Bulk silicon vs. Si nano-scale particles and thin film anodes 11
  - 2.2.2 Nanostructured Si anodes 12
  - 2.2.3 Si-Carbon composite anodes 13
  - 2.2.4 Patterned Si thin film anodes 14
  - 2.2.5 Si-N composite anodes 17

CHAPTER 3. ENGINEERING SILICON-RICH NITRIDE ANODES 20

3.1 Introduction 20

3.2 Plasma enhanced chemical vapor deposition (PECVD) technique 21

3.3 Experimental 22

3.3.1 Preparation of Cu current collectors 22

3.3.2 Preparation of anode materials 24

3.3.3 Surface characterization 24

3.3.4 Cell assembly and testing 27

3.4 Results and discussion 27

3.4.1 PECVD silicon nitride for a high-performance lithium ion battery anode 27

3.4.2 Controlling deposition conditions (process temperature) 30

3.4.3 Controlling deposition conditions (RF power) 33

3.4.4 Surface effect of the current collectors 39

3.4.5 Thickness effect in the anode materials 43

CHAPTER 4. DEVELOPMENT OF IN-SITU CHARACTERIZATION SYSTEMS 47

4.1 Literature review of the stress measurement in lithium ion battery anodes 47

4.2 Measurement system (white light interferometry) 50

4.3 Experimental 51

4.4 Analysis model 53

CHAPTER 5. IN-SITU NANOMECHANICAL CHARACTERIZATION OF SILICON THIN FILMS ON ROUGHENED CURRENT COLLECTORS FOR LITHIUM ION BATTERY APPLICATIONS.........57

5.1 Introduction.........57

5.2 Experimental.........58

5.3 Results and discussion.........60

CHAPTER 6. IN-SITU STRESS MEASUREMENTS WITH THE CRACK OBSERVATION.........68

6.1 Introduction.........68

6.2 Experimental.........68

6.3 Results and discussion.........70

CHAPTER 7. IN-SITU MONITOR ELECTROCHEMICAL PROCESSES IN BATTERIES USING VIBRATING MICROCANTILEVERS.........78

7.1 Introduction.........78

7.2 Experimental.........79

7.3 Design.........79

7.4 Results and discussion.........81

CHAPTER 8. CONCLUSIONS AND FUTURE SUGGESTIONS.........84

8.1 Conclusions.........84

8.2 Future suggestions 86

8.2.1 Development of silicon nitride anodes 86

8.2.2 In-situ characterization technologies 87

Bibliography 89

Abstract 107

Autobiographical statement 109

LIST OF TABLES

Table 1.1 Characteristics of BEVs, HEVs, and FCEVs [5]. 2

Table 3.1 Atomic concentration (%) of elements of amorphous SiN_x films on a pristine, mechanically-scratched, and $FeCl_3$-etched copper substrates and *a*-Si film on a $FeCl_3$-etched copper substrate before cycling. 25

Table 3.2 Atomic concentration (%) of elements of amorphous SiN_x films deposited at 100 ℃, 200 ℃, and 300 ℃ before cycling. 31

Table 3.3 Atomic concentration (%) of elements of amorphous SiN_x films deposited at 25W, 50W, and 100W before cycling...34

LIST OF FIGURES

Figure 1.1 Comparison of the different battery technologies in terms of volumetric and gravimetric energy density [14]. 4

Figure 1.2 Schematic illustration of a conventional lithium ion battery showing charge/discharge process [21]. 6

Figure 1.3 Schematic illustration of the AAA layer staking and αα interlayers of the intercalated lithium atoms [22]. 6

Figure 2.1 (a) cycling performance of silicon nanofilm, nanoparticle, bulk silicon, and graphite [47]. (b) SEM image of the Si thin film after cycling [61]. 12

Figure 2.2 Schematic diagram of morphological changes in (a) nano-scale particle or thin film Si anodes, and (b) Si NWs during electrochemical cycling. (c) Cycling performances of Si NWs, Si nanocrystals (NCs), and graphite anodes [42]. 13

Figure 2.3 (a) Cycling performance of the Si-fullerene (C_{60}) composite anodes and SEM images of the anodes (b) bare Si and (c) C_{60} coated Si after 25 cycles [73]. 14

Figure 2.4 (a) Cycling performance of 100, 200, and 500nm *a*-Si thin film [90], (b) SEM morphology of the Si thin film anode after 12 cycles [46]. 15

Figure 2.5 (a) Schematic diagram of lithiated Si film on Cu substrate. (b) Minimum crack spacing that no longer additional crack is created [46]. 17

Figure 2.6 (a) SEM image of 40µm pattern size, (b) 17µm pattern size, and (c) 7µm pattern Si patches after cycling size [46]. 17

Figure 2.7 Cycling performance of 200 nm thick (a) *a*-Si, (b) $Si_{0.76}N_{0.24}$, and (c) $Si_{0.59}N_{0.41}$ thin films at 0.5 C rate. 18

Figure 2.8 Cycling performance of $SiN_{0.92}$ films for the thickness of 200 nm and 500 nm. 19

Figure 3.1 Schematic diagram of a PECVD reactor for SiO_xN_y film deposition [100]. 22

Figure 3.2 AFM micrographs of (a) a pristine Cu foil, (b) a mechanically-scratched Cu foil, and (c) a Cu foil etched with $FeCl_3$. (d) The root mean square average roughness (R_q) of each sample has been quantified. 23

Figure 3.3 The high resolution XPS spectra of Si 2p of (a) PECVD *a*-Si and (b) PECVD nitride. 26

Figure 3.4 The voltage profiles during 50 cycles for (a) evaporated *a*-Si and (b) PECVD *a*-Si, and (c) PECVD nitride. (d) The cycling performance of three samples. 28

Figure 3.5 The high resolution N 1s spectra of the Si-rich nitride anode (a) before cycle, and (b) after 100 cycles. 29

Figure 3.6 Nyquist plots of (a) evaporated *a*-Si and (b) PECVD nitride anodes during 300 cycles. 30

Figure 3.7 XPS spectra of 250 nm SiN_x films deposited at (a) 100, (b) 200, and (c) 300 ℃ in the PECVD. 31

Figure 3.8 The high resolution XPS spectra of the Si 2p for PECVD nitride deposited (a) at 100 ℃, (b) 200 ℃, and (c) 300 ℃. (d) The cycling performance of three samples grown at different temperatures. 32

Figure 3.9 SEM images of 250 nm SiN_x films deposited (a) at 100 ℃ in the PECVD after 100 cycles, and (b) after 300 cycles, (c) at 200 ℃ in the PECVD after 100 cycles, and (d) after 300 cycles, (e) at 300 ℃ in the PECVD after 100 cycles, and (f) after 300 cycles. All the films were deposited on the etched Cu. 33

Figure 3.10 XPS spectra of 250 nm SiN_x films deposited at plasma power of (a) 25, (b) 50, and (c) 100 W in the PECVD. 35

Figure 3.11 The high resolution XPS spectra of the Si 2p for PECVD nitride deposited (a) at 25 W, (b) 50 W, and (c) 100 W. (d) The cycling performance of three samples grown at different plasma RF powers. 35

Figure 3.12 SEM images of 250 nm SiN_x films deposited (a) at 25 W in the PECVD after 100 cycles, and (b) after 300 cycles, (c) at 50 W in the PECVD after 100 cycles, and (d) after 300 cycles, (e) at 100 W in the PECVD after 100 cycles, and (f) after 300 cycles. All the films were deposited on the etched Cu. 36

Figure 3.13 (a) The cycling performances of 250 nm thick evaporated *a*-Si and PECVD nitride during 300 cycles. (b) A TEM image of PECVD nitride after 300 cycles. 37

Figure 3.14 The SEM images of PECVD nitride films (a) before cycling, (b) after 30 cycles, (c) after 100 cycles, and (d) after 300 cycles. 38

Figure 3.15 An adhesion test using a scotch tape of (a) PECVD *a*-Si, (b) evaporated *a*-Si, and (c) PECVD nitride on a pristine copper foil. 38

Figure 3.16 Cyclic performance of the *a*-Si anodes on the pristine (black), scratched (blue), and FeCl3-etched (red) Cu substrates. 39

Figure 3.17 SEM images of a 250 nm SiN_x film (a) before cycling, (b) after 1st charge, (c) after 30 cycles, and (d) after 100 cycles on a pristine Cu substrate, (e) before cycling, (f) after 1st charge, (g) after 30 cycles, and (h) after 100 cycles on a mechanically-scratched Cu substrate, (i) before cycling, (j) after 1st charge, (k) after 30 cycles, and (l) after 100 cycles on a $FeCl_3$-etched Cu substrate. 41

Figure 3.18 (a) Cyclic voltammogram (scanning rate, 0.2 mVs^{-1}) and (b) Cyclic performance of SiN_x anode on a $FeCl_3$-etched Cu cycled at 1C rate. 42

Figure 3.19 The cycling performances of 250 nm, 500 nm, and 1 µm PECVD nitride anodes during 100 cycles. All three films were deposited at 25 W power and 100 ℃. 43

Figure 3.20 SEM images of (a) 250 nm SiN_x films after 30 cycles, (b) after 100 cycles, and (c) after 300 cycles, (d) 500 nm SiN_x films after 30 cycles, (e) after 100 cycles, and (f) after 300 cycles, (g) 1 µm SiN_x films after 30 cycles, (h) after 100 cycles, and (i) after 300 cycles. All the films were deposited on the etched Cu. 44

Figure 3.21 Cyclic performances of 500 nm SiN_x films depending on the C-rate (0.5C and 1C). 45

Figure 3.22 SEM images of 500 nm SiN_x films (a) tested at 0.5C, and (b) tested at 1C upon 300 cycles. 45

Figure 4.1 Voltage and stress profiles at cut-off voltages of (a) 0-1.5V, and (b) 0.1-1.5V. Inner box in (a) is cyclic voltammetry. 48

Figure 4.2 (a) A schematic diagram of the electrochemical cell and the MOS setup. (b) Voltage profiles and (c) stress variation profiles [92]. 50

Figure 4.3 Schematic diagram of a WLI system [117]. 51

Figure 4.4 Fabrication process of the bilayered cantilever (*a*-Si on copper). 52

Figure 4.5 Measurement setup of the in-situ measurement system. (a) SEM of the cantilever anode, (b) Top view of the customized electrochemical cell, (c) White light interferometry and chronopotentiometry setup. 53

Figure 4.6 The bending of the bilayer cantilever during lithiation and delithiation. (σ_c: compressive stress, σ_t: tensile stress) 54

Figure 4.7 3D interferometry images of the cantilever anodes during the first cycle. 56

Figure 5.1 The adhesion tests (scotch tape) of the *a*-Si films on (a) the pristine copper and (b) $FeCl_3$-etched copper. 60

Figure 5.2 (a) The voltage and (b) in-situ stress profiles of the *a*-Si films on the pristine (black) and $FeCl_3$-etched copper (red) cantilevers in the liquid cell chamber. 61

Figure 5.3 (top) The voltage and (bottom) in-situ stress profiles of the *a*-Si film on the $FeCl_3$-etched copper during 5 cycles. 63

Figure 5.4 The SEM images of (a) the *a*-Si film on the pristine copper cantilever after 1 cycle and (b) the film on the $FeCl_3$-etched copper cantilevers after 5 cycles. 65

Figure 5.5 The electrochemical properties of the evaporated *a*-Si films on the (a) pristine copper , and (b) $FeCl_3$-etched copper, cycled at a rate of 2 A/g (1C) between 0.02 V and 2.0 V vs. Li^+/Li in the coin cell. (c) Cycle performances of the a-Si anodes on two different types of copper substrates upon 50 cycles. 65

Figure 5.6 (a) A schematic diagram of degradation processes of the *a*-Si anodes. The SEM images of 250 nm evaporated *a*-Si films (b) on the pristine copper and (c) $FeCl_3$-etched copper before cycling, after 1^{st} lithiation, and after 10 cycles. 67

Figure 6.1 The measurement setup with the cell configuration and the 3D interferometry images before and after lithiation. Surface heights are depicted by the colors on the vertical height scale on the right side. 69

Figure 6.2 The voltage and in-situ stress profiles of a 40 nm thick *a*-Si film on a pristine Cu during 5 cycles. (inset) The cycling performance upon 5 cycles. During the initial three cycles, the potential window was set from 0.05 V to 1 V. During the rest of cycles, the potential window was set from 0.01 V to 2 V. 71

Figure 6.3 SEM images of the 40 nm thick *a*-Si film after 5 cycles. 73

Figure 6.4 (left) Voltage and in-situ stress profiles of a 250 nm thick *a*-Si film on the pristine Cu during the first cycle. (right) Optical images corresponding to certain points (a-f) at state of charge and discharge. The potential window was set from 0.02 V to 2 V. 75

Figure 6.5 (left) Voltage and in-situ stress profiles of a 500 nm thick *a*-Si film on the pristine Cu during the first cycle. (right) Optical images corresponding to certain points (a-f) at state of charge and discharge. The potential window was set from 0.02 V to 2 V. 76

Figure 7.1 The measurement setup of the vibration test. 79

Figure 7.2 (top) Working principle of a conventional LIB (bottom) In-situ monitoring the frequency shift of vibrating microcantilevers made of battery materials on cooper. 81

Figure 7.3 The vibration magnitude at different charge times. The first mode was 18kHz shift to 16kHz during the first charge. 82

Figure 7.4 (top) The first charge curve of a silicon anode (bottom) The in-situ measurement by monitoring the frequency shift caused by the mass changes. 82

CHAPTER 1. INTRODUCTION

1.1 Energy storage systems

In order to reduce environmental pollution and petroleum consumption for transportation, a number of studies have been conducted into the development of advanced vehicles using renewable energy sources, including battery electric vehicles (BEVs), hybrid electric vehicles (HEVs), and fuel cell electric vehicles (FCEV) [1, 2]

BEVs have a pure electrical power source for the propulsion of the vehicles, replacing internal combustion engines (ICEs). Although the BEVs are more desirable for consumers, there are several disadvantages including high cost, short driving range, long recharging time, and heavy weight. For instance, Nissan Leaf is a BEV that is commercially available today. It costs around $35,000, has a range of 115 mi/charge, and the battery must be charged over night.

HEVs utilize both batteries and ICEs for the propulsion of the vehicles. During acceleration, the electric motor supplements the output of the ICE. The ICE stops when the vehicle moves at low speed or is stopped. Some electric energy is recovered during the braking process [3]. HEVs are suitable for long distance driving. The Toyota Prius is an example of a popular HEV with a fuel efficiency of around 50 mile/gal. One of the disadvantages of HEVs is that the design of two motors requires a complex system for the management.

FCEVs generate electrical energy from hydrogen. Since the byproduct of a hydrogen fuel cell is water, FCEVs provide a clean operational environment. However, current FCEVs still have disadvantages such as high cost and refueling infrastructure [4]. The major characteristics of these three types of vehicles are shown in Table 1.1 [5].

Types of EVs	**BEVs**	**HEVs**	**FCEVs**
Propulsion	**◆ Electric motor drives**	**◆ Electric motor drives** **◆ Internal combustion engines**	**◆ Electric motor drives**
Energy system	**◆ Battery** **◆ Ultracapacitor**	**◆ Battery** **◆ Ultracapacitor** **◆ ICE generating unit**	**◆ Fuel cells** **◆ Need battery/ultra-Capacitor**
Energy source & infrastructure	**◆ Electric grid charging facilities**	**◆ Gasoline stations** **◆ Electric grid charging facilities (for PHEV)**	**◆ Hydrogen** **◆ Hydrogen production and transportation infra -structure**
Characteristics	**◆ Zero emission** **◆ High energy efficiency** **◆ Independence on crude oils** **◆ Relatively short range** **◆ High initial cost** **◆ Commercially available**	**◆ Very low emission** **◆ Higher fuel economy as compared with ICE vehicles** **◆ Long driving range** **◆ Dependence on crude oils (for non PHEV)** **◆ Complex** **◆ Commercially available**	**◆ Zero emission or ultra low emission** **◆ High energy efficiency** **◆ Independence on crude oils** **◆ Satisfied driving range** **◆ High cost** **◆ Under development**
Major issues	**◆ Battery and battery management** **◆ Charging facilities** **◆ Cost**	**◆ Multiple energy sources control** **◆ Battery sizing and management**	**◆ Fuel cell cost, cycle life and reliability** **◆ Hydrogen infrastructure**

Table 1.1 Characteristics of BEVs, HEVs, and FCEVs [5].

All three of these vehicle types require a good energy storage system. Batteries are currently the most common option for energy storage systems in motor vehicles [6-8].

However, the major hurdle for the electrification of road transportation is the insufficient capacities of current batteries, limiting the driving range of practical electric vehicles.

1.2 Battery technology

A battery is an electrochemical cell that converts chemical energy into electrical energy, which was invented by Alessandro Volta in 1800. In recent years, batteries have played a significant role in many electronic applications [9]. There are two types of batteries. One type is a primary battery, which can be used only once. Common primary batteries include zinc-carbon batteries, alkaline batteries, and lithium batteries. Primary cells cannot be recharged, because the chemical reactions are not reversible and active materials may not return to their original states [10]. The other type is secondary batteries, which can be charged and discharged multiple times. Common rechargeable batteries include lead-acid batteries, nickel-cadmium, nickel-metal hydride batteries, and lithium ion batteries.

The oldest type of rechargeable battery is a lead-acid battery. It has been widely used in automobiles for lighting and ignition systems, because of its low cost, good shelf life, and ease of manufacturing [11]. However, the drawbacks of lead-acid batteries include their relatively heavy weight and a limited range of temperatures for operation.

A nickel-cadmium battery (NiCd) uses metallic cadmium as the negative electrode and nickel oxihydroxide (NiOH) as the positive electrode. This battery is suitable for high power electronics, which require high discharge rates due to their relatively low internal resistance [10]. However, this type of battery has a low energy density and environmental hazard because of cadmium’s toxicity. Nickel-metal hydride (NiMH) batteries were developed by replacing the cadmium on the electrode with hydrogen absorbing alloys. Commercial hybrid vehicles currently use NiMH batteries to enhance their gas mileage. NiMH batteries have a high volumetric energy density (up to 420 Wh l^{-1}) but a relatively lower gravimetric energy density (80 Wh kg^{-1}). They are also cheaper than NiCd batteries [12, 13]. However, one significant disadvantage of NiMH batteries is a high self-discharge rate due to electrochemical processes within the cell.

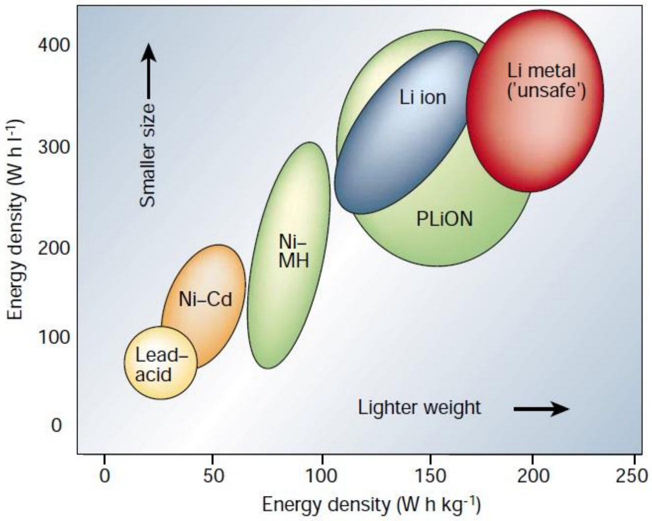

Figure 1.1 Comparison of the different battery technologies in terms of volumetric and gravimetric energy density [14].

To reach the goal of high specific energy and power for rechargeable batteries, the functional materials are required to have high a specific charge capacity (i.e. a high number of charge carriers per mass). The cell voltage is the potential difference between the cathode and the anode. Therefore, a high redox potential for the positive electrode and a low potential for the negative electrode is desirable. In order to maintain a high efficiency for rechargeability (known as Columbic efficiency), the electrode materials have to be reversibly recovered to sustain the specific charge for hundreds of cycles. Commercially available lithium ion batteries (LIBs) have a high specific energy (100-250 Wh kg^{-1}), high specific power (250-340 W kg^{-1}), and a high energy efficiency (80-90%), compared to other types of batteries as shown in Figure 1.1 [14]. On the other hand, LIBs have disadvantages of temperature dependent performance, fire hazard, and high cost [15]. Many researchers have been investigating these issues. More detailed properties of LIBs will be given in the next subsection.

Other advanced lithium batteries have also been investigated including lithium air batteries (Li-air) and lithium-sulfur (Li-S) batteries. In traditional Li-air batteries, one of the electrodes (cathode) is an interface with the air and the other electrode (anode) is a metallic lithium. During the charging (Li insertion into cathode), an oxidation reaction occurs at the anode, in which electrons flow to the cathode through an external circuit, and Li ions reduce oxygen to form Li_2O_2 in the cathode. This reaction is reversed during discharging (Li extraction from cathode). However, there are also non-reversible side reactions such as the formation of LiO_2. Li-air batteries have larger energy density (1700 Wh kg^{-1}) compared with other batteries, such as Lead-acid (40 Wh kg^{-1}), NiMH (50 Wh kg^{-1}), Zinc-air (350 Wh kg^{-1}), and Li-ion (160 Wh kg^{-1}) [16]. However, the main challenge in commercializing Li-air batteries lies in preventing the material from interacting with the environment, which causes degradation of the cathode and capacity fading. Recently, Li-S batteries have been considered as an alternative choice for next generation rechargeable batteries due to the abundance and low cost of sulfur as well as their high theoretical energy density (2600 Wh kg^{-1}) [17]. However, Li-S batteries have not been commercialized yet due to many issues including short cycle life, low efficiency, and a high self-discharge rate, which are related to the dissolution of the sulfur reduction elements in liquid electrolyte [18].

1.3 Lithium ion batteries

Nowadays, LIBs are the most popular rechargeable batteries for both portable electronics and electric vehicles. Figure 1.2 shows the details of charge/discharge process in a LIB. The three functional components are an electrolyte, anode, and cathode. The liquid electrolyte is typically a mixture of organic carbonates, such as ethylene carbonate or diethyl carbonate, which contain complexes of solid lithium-salts such as $LiPF_6$, $LiBF_4$, or $LiClO_4$ [19] . The electrolyte plays an important role as a medium for Li ion transport and many efforts have been made to prevent oxidation and minimize internal resistance of the electrolyte [20].

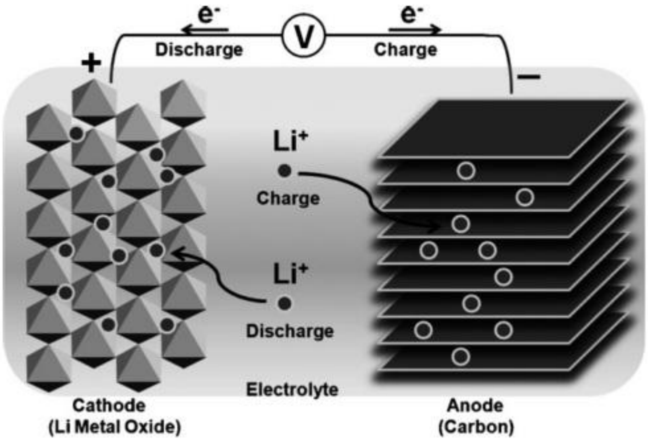

Figure 1.2 Schematic illustration of a conventional lithium ion battery showing charge/discharge process [21].

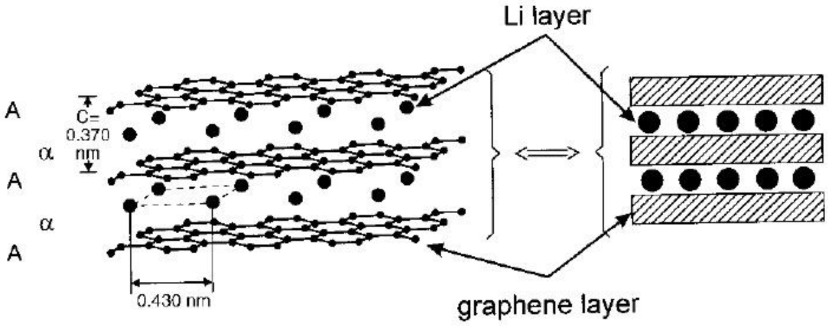

Figure 1.3 Schematic illustration of the AAA layer staking and αα interlayers of the intercalated lithium atoms [22].

The most popular material for negative electrode (anode) is graphite. Graphite is a carbonaceous structure composed of multiple layers of graphene. The host material, graphite, is subjected to a solid-state redox reaction, including electron transfer coupled with insertion of Li ions from an electrolyte into the solid host. This process is also called intercalation. One Li atom per six carbon atoms forms crystalline graphitic carbons (LiC_6), equivalent to a theoretical capacity of 372 mAh g^{-1} [23-25]. During the intercalation process, each graphene layers position to AAA as shown in Figure 1.3 [22]. The interlayer distance among the graphene planes slightly increases. The lithium atoms then shift to the αα position.

The positive electrode (cathode) is generally one of the materials: a layered oxide such as $LiCoO_2$, a polyanion such as $LiFePO_4$, a spinel such as $LiMn_2O_4$, or a LiNiMnCo (NMC) [26]. These lithium intercalation compounds are formed by the insertion of Li atoms between the slabs of the host materials. The Li ions are extracted from the compounds during the oxidation, which electrons flow to the anode. The reactions at both the anode and the cathode have to be reversible to maintain the specific energy during multiple cycles. Half reactions for each electrode are as follows,

Cathode: $LiCoO_2 \leftrightarrow xLi^+ + Li_{(1-x)}CoO_2 + xe^-$

Anode: $C + xLi + xe^- \leftrightarrow Li_xC$

A supplementary component such as a separator is placed between the anode and the cathode in order to prevent a short circuit. The polymer separator in the LIB consists of many pores, which are uniformly distributed to ensure a uniform current distribution through the surface of the permeable membrane.

LIB can be manufactured in various formats, such as cylindrical cells, pouch cells, and prismatic types. Cylindrical and pouch type cells are commonly used in portable devices. Prismatic type cells are used in electric vehicles. Hundreds of battery cells are connected in series and parallel to increase the voltage (for a single cell: ~3.6V) to power the vehicles. One of the issues for LIBs' applications in electrical cars is thermal runaway if they are overheated or overcharged [27]. The rise in temperature can cause mechanical failures of the cells, short circuits, early death of the cell by distortion, swelling, and burst of the cell. Another issue is dendrite formation, which leads to a short circuit between the anode and the cathode. The deposition of lithium salts on anode potentially ascribes to non-uniform current distributions. The dendrites eventually cause a serious safety hazard [28, 29]. To reduce these risks, safety management systems are installed, and they shuts down the battery when its voltage reaches beyond the safe range (3.0–4.2 V) [28].

CHAPTER 2. DEVELOPMENT OF HIGH PERFORMANCE ANODES

2.1 Challenges of Si anodes

There are growing research interests in the development of LIBs with high energy and power densities. Silicon is an attractive candidate for the anode material thanks to its low discharge potential (<0.4 V) and high specific capacity (theoretical capacity 4200 mAh g^{-1}) [30-32]. The main challenge in implementing a silicon anode is its material degradation associated with huge volume expansion (>300%) during the lithiation/delithiation process. The mechanical stress, the material pulverization and electrical contact loss cause mechanical instability and poor cyclic performance [33-38]. The reaction of lithium and silicon is an intermetallic alloying process ($Li_{4.4}Si$), which experiences much larger volume changes (~400%) than the intercalation anodes, such as graphite anodes (LiC_6, ~10%).

Irreversible capacity loss: Although silicon anodes have a high specific capacity, an irreversible capacity loss is observed. The irreversible capacity loss is attributed to the following factors, including (1) the formation of a solid electrolyte interphase (SEI) on the surface of active material exposed to the electrolyte [22], (2) a loss of electrical contact due to large volume changes during electrochemical cycling, and (3) side reactions with surface oxide layers [39].

SEI formation: The SEI formation is attributable to the decomposition of the electrolytes at the interface between the electrode material and electrolyte. SEI comprises inorganic components such as salt degradation products and organic components such as reduction products of the electrolyte solvent [40]. In graphite anodes, the SEI layer is created during the first charging (lithium insertion) at the voltage range of 0.3-0.8 V [15]. When Li ions travel towards the anode through the electrolyte, they react with degradation products and form solid parts on the anode surface. Densely packed SEI prevents further formation of the solid parts and allows Li ions to access the anode. Once the SEI layer is formed on the graphite surface during the first cycle, no further formation occurs during the subsequent cycles. The SEI prevents another decomposition of electrolyte, contributing to a longer cycle life [15, 22]. In contrast, the SEI formation in silicon anodes (at 0.4-0.7 V) is inhomogeneous and a dynamic process of breakup and reformation over the cycles [41-43]. The SEI layers are damaged by the mechanical stress during Si-Li alloy formation. New SEI layers will be formed when the new silicon is exposed to the electrolyte. In order to reduce the irreversible capacity, nanotechnology has been used to minimize the fractures in anode materials [21, 41, 44-47].

Loss of electrical contact due to the mechanical stress: Owing to the large stress induced by continuous expansion and contraction in Si anodes, cracking and delamination of active materials lead to the disconnection of Si-Li alloys from the current collectors. During charging process (lithium insertion), the Si-Li alloys are under compressive stress due to the volume expansion. The silicon experiences the plastic deformation when the stress reaches the yield strength. At this point, the active material might be still intact unless the compressive stress is extremely high. During discharging process (lithium extraction), the Si-Li alloys experience large tensile stress due to the volume contraction, leading to the pulverization and the disconnection of the active materials from the substrates [48]. The disconnected Si particles or films will not allow the charge to transfer from the active material to the current collector [49], causing the irreversible capacity loss.

2.2 Literature review of Si-based anodes

2.2.1 Bulk silicon vs. Si nano-scale particles and thin film anodes

Several techniques have been proposed to overcome the structural damage of silicon during electrochemical cycles, including nano-scale particles [32, 50] or thin films deposition [51-53], nanostructured silicon [21, 44, 47], silicon-carbon composites [45, 54, 55], silicon-graphene composites [56, 57], silicon-metal composites [58, 59], patterning Si thin films [46, 60], etc. Nano-scale materials have been found to mitigate the large stresses associated with the volume changes during electrochemical alloying. This advantage contributes to better cyclic stability compared to the bulk silicon [47, 50, 52, 53, 61]. In addition, the morphologies of nanoscale Si can shorten the length of the diffusion pathway and improve Li reaction with large surface area of Si [62].

Graetz and coworkers compared cycling performance of silicon films, silicon nanocrystals (nanoparticles), bulk silicon, and graphite (Figure 2.1a) [47]. The thickness of Si films was 100 nm, and the size of the Si nanocrystals was 5-20 nm. Si nanocrystals was showen to have an initial charge capacity of 2400 mAh g^{-1} and a discharge capacity of 1000 mAh g^{-1}, having a reversible capacity of 525 mAh g^{-1} during 50 cycles. This performance was superior to the bulk Si anodes. The Si nanofilm showed the highest reversible capacity of ~1700 mAh g^{-1} among three types of silicon anodes. Si thin film anodes did not have inactive binders so they had higher specific capacity. Additionally, thin film deposition methods provided good uniformity and adhesion between the films and the current collectors, which maintained good electrical contact. Therefore, cycling stability and cycle life were improved [63]. However, the thin film anode still experienced the large stress, followed by disconnection of the films from the current collectors (Figure 2.1b) [61].

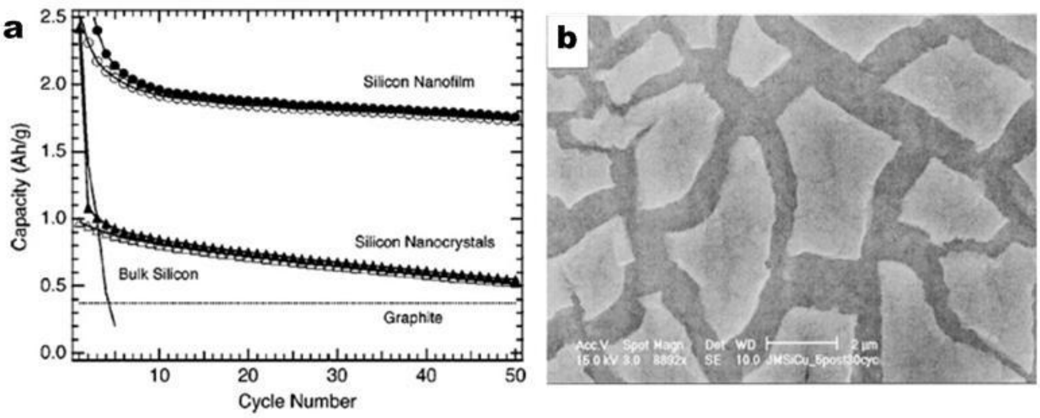

Figure 2.1 (a) cycling performance of silicon nanofilm, nanoparticle, bulk silicon, and graphite [47]. (b) SEM image of the Si thin film after cycling [61].

2.2.2 Nanostructured Si anodes

Nanostructured silicon anodes such as Si nanospheres and nanowires (NWs) are other promising candidates as high-energy electrode materials. Cui and coworkers reported that silicon nanowire anodes exhibited high discharge capacity (>3000 mAh g^{-1}) [42]. The Si nanowires of averaging 90 nm diameter were grown using a vapor-liquid-solid (VLS) method on the stainless steel current collector.

The NWs have several advantages, shown in Figure 2.2b. First, it was believed that the Si NWs were able to accommodate the volume changes by providing sufficient space [41, 64-67]. Second, each NW was directly connected to the metallic substrate, thereby minimizing the capacity loss. Finally, the 1D structure allowed efficient electron charge transport. The Si NW anodes exhibited a high specific capacity, as shown in Figure 2.2c. First charge capacity was shown to have 4277 mAh g^{-1}, which was comparable to the theoretical capacity (within experimental error). The first and second discharge capacity was 3124 and 3193 mAh g^{-1}, giving a Coulombic efficiency of 70 and 90%, respectively. Both charge and discharge capacities were consistent during several cycles with little capacity fading.

However, they showed only 10 cycles. For practical uses, batteries with high columbic efficiency of 99.995% over 1000 cycles are needed.

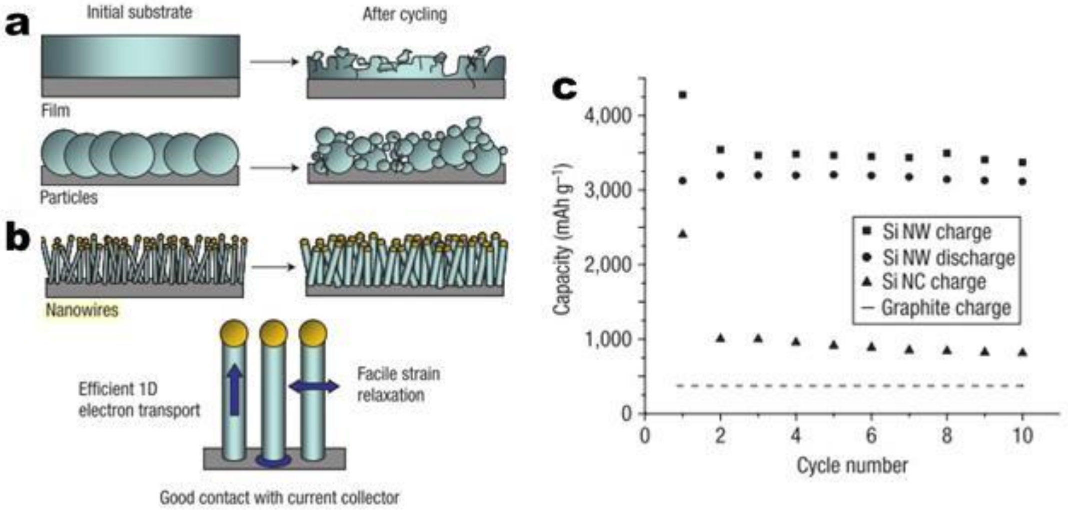

Figure 2.2 The schematic diagrams of morphological changes in (a) nano-scale particles or thin film Si anodes, and (b) Si NWs during electrochemical cycling. (c) Cycling performances of Si NWs, Si nanocrystals, and graphite anodes [42].

2.2.3 Si-Carbon composite anodes

Si-carbon composites have been investigated to enhance the electrochemical performance by using the carbon as a stress relaxation material [54, 68-78]. The carbon improves electrical conductivity. Moreover, the presence of the carbon coating on Si anodes limits the specific capacity, which reduces large stress induced by the volumetric increase of the composite material. Reduced stress may hinder the subsequent formation of SEI layers and maintain the structural stability during further cycling. Figure 2.3 shows SEM images of bare Si and fullerene C_{60}-coated Si after 25 cycles as well as the cycling performance of the bare Si and C_{60}-coated Si anodes. [73]. C_{60} (100nm) layers were coated onto the Si thin film (300 nm) anode by a plasma evaporation technique. The carbon coating dramatically improved the cycling performance, resulting in a reversible capacity of 3000 mAh g^{-1}. In the SEM images, the bare Si electrode had severe fractures on the surface after 25 cycles. On the other hand, no cracking or fractures were observed on the surface of the C_{60} coated sample. This improvement was ascribed to the polymeric layer of C_{60} preserving the electrochemical activity of the Si film during the lithiation/delithiation processes. However, the long-term cyclic stability still has not been demonstrated. Moreover, the fabrication process became significantly complicated because two different materials had to be synthesized.

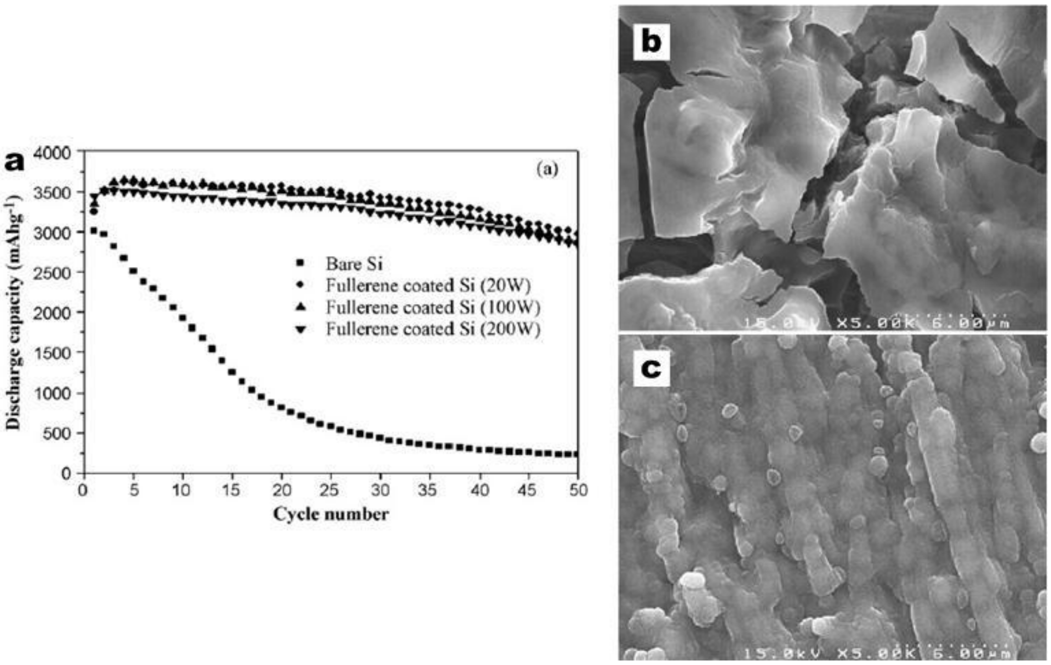

Figure 2.3 (a) Cycling performance of the Si-fullerene (C_{60}) composite anodes and SEM images of the anodes (b) bare Si and (c) C_{60} coated Si after 25 cycles [73].

2.2.4 Patterned Si thin film anodes

The cycling performance of Si thin film anodes has been demonstrated by a number of studies [53, 61, 79, 80]. Si thin film anodes are directly grown onto the current collectors using several deposition methods, including a low pressure CVD [81, 82], physical vapor deposition (PVD) [51, 80, 83, 84], E-beam evaporation [47, 85], and plasma enhanced CVD [86-89]. In addition, the thin film anodes are in uniform and intimate contact with the current collectors. The superior electrical contact provides the wide range of the electron pathway, which can enhance the specific energy density. On the other hand, powder-type anodes create the electron pathway from their surface to the current collectors. Therefore, the number of charge carriers per area is smaller than that of thin film anodes.

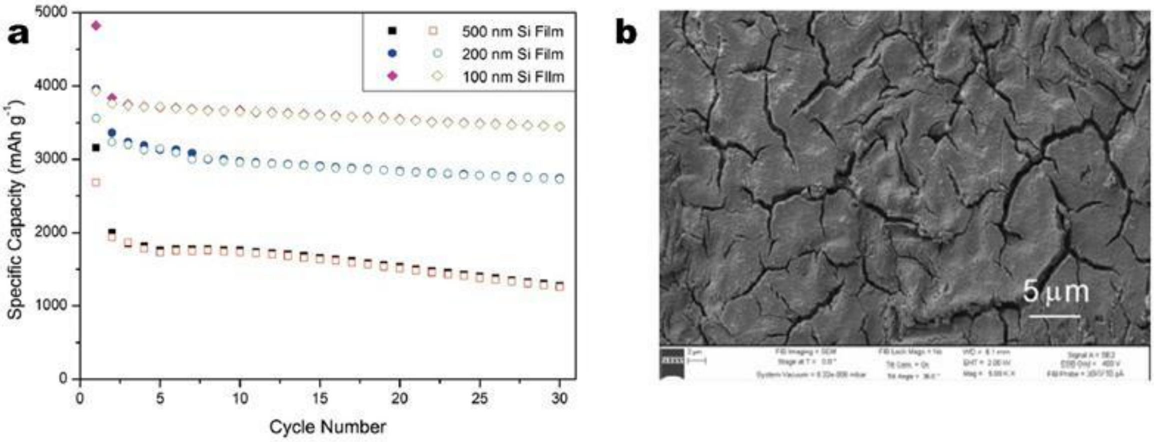

Figure 2.4 (a) Cycling performance of 100, 200, and 500nm *a*-Si thin film [90], (b) SEM morphology of the Si thin film anode after 12 cycles [46].

Li et al. reported the cycling performances of thin film anodes with three different film thicknesses [90]. It was believed that the thicker films had poor performance compared to thinner films due to the larger stress upon lithiation/delithiation, longer Li diffusion length, and higher film internal resistance [39]. Figure 2.4a shows cycling performances of 100 nm, 200 nm, and 500 nm thick films. The Si films with thicknesses of 100 nm and 200 nm showed higher reversible capacity and retention than the 500 nm films during 30 cycles. However, the large irreversible capacity loss still remained for all samples. This implies that the 100 nm thick film is not thin enough to accommodate the volume changes in the active material. Li et al. further suggested a direction of designing electrodes to minimize film cracks by patterning the electrodes. The pattern size is supposed to be smaller than the critical crack spacing, so that no further propagation of microcracks occurs. [60, 91].

Xiao and coworkers carried out the electrode patterning and improved cycling performance of the Si thin film anodes [46]. 100 nm thick Si films were deposited on 0.5 mm thick Cu substrates using electron beam evaporation. Prior to the deposition, Ni meshes were mounted as shadow masks, and the patterned Si islands were selectively deposited. Since the minimum crack spacing was ca. 7 µm, they chose three different sizes of Ni meshes, which contained pattern widths of 40, 17, and 7 µm. They also estimated the minimum crack spacing by a simple calculation. In Figure 2.5, when the Si patch begins to crack, the force equilibrium is as following,

$$\frac{\tau_{\mathrm{cr}}^{\mathrm{int}} L_{\mathrm{cr}}}{2} = \sigma_Y^{\mathrm{Si}} h,\ \tau_{\mathrm{cr}}^{\mathrm{int}} = \min\left(\tau_Y^{\mathrm{Cu}},\ \tau_f^{\mathrm{int}}\right) \qquad (2.1)$$

where $\tau_{\mathrm{cr}}^{\mathrm{int}}$ is the interfacial shear strength between the lithiated Si and Cu. Both the shear flow stress of Cu τ_Y^{Cu} and the friction strength of metal-silicate composite τ_f^{int} are about 40 MPa, indicating that the estimate of the interfacial shear strength $\tau_{\mathrm{cr}}^{\mathrm{int}}$ is 40MPa. Film thickness h is 100 nm and the film stress σ_Y^{Si} was measured as 1-1.75 GPa in the previously reported experiment [92]. Finally, the minimum crack spacing that no additional cracks are allowed was calculated to be L_{cr}=5.1-8.9 µm.

After electrochemical cycling, most of the Si patches with 40 µm and 17 µm patterns were peeled off, as shown in Figure 2.6a and b. However, the sample with 7 µm patterns, which was approximately the minimum crack spacing, showed that the all the Si patches adhered to the Cu substrate (Figure 2.6c). With good integration of the films onto the substrates, better cycling performance was observed.

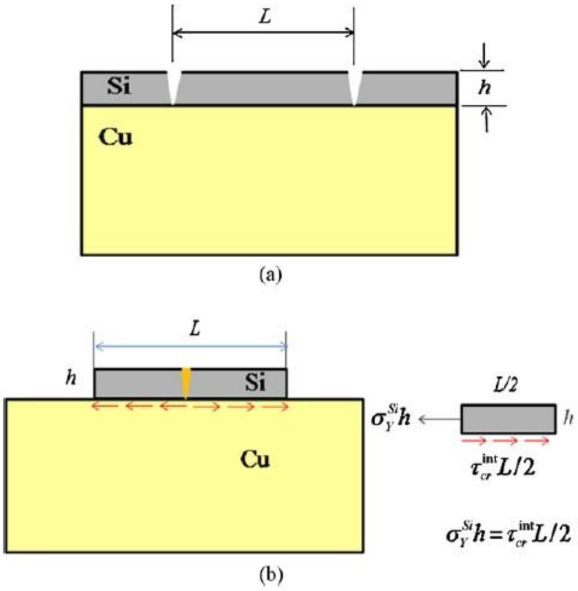

(a)

(b)

Figure 2.5 (a) Schematic diagram of lithiated Si film on Cu substrate. (b) Minimum crack spacing that no longer additional crack is created [46].

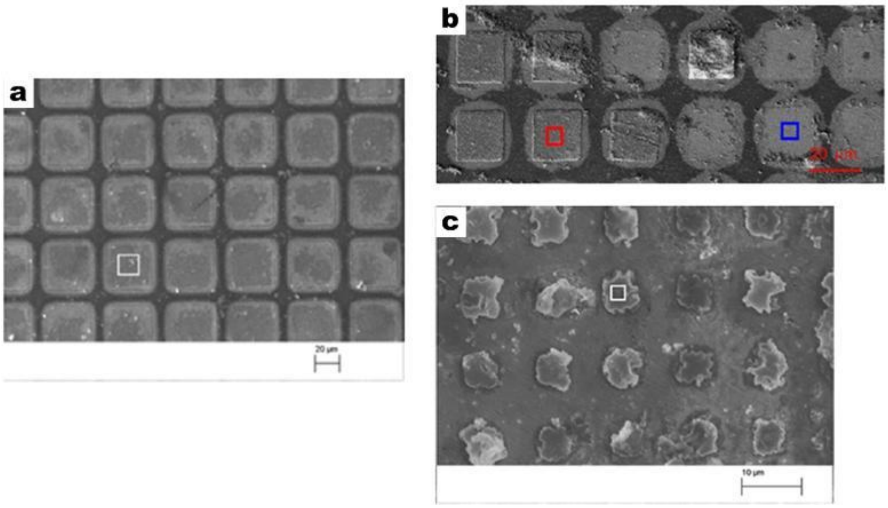

Figure 2.6 (a) SEM image of 40µm pattern size, (b) 17µm pattern size, and (c) 7µm pattern Si patches after cycling size [46].

2.2.5 Si-N composite anodes

Incorporation of other materials in silicon potentially can limit the volume expansion, such as copper (inactive material) [52, 67], carbon (active material) [93, 94], oxygen [47, 61, 95], and nitrogen [68, 96]. Among these materials, nitride has been less frequently investigated. Ahn et al. have examined the effects of nitrogen on the electrochemical properties of 200 nm thick silicon nitride ($Si_{1-x}N_x$) thin films deposited by a RF magnetron sputtering. Figure 2.7 shows cycling performance of $Si_{1-x}N_x$ (x = 0, 0.24, 0.41) thin films at 0.5 C rate. In Figure 2.7b, the $Si_{0.76}N_{0.24}$ sample shows that the capacity abruptly increased at the 650th cycle. The $Si_{0.59}N_{0.41}$ sample had negligible capacity during the whole 850 cycles. In their study, the analytic interpretation of the abnormal electrochemical behaviors was not discussed. The behaviors were explained by the mechanical stability of Si_3N_4.

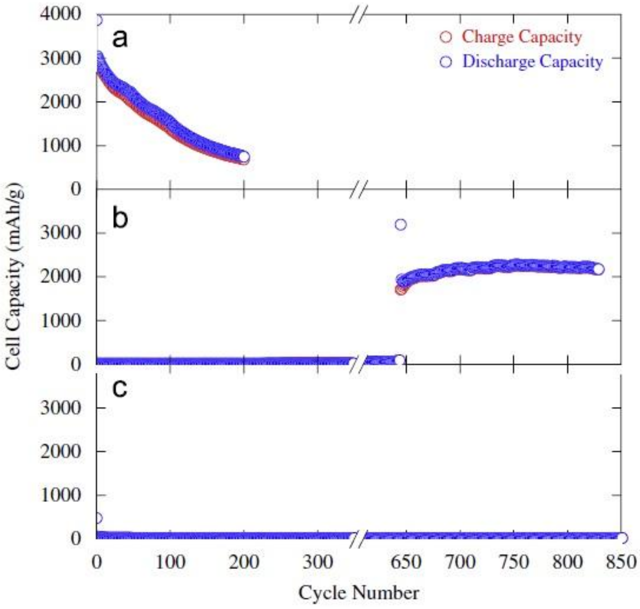

Figure 2.7 Cycling performance of 200 nm thick (a) *a*-Si, (b) $Si_{0.76}N_{0.24}$, and (c) $Si_{0.59}N_{0.41}$ thin films at 0.5 C rate.

Suzuki et al. have investigated electrode properties of 200 nm thick $SiN_{0.92}$ thin films as a negative electrode. The film was formed by using a pulsed laser deposition technique. In particular, they used solid state electrolyte instead of liquid electrolyte. Figure 2.8 shows the cycling performance of the 200 nm and 500 nm thick $SiN_{0.92}$ films. Both films were shown to have fairly good cyclability. However, the reversible capacity of 1300 mAh g^{-1} was not comparable to the specific capacity of Si based anodes (>2000 mAh g^{-1}).

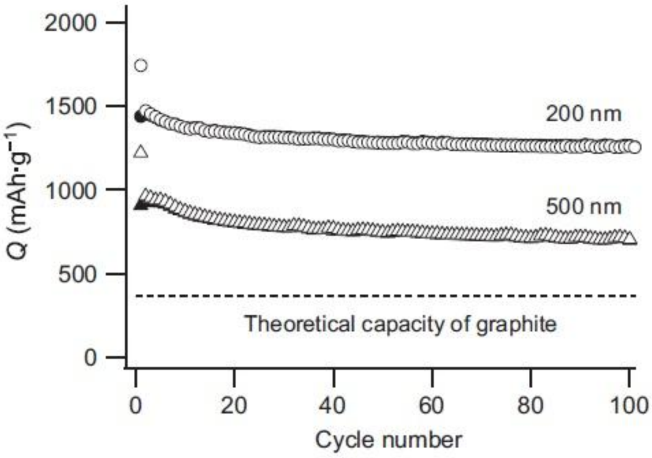

Figure 2.8 Cycling performance of $SiN_{0.92}$ films for the thickness of 200 nm and 500 nm.

CHAPTER 3. ENGINEERING SILICON-RICH NITRIDE ANODES

3.1 Introduction

Thin film anodes were chosen in this study due to their uniform and direct deposition onto the substrates minimizing multiple syntheses. Prior to proceeding the thin film technology, two following questions must be asked. (1) How can we improve the film contact? (2) How can we analyze the improved performance of anodes? In order to enhance the film adhesion, two techniques are introduced in this chapter, including a thin film deposition method (PECVD) and surface treatments of the current collectors. We engineered the Si-rich nitride (Si-rich SiN_x) by controlling the deposition parameters. Silicon nitride has been shown to be converted into silicon with the formation of lithium nitride (Li_3N) by the reaction in equation 3.1 [68]. The resultant silicon can react with lithium in a further reduction while the ductile and conductive Li_3N matrix buffers volume expansion of the Si-Li alloy. The reaction potential of the conversion reaction of nitride has been shown to be below one volt vs Li. The control of silicon and nitride composition is critical because stoichiometric silicon nitride ($SiN_{1.33}$) behaves like an electrical insulator, which leads to extremely low charge and discharge capacity.

$$\mathrm{SiN_x} + \mathrm{yLi^+} + \mathrm{ye^-} \rightarrow \mathrm{Si} + \mathrm{xLi_{y/x}N} \qquad (3.1)$$

$$\mathrm{Si} + \mathrm{xLi^+} + \mathrm{xe^-} \leftrightarrow \mathrm{Li_xSi} \qquad (3.2)$$

The surface treatments were performed by roughening the current collectors with a mechanical scratching and a chemical etching. For better analysis of the anode performance, several techniques were utilized such as AFM, XPS, Potentiostat, SEM and TEM. The graphical and quantitative surface profiler AFM was used to observe the surface effect by the roughening treatment prior to the film deposition. After the film growth, we confirmed various chemical compositions in the material using XPS. Prepared anodes were then cycled using an electrochemical testing tool, Potentiostat. The morphology changes were observed after electrochemical cycles using SEM and TEM. Indeed, further characterization is required to better analyze the mechanical properties of the materials, which will be discussed in chapter 4.

3.2 Plasma enhanced chemical vapor deposition (PECVD) technique

Plasma enhanced chemical vapor deposition (PECVD) is a process to deposit films by ionizing reactive gases with plasma at low temperature (100~350 ^{0}C). Such low temperature process is critical for the device fabrication that requires low sensitivity to temperature and low residual stresses [97]. PECVD is a versatile manufacturing process. Amorphous silicon (*a*-Si) with varied chemical composition (e.g., doped with oxygen, nitrogen, fluorine etc.) can be fabricated [54]. PECVD has been widely used in the microelectronics and photovoltaic industries. The advantages of PECVD are a high deposition rate, a rapid process and a conformal coating for three-dimensional nanostructures [92] compared to other processes such as low pressure CVD [72, 98], physical vapor deposition (PVD) [47, 61, 80, 99] and atomic layer deposition (ALD). Although the PECVD method has been used for silicon-based anodes in several papers [86-89], the rapid capacity fading was observed in those experiments.

Figure 3.1 shows a schematic diagram of a PECVD reactor for the deposition of silicon oxynitride (SiO_xN_y) [100]. A glow discharge is generated between two parallel plates. Reactive gases flow through the discharge, which ionizes the gases creating active species on the sample surface depending on the type of gases. The film quality and thickness are controlled by process parameters including RF power, process temperature, process time, and pressure. The reaction gases include N_2, NH_3, SiH_4, and N_2O.

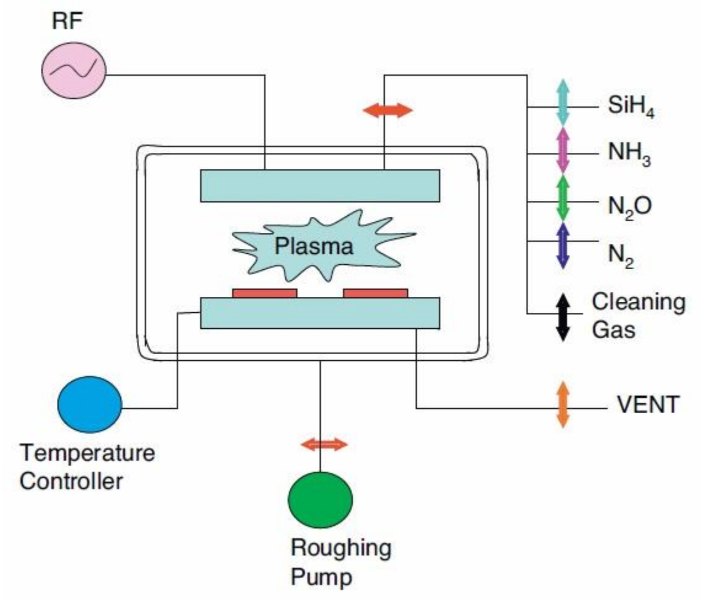

Figure 3.1 Schematic diagram of a PECVD reactor for SiO_xN_y film deposition [100].

3.3 Experimental

3.3.1 Preparation of Cu current collectors

25 µm thick copper foil was purchased from Lyon Industries Inc. Two roughening techniques were used to increase the roughness of the copper, including mechanical scratching and chemical etching. The mechanical scratching was performed by a steel wool. In the etched samples, we first performed the mechanical scratching, and then etched foil by 0.1 mol of ferric chloride ($FeCl_3$) for 5 min. After etching, the copper foil was rinsed with DI water and isopropyl alcohol (IPA). The sample was dried on a heater at 70 °C for 5 min to remove alcohol. An atomic force microscopy (AFM, Veeco Dimension 3100) with a tapping mode was used to characterize the roughness of copper. The scanning rate was 0.3Hz. We used a Si tapping tip to scan the surface morphology of the copper (10 × 10µm). Average roughness of the surface was defined by the root mean square.

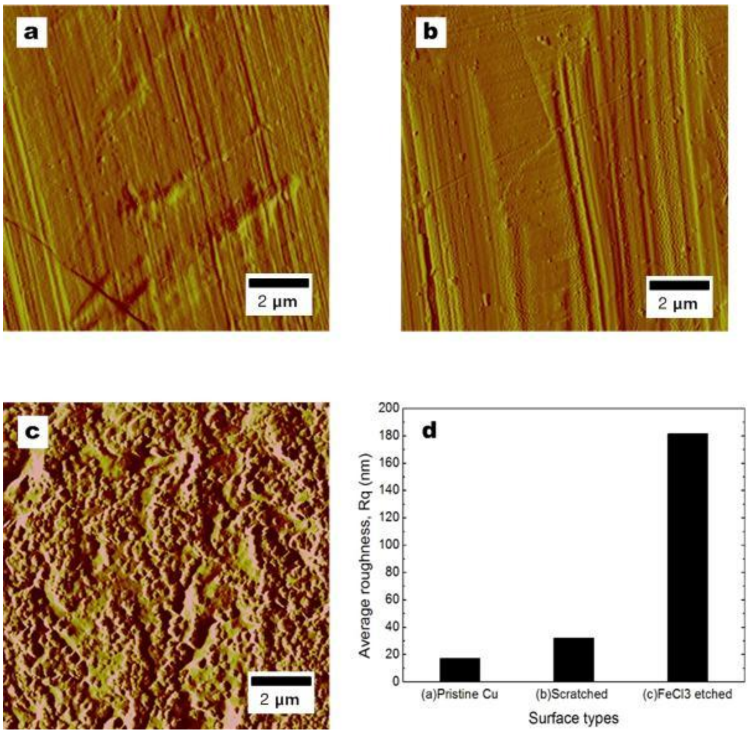

Figure 3.2 AFM micrographs of (a) a pristine Cu foil, (b) a mechanically-scratched Cu foil, and (c) a Cu foil etched with $FeCl_3$. (d) The root mean square average roughness (R_q) of each sample has been quantified.

Figure 3.2 shows the surface morphologies of three different copper substrates measured by AFM, including (3.2a) pristine copper, (3.2b) mechanically-scratched copper, and (3.2c) $FeCl_3$-etched copper. Similar morphologies (straight lines) were found on a pristine copper and on mechanically-scratched copper. The depths of the observed lines were thicker after mechanical scratching. After the $FeCl_3$ etching, numerous islands were formed on the surface, resulting in a larger roughness. In Figure 3.2d, the root mean square average roughness (R_q) of the pristine copper, the mechanically-scratched copper, and the $FeCl_3$-etched copper were 17 nm, 32 nm, and 182 nm, respectively. AFM was also used to image the 250 nm nitride deposited on three different copper substrates. The roughness of the nitride films on the pristine copper, the mechanically-scratched copper, and the $FeCl_3$ etched copper were measured to be 16, 30, and 187 nm, respectively. The roughness of the copper substrates remained the same before and after *a*-Si coating, indicating that the *a*-Si was uniformly deposited.

3.3.2 Preparation of anode materials

SiN_x thin films were deposited on as-prepared copper substrates using PECVD (Plasma Therm 790). The deposition parameters for *a*-Si were 100% SiH_4, flow rate 5 sccm, temperature 100 ^oC, pressure 450 mTorr and radio frequency (RF) power 25 W. Nitride was deposited by diluted silane (2% SiH_4 in 98% N_2). The typical deposition parameters for nitride were: flow rate 50 sccm, temperature 350 ^oC, pressure 450 mTorr and RF power 25 W. Films deposited at different temperature (100 ℃, 200 ℃, 300 ℃) and RF power (25 W, 50 W, 100 W) were also evaluated. The thickness of films was measured using a surface profiler (Dektak 8). Electron beam evaporated *a*-Si (using Temescal BJD 1800) was also deposited as a control. The weights of the *a*-Si and nitride films were measured by a microbalance (Mettler Toledo, XP26) before and after thin film deposition. The balance had the accuracy of ±1 μg. Prior to the film deposition, the copper foils were dried in a vacuum oven in order to remove moisture.

3.3.3 Surface characterization

XPS was used to analyze the chemical composition of SiN_x films with a PHI 5500 ESCA (Perkin Elmer). XPS is a powerful tool for the quantitative study of the surface chemistry such as molecular bonding and chemical composition. A XPS spectrum is a plot of the number of electrons for each element versus the binding energy of the electrons. The X-ray power was 210 W and the emission current was 15 mA. Neutralization was performed to prevent charging effects. We first performed a survey scan (0-1200 eV) to quantify chemical composition. Then a high resolution analysis was conducted on each element with 23.5 eV pass energy. The characteristic peaks in XPS spectra refer to the electron composition within the atoms, such as 1s, 2s, 2p, etc. The atomic concentration (%) of each element was obtained by dividing the signal intensity by a relative sensitivity factor using software (AugerScan 3.2).

Table 3.1 shows the atomic composition of SiN_x on three different substrates and bare *a*-Si on $FeCl_3$-etched copper before electrochemical cycling using XPS. Depth profiling was conducted for 5 min on each sample with a sputter rate of 0.8 nm/min. Because SiN_x was deposited using the same process parameters, it showed similar compositions of silicon, nitrogen, and oxygen on different substrates (Table 3.1a-c). The presence of both silicon and nitrogen were expected because the reactive gas (2% SiH_4 was diluted in 98% N_2) was ionized in the chamber. The presence of oxygen is most likely caused by the oxidation of the silicon surface when exposed to air after deposition. For bare *a*-Si films, the concentration of Si was highest (Table 3.1d).

	C 1s	**O 1s**	**N 1s**	**Cu 2p**	**Si 2p**
(a) SiN_x on a pristine Cu	**5.5**	**5.1**	**38.8**	**-**	**50.5**
(b) SiN_x on a mechanically-scratched Cu	**2.5**	**3.3**	**40.3**	**-**	**53.8**
(c) SiN_x on a $FeCl_3$-etched Cu	**2.2**	**2.7**	**40.4**	**1.3**	**52.9**
(d) Bare *a*-Si on a $FeCl_3$-etched Cu before cycling	**1.9**	**1.8**	**-**	**1.4**	**94.9**

Table 3.1 Atomic concentration (%) of elements of amorphous SiN_x films on a pristine, mechanically-scratched, and $FeCl_3$-etched copper substrates and *a*-Si film on a $FeCl_3$-etched copper substrate before cycling.

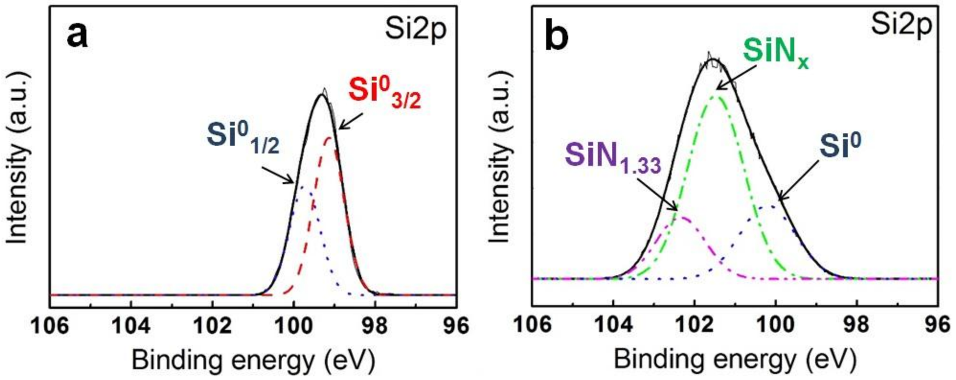

Figure 3.3 The high resolution XPS spectra of Si 2p of (a) PECVD *a*-Si and (b) PECVD nitride.

Figure 3.3 shows the XPS Si 2p spectra of PECVD *a*-Si and silicon nitride before cycling. The *a*-Si film was composed of Si^0. Compared to *a*-Si, the Si 2p spectrum of nitride consisted of a broad peak. In Figure 3.3b, the Si 2p spectrum of silicon nitride was fitted using three Gaussian functions of Si^0 (100.07 eV), SiN_x (101.48 eV), and $SiN_{1.33}$ (102.34 eV). The ratios of $SiN_{1.33}$, SiN_x and Si^0 were determined to be 13%, 70%, and 17%, respectively. Using XPS survey, the atomic concentration of silicon and nitrogen in nitride was 57% and 43%, respectively. Based on the fitting, the value x in SiN_x was estimated to be 0.83.

After electrochemical tests, the cells were disassembled and then rinsed with DMC solvent. Scanning electron microscopy (SEM, JEOL JSM-6510LV) was used to image surface morphologies of samples before and after cycling. The acceleration voltage was 15 kV in SEM. High-resolution transmission electron microscopy (TEM, Titan) was conducted to image the surface of nitride films with its high resolution (300 kV) after 300 cycles. A thin sample of anode was prepared with a dual-beam focus ion beam (FIB, TESCAN LYRA).

3.3.4 Cell assembly and testing

The electrochemical characteristics of the *a*-Si and nitride films were measured by a half-cell configuration. All the cell assembly and electrochemical testing were performed in a glove box filled with ambient Argon. The cell was assembled using a CR2032 coin cell. Lithium metal (Alfa Aesar) was used as counter and reference electrodes. A polyethylene separator (Celgard 2320) was soaked overnight in the liquid electrolyte (1 mol $LiPF_6$ in ethylene carbonate (EC) and dimethyl carbonate (DMC) with a 1:1 ratio). The charge and discharge tests were performed using a potentiostat (Maccor Model 4200) at a constant current density of 2 A/g. The cut-off voltages were set 0.001 V and 2 V versus Li^+/Li. Cyclic voltammetry analysis was employed at 0.2 mV/s scan rate with voltage ranged from 0.001 to 2 V (Gamry Series G 300).

3.4 Results and discussion

3.4.1 PECVD silicon nitride for a high-performance lithium ion battery anode

Figure 3.4 illustrates the charge and discharge curves of evaporated *a*-Si, PECVD *a*-Si and PECVD nitride. These films were cycled at 1C, which refers to one-hour charge. Figure 3.4a and b show the charge and discharge curves of first, second and 50th cycles of *a*-Si deposited by evaporation and PECVD, respectively. In this study, cathodic lithiation in the anode was referred to charge. In the first charge, the voltage plateaus for the evaporated and PECVD *a*-Si films were slightly different (0.3 V and 0.24 V respectively). The voltage plateau corresponds to the formation of Si-Li alloys. The first charge capacity for evaporated and PECVD *a*-Si films were similar (3827 and 3993 mAh g^{-1} respectively). The following discharge curve had a voltage plateau around 0.37 V for both evaporated and PECVD *a*-Si films. The first discharge capacity for evaporated and PECVD *a*-Si were 3348 mAh g^{-1} and

3233 mAh g^{-1}, making Coulombic efficiency 87% and 81%, respectively. The initial capacity loss was probably due to reduction reactions in the electrolyte, resulting in solid-electrolyte interphase (SEI) formation [22, 39]. The Coulombic efficiency for the samples became approximately 99.2% after a couple of cycles, but dropped to 97.8% afterwards. The capacity retention of evaporated *a*-Si was slightly higher than that of PECVD *a*-Si.

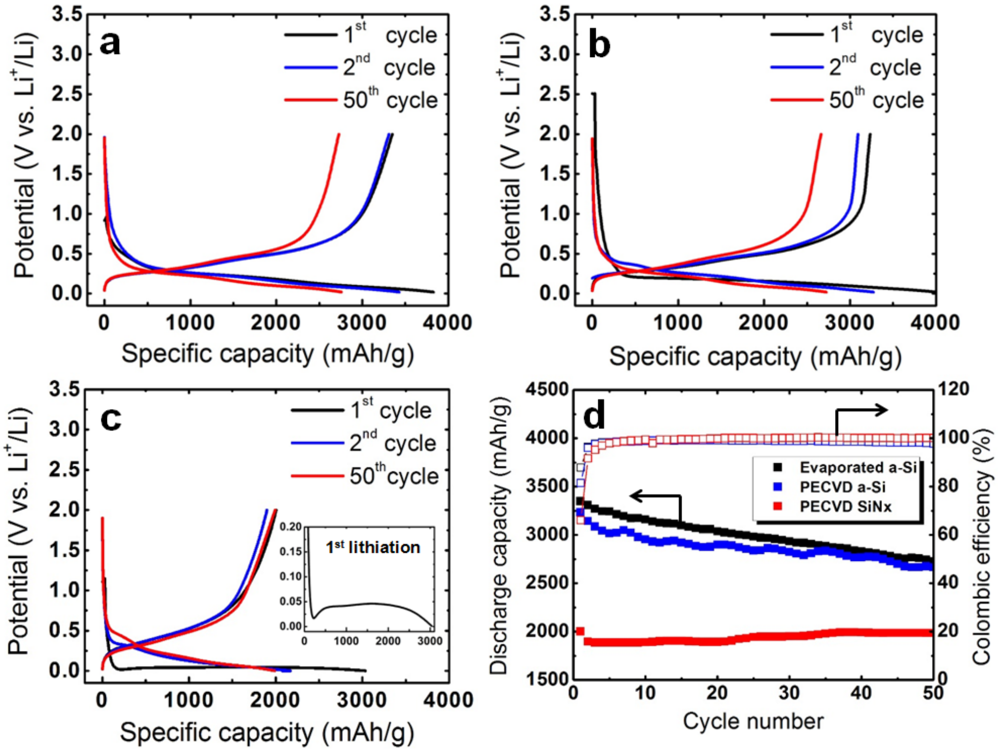

Figure 3.4 The voltage profiles during 50 cycles for (a) evaporated *a*-Si and (b) PECVD *a*-Si, and (c) PECVD nitride. (d) The cycling performance of three samples.

In Fig 3.4c, PECVD nitride showed a different voltage profile compared to *a*-Si films. At the initial stage of the first charge, the voltage profile had a potential overshoot, which indicated the nucleation of a new phase to form Li_3N during the conversion reaction [60]. The first discharge capacity of PECVD nitride was 2004 mAh g^{-1}, corresponding to a 66% Coulombic efficiency. The low Coulombic efficiency could be attributed to irreversible conversion reactions in addition to SEI formation. The Coulombic efficiency increased during the second and third cycle and maintained almost 100% for the rest of cycles. The discharge capacity at the 50th cycle was 1984 mAh g^{-1}. PECVD nitride had a higher capacity retention (99%) compared to PECVD *a*-Si (84%). The incorporation of nitrogen limited the specific capacity but improved the cycling stability resulting in higher Coulombic efficiency.

The Li-N matrix after cycling was studied using XPS. Figure 3.5 shows the high resolution N 1s spectra of the nitride before and after 100 cycles. Before reactions, the spectrum (Figure 3.5a) of N1s was fitted by two Gaussian functions SiN_x and $SiN_{1.33}$, and their ratio was 84% and 16%, respectively. After 100 cycles, the spectrum was fitted by three Gaussian functions. The ratio of SiN_x and $SiN_{1.33}$ became 66% and 24%, indicating that SiN_x was oxidized to nonconductive $SiN_{1.33}$ during multiple cycles. In addition, a new peak was present at 399.7 eV, which corresponds to Li_3N. Li_3N has high ionic conductivity (2-5 x 10^{-4} Scm^{-1}), which may play a role in facilitating Li ion transport [101, 102].

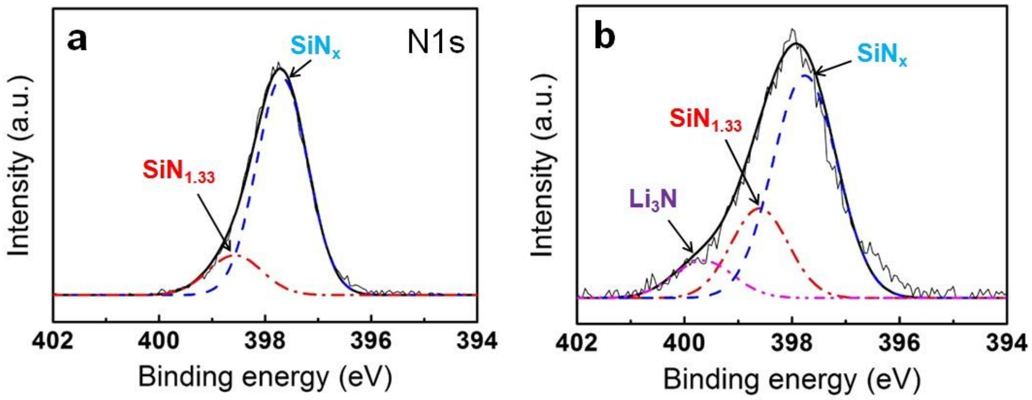

Figure 3.5 The high resolution N 1s spectra of the Si-rich nitride anode (a) before cycle, and (b) after 100 cycles.

Figure 3.6 shows the impedance spectra of evaporated *a*-Si and PECVD nitride anodes during 300 cycles. The semicircle in the middle frequency region represents the charge transfer impedance, which is associated with an internal resistance. During the first

100 cycles, the evaporated *a*-Si was shown to have lower internal resistances compared to the PECVD nitride. The charge transfer impedance of the evaporated *a*-Si increased with further cycles up to 300 cycles (Figure 3.6a). However, the impedance of the nitride was reduced over the cycles (Figure 3.6b), suggesting that the nitride electrode maintains good structural stability over the cycles.

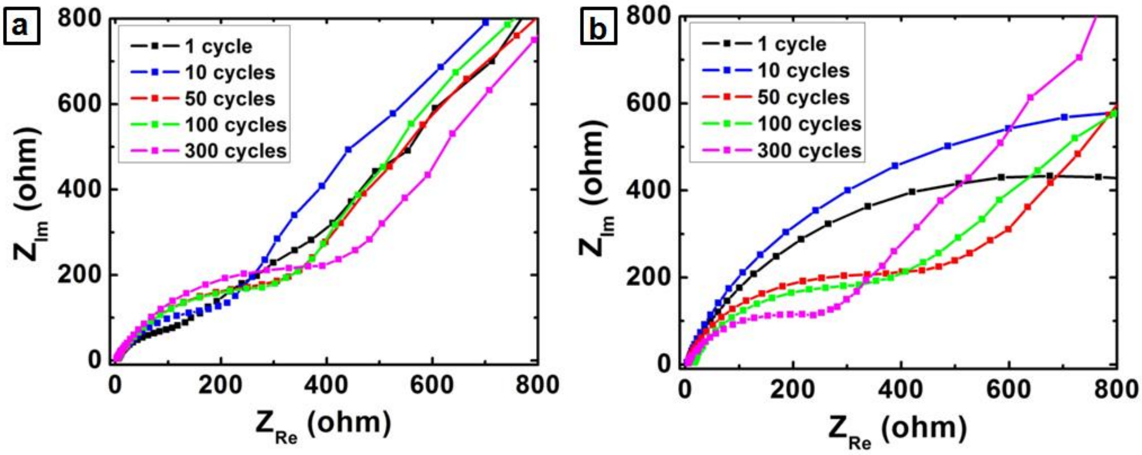

Figure 3.6 Nyquist plots of (a) evaporated *a*-Si and (b) PECVD nitride anodes during 300 cycles.

3.4.2 Controlling deposition conditions (process temperature)

The deposition parameters (such as temperature and power) for PECVD nitride have been studied in order to tune chemical compositions and its electrochemical properties. The common nitrogen source in PECVD nitride is ammonia (NH_3), and it produces hydrogen rich nitride [14, 103]. By using N_2 instead of NH_3 as the nitrogen source, a low hydrogen content silicon nitride is obtained. N_2 has an inherently higher binding energy than NH_3, which hinders ionization. With higher temperature and higher power during deposition, N_2 could dissociate into free nitrogen active species. Figure 3.7 shows X-ray photoelectron spectra of the SiN_x films deposited at 100, 200, and 300°C. Their surfaces were sputtered for 5 min using an Ar gas prior to the analysis in order to remove surface contaminants. Atomic concentration of nitrogen content of each sample was found to be 35.6, 38.6, and 44.2 % at 100, 200, and 300°C, respectively (Table 3.2). In this case, the value, x in SiN_x was estimated 0.62, 0.69, and 0.88 at 100, 200, and 300°C, respectively.

	C 1s	**O 1s**	**N 1s**	**Cu 2p**	**Si 2p**
(a) 100°C sample	**2.2**	**4.4**	**35.6**	**-**	**57.5**
(b) 200°C sample	**2.1**	**2.8**	**38.6**	**-**	**56.1**
(c) 300°C sample	**1.8**	**3.1**	**44.2**	**-**	**50.5**

Table 3.2 Atomic concentration (%) of elements of amorphous SiN_x films deposited at 100 °C, 200 °C, and 300 °C before cycling.

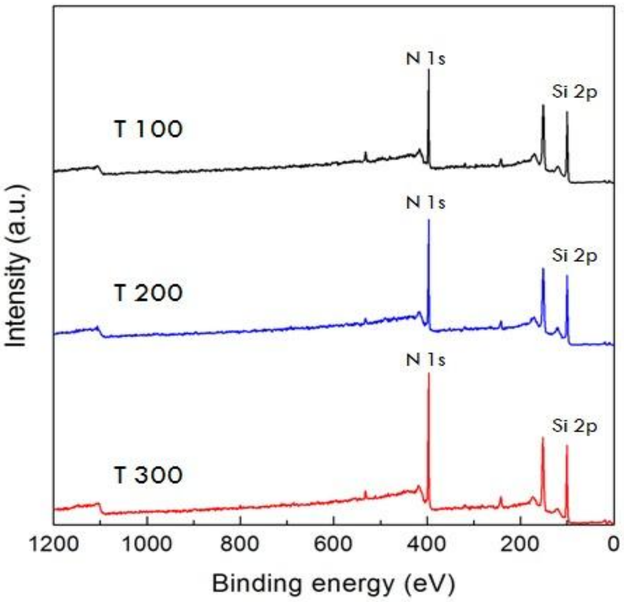

Figure 3.7 XPS spectra of 250 nm SiN_x films deposited at (a) 100, (b) 200, and (c) 300 °C in the PECVD.

Figure 3.8 shows the high resolution XPS spectra of the Si 2p and corresponding cycling performance of PECVD nitride deposited at different temperatures (100 ℃, 200 ℃, and 300 ℃) with a constant RF power of 25 W. The concentration of nitrogen increased with increasing deposition temperature (Figure 3.8a-c). PECVD nitride deposited at lower temperature (100 ℃) had slightly higher specific capacity.

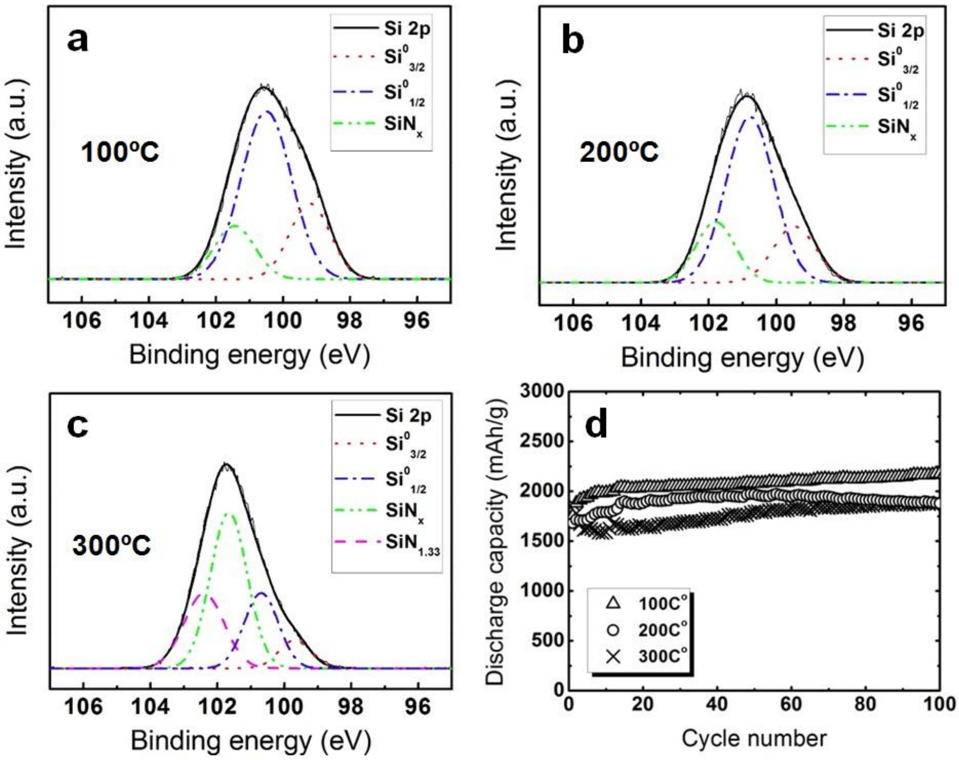

Figure 3.8 The high resolution XPS spectra of the Si 2p for PECVD nitride deposited (a) at 100 ℃, (b) 200 ℃, and (c) 300 ℃. (d) The cycling performance of three samples grown at different temperatures.

Figure 3.9 shows SEM images of 250 nm SiN_x films deposited at 100, 200, and 300 ℃ in the PECVD that were cycled for 100 and 300 cycles. The three samples that experienced 100 cycles (Figure 3.9a, c, and e) all have similar morphologies with crack size of ~3µm. The capacity retention of those samples after 100 cycles was 124, 112, and 101% for 100, 200 and 300 ℃ samples, respectively. However, the films after 300 cycles were differentiated by the spacing distances of the cracks and sizes of islands. The 100 ℃ sample had the largest island size and crack spacing, because the higher amount of silicon content was incorporated into the film more than others, therefore the volume changes in silicon were larger.

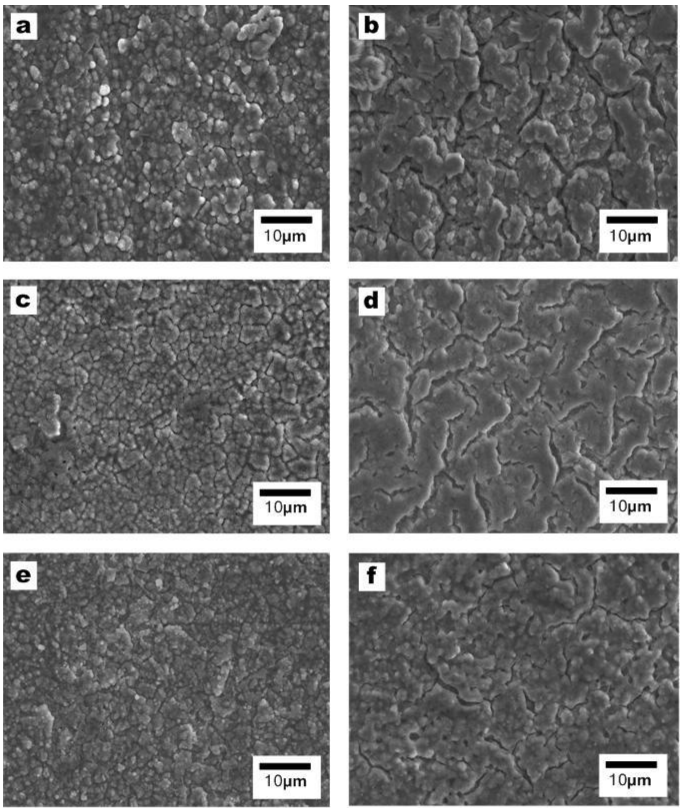

Figure 3.9 SEM images of 250 nm SiN_x films deposited (a) at 100 ℃ in the PECVD after 100 cycles, and (b) after 300 cycles, (c) at 200 ℃ in the PECVD after 100 cycles, and (d) after 300 cycles, (e) at 300 ℃ in the PECVD after 100 cycles, and (f) after 300 cycles. All the films were deposited on the etched Cu.

3.4.3 Controlling deposition conditions (RF power)

Figure 3.10 shows the high resolution XPS spectra of the Si 2p and cycling performance of PECVD nitride deposited at RF power of 25 W, 50 W, and 100 W at a constant temperature 100 ℃. Atomic concentration of nitrogen content of each sample was nearly similar. However, the amount of silicon and oxygen contents varied in controlling the RF power. The atomic concentration of silicon content was 57.5, 54.9, and 44.7% for 25, 50, and 100 W samples, respectively (Table 3.3). The amount of silicon decreased when the RF power increased. On the other hand, oxygen content increased with the increase in RF power. It is known that the Si content in the silicon nitride film becomes less rich when the RF power increases. Moreover, an excessive increase in the RF power can cause damage to the silicon, and more defects or impurities are expected to exist on the surface. It is also known that when the higher RF power is applied, the lower uniformity of films is made. Non-uniformity of films can be observed from the 100W sample, which includes the Cu 2p peak. It is evident that the film does not cover the whole surface.

	C 1s	**O 1s**	**N 1s**	**Cu 2p**	**Si 2p**
(a) 25W sample	**2.2**	**4.4**	**35.6**	**-**	**57.5**
(b) 50W sample	**1.6**	**8.0**	**34.6**	**0.4**	**54.9**
(c) 100W sample	**3.4**	**12.3**	**37.5**	**1.3**	**44.7**

Table 3.3 Atomic concentration (%) of elements of amorphous SiN_x films deposited at 25W, 50W, and 100W before cycling.

The atomic ratio of silicon to nitrogen decreased with increasing RF power. In addition, silicon became more oxidized with the increasing RF power. The specific capacity of nitride was very sensitive to RF power during deposition, and it decreased with increasing RF power. In Figure 3.11d, nitride deposited at 100 W was shown to have an extremely low specific capacity. The highly oxidized silicon and nonconductive $SiN_{1.33}$ caused detrimental effects on the cyclic performance.

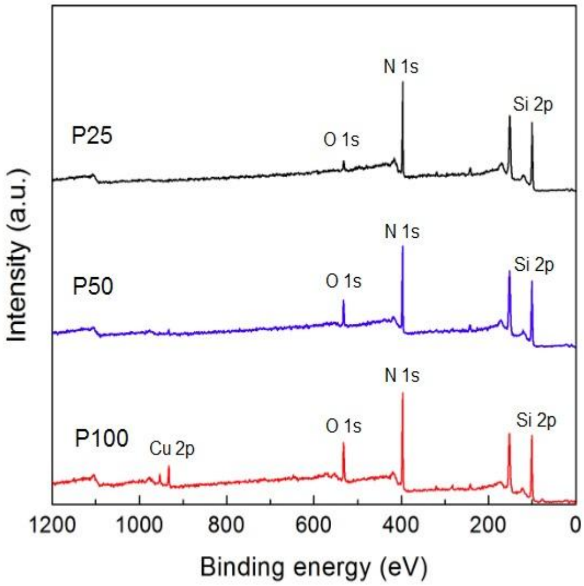

Figure 3.10 XPS spectra of 250 nm SiN_x films deposited at plasma power of (a) 25, (b) 50, and (c) 100 W in the PECVD.

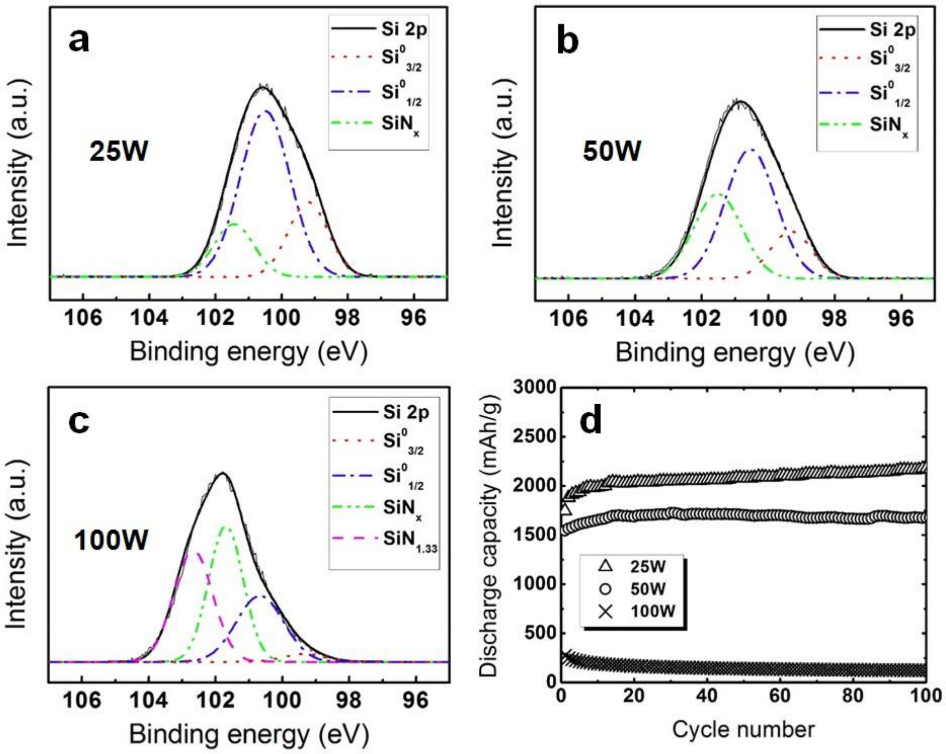

Figure 3.11 The high resolution XPS spectra of the Si 2p for PECVD nitride deposited (a) at 25 W, (b) 50 W, and (c) 100 W. (d) The cycling performance of three samples grown at different plasma RF powers.

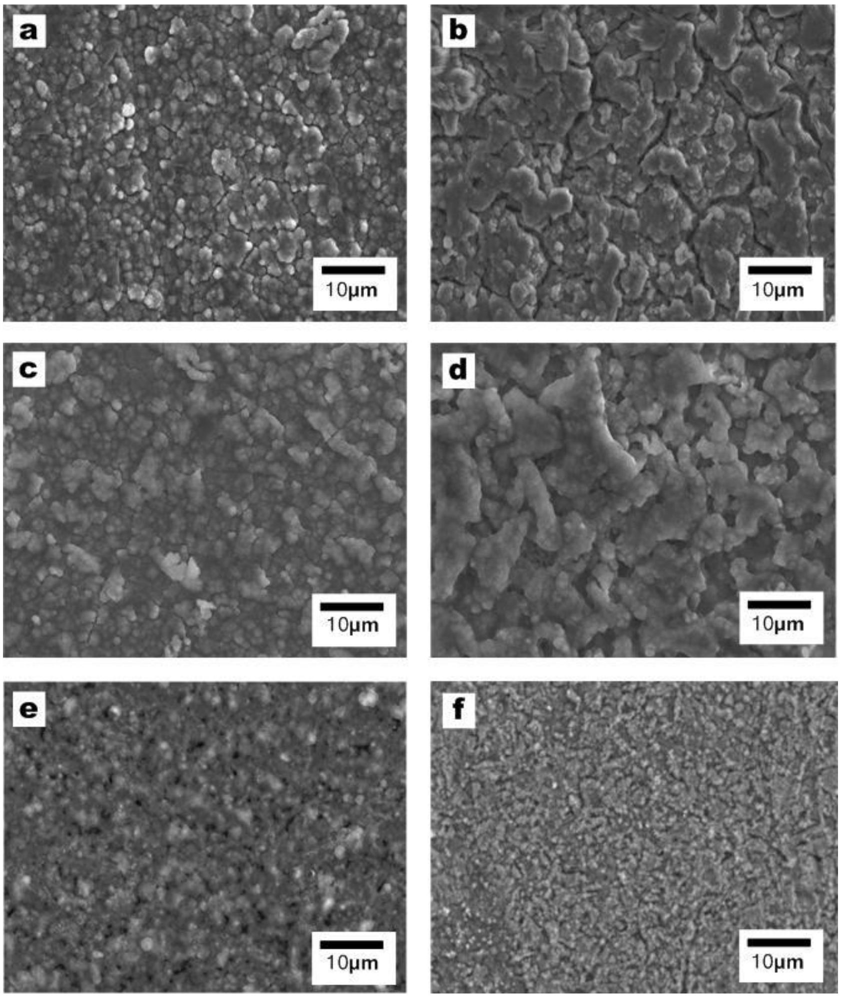

Figure 3.12 SEM images of 250 nm SiN_x films deposited (a) at 25 W in the PECVD after 100 cycles, and (b) after 300 cycles, (c) at 50 W in the PECVD after 100 cycles, and (d) after 300 cycles, (e) at 100 W in the PECVD after 100 cycles, and (f) after 300 cycles. All the films were deposited on the etched Cu.

In SEM images, the Si films deposited at 25 and 50W after 300 cycles (Figure 3.12b and d) formed larger agglomerates and cracks on the surface than after 100 cycles (Figure 3.12a and c). Those fractures were due to the large stress induced by the volume expansion, which might lead to the disconnection and the fragmentation of the active material from the current collectors, resulting in the capacity fading. The difference in the cyclic performance between the 25 and 50W samples were attributed to the different amount of Si contents. The deteriorated performance of the 100W sample was ascribed to the small amount of Si contents, side reactions with oxide, and rigid mechanical properties of SiN_x.

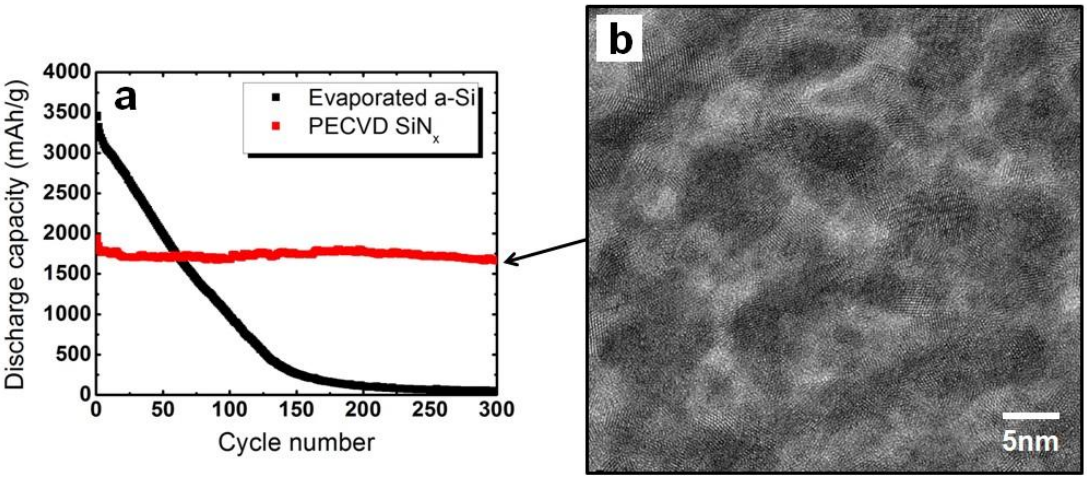

Figure 3.13 (a) The cycling performances of 250 nm thick evaporated *a*-Si and PECVD nitride during 300 cycles. (b) A TEM image of PECVD nitride after 300 cycles.

250 nm evaporated *a*-Si and PECVD nitride anodes were tested for 300 cycles and the results are shown in Figure 3.13a. In the initial 50 cycles, the capacity of evaporated *a*-Si was higher than the PECVD nitride. Nevertheless, the capacity of evaporated *a*-Si gradually dropped during cycling. PECVD nitride showed a stable cyclic performance. Under inspection by SEM, large cracks were found in evaporated *a*-Si and silicon eventually peeled-off from the substrate. On the other hand, PECVD nitride formed small islands (diameter 5~7 μm) and strongly adhered to the substrate (Figure 3.14). The level of adhesion of the evaporated silicon and PECVD nitride were investigated using a scotch tape test (Figure 3.15). Compared to evaporated silicon, PECVD nitride showed a strong adhesion, probably due to ion bombardment of reactive gases during the deposition.

Figure 3.13b shows a high resolution TEM image of PECVD nitride after 300 cycles. The lattice structure of silicon nanocrystal (diameter of 5-10 nm) was clearly seen. The silicon nanocrystals were uniformly embedded in a matrix made of Li_3N. Li_3N acts as a barrier to prevent the aggregation of silicon nanocrystals and maintained structural stability

[104]. In addition, Li_3N is known to have a high ionic conductivity, which may enhance the charge transfer during lithiation and delithiation. Compared to other conversion anode material such as silicon oxide, nitride has been found to have a better Coulombic efficiency over many cycles [95].

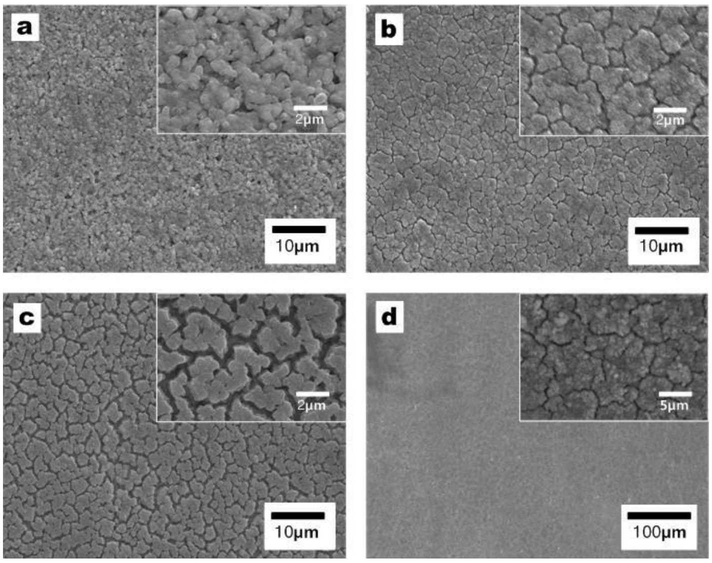

Figure 3.14 The SEM images of PECVD nitride films (a) before cycling, (b) after 30 cycles, (c) after 100 cycles, and (d) after 300 cycles.

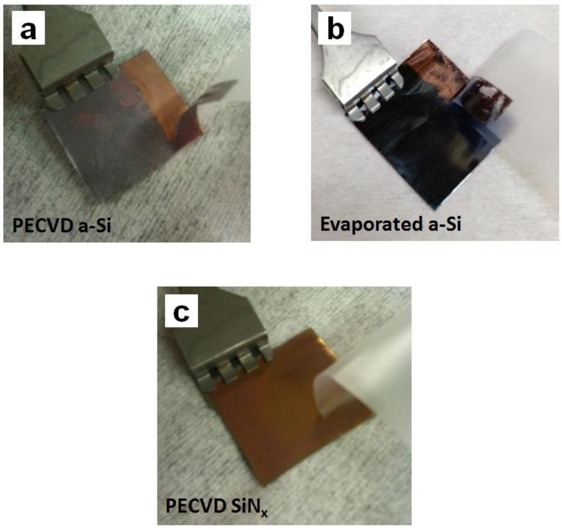

Figure 3.15 An adhesion test using a scotch tape of (a) PECVD *a*-Si, (b) evaporated *a*-Si, and (c) PECVD nitride on a pristine copper foil.

3.4.4 Surface effect of the current collectors

In the half-cell setting, SiN_x was a working electrode, and the lithium metal was used as a counter and reference electrode. During the charge, the lithium ions migrated to the silicon and formed silicon-lithium alloys. The voltage started from an open circuit voltage and dropped to near 0 V with time. The cut-off voltage was set to 0.001-2 V. The plateau near 0 V indicates the Si-Li alloying reaction. During the discharge, the lithium ions delithiated from the Si-Li alloys and migrated to the counter electrode. The voltage increased with time. The typical discharge voltage for the silicon anode is ca. 0.5 V.

Figure 3.16 shows the cyclic performance of SiN_x films on the three different substrates in terms of discharge capacity and Coulombic efficiency. The Coulombic efficiency of a, b, and c after 50 cycles were 95, 97, and 100%, respectively. However, initial irreversible capacity loss was observed for the silicon anode because liquid electrolyte formed the nonconducting SEI layer on the large surface area. The reversible discharge capacity of the $FeCl_3$-etched sample was about 2200 mAh g^{-1}, and it showed relatively small capacity loss compared to other samples.

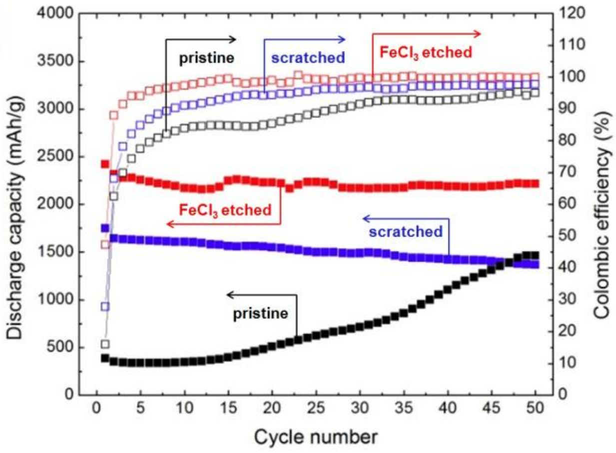

Figure 3.16 Cyclic performance of the *a*-Si anodes on the pristine (black), scratched (blue), and FeCl3-etched (red) Cu substrates.

Figure 3.17 illustrates SEM images of the surface morphologies before cycling and after first charging, 30 cycles, and 100 cycles. PECVD films were deposited on three types of current collectors: pristine Cu (a-d), mechanically-scratched Cu (e-h), and $FeCl_3$-etched Cu (i-l). The increasing crack spacing was visually seen during cycling on the pristine Cu (Figure 3.17a-d), and the fracture caused the loss of electrical contact between the substrate and the active materials. In Figure 3.17b, there was no obvious cracking owing to the nitrogen concentration in the film and rigid mechanical strength of the nitride; cracking can be seen in the other images. Major cracking occurred after several cycles and the surface of the silicon was further exposed to electrolyte so that the lithium ions could react with the uncycled silicon resulting in the improved capacity.

In Figure 3.17c and d, the fracture of films became more frequent and larger. It was concluded that the significant cracking does not occur only during initial charging but also after certain cycles depending on the mechanical properties and the amount of active materials on the surface. The growth of cracks was seen on the mechanically-scratched sample after the first charging (Figure 3.17f). The active material began swelling, and the films broke down, unlike the pristine sample. In Figure 3.17g, the films were fractured and delaminated causing the capacity fading due to the electrical contact loss. After 100 cycles as shown in Figure 3.17h, most of films were crumbled and peeled off. However, the discharge capacity after 50 cycles did not decay significantly because the mechanical scratching was uniformly performed on the whole surface and some films were still attached to the substrate. After the first charge, the films on the $FeCl_3$-etched copper looked similar to the one before cycling (Figure 3.17j). The surface of the $FeCl_3$-etched sample was showmen to have small Si islands even after 30 and 100 cycles (Figure 3.17k and l). The size of cracks after 50 cycles was ca. 3 μm, although the typical size of cracks depends on the film thickness. However, our film on the $FeCl_3$-etched copper did not have separated islands. We discovered that the $FeCl_3$-etched sample showed the best cycle performance via the voltage profile, reversible capacity, and surface morphology.

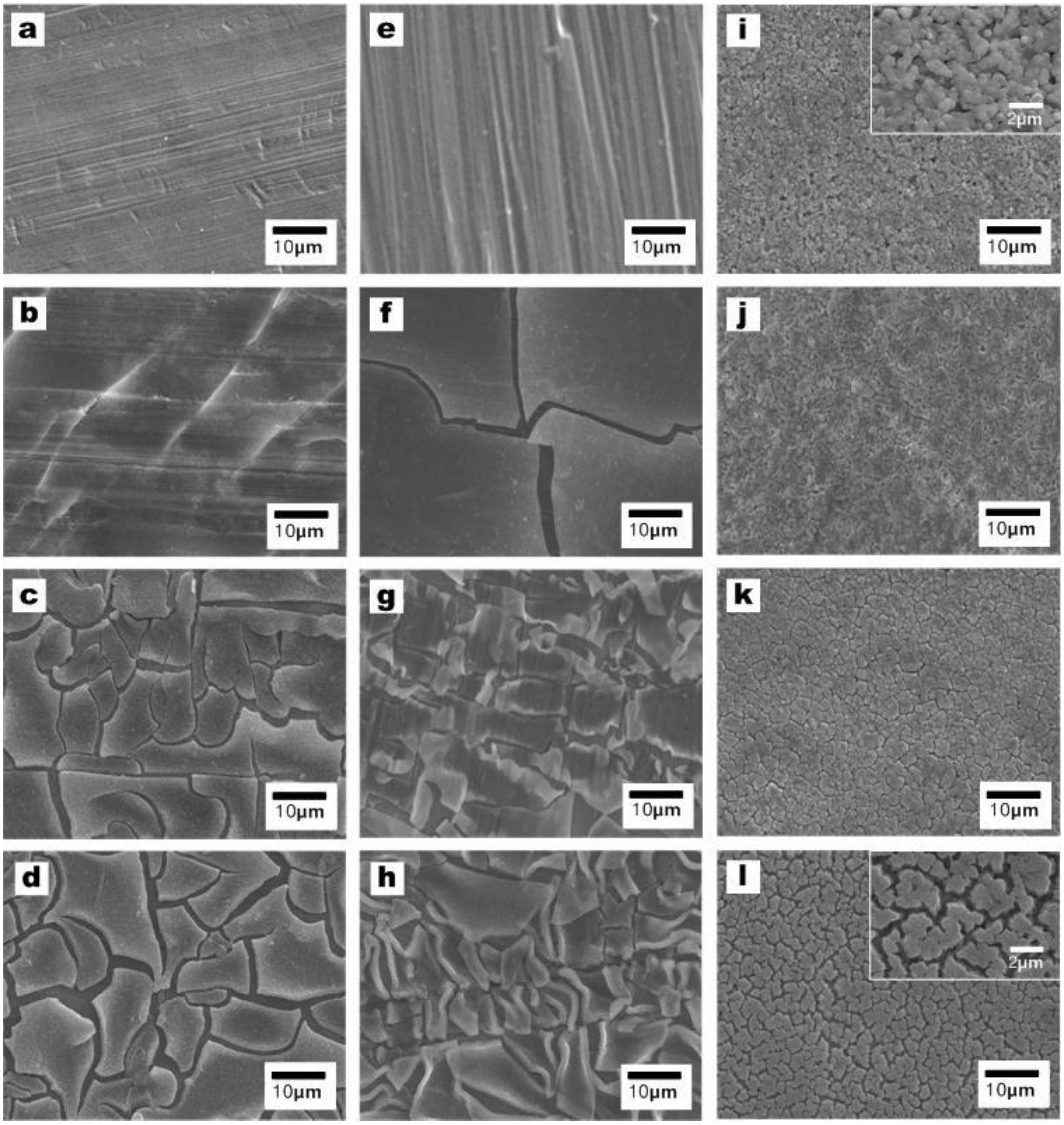

Figure 3.17 SEM images of a 250 nm SiN_x film (a) before cycling, (b) after 1st charge, (c) after 30 cycles, and (d) after 100 cycles on a pristine Cu substrate, (e) before cycling, (f) after 1st charge, (g) after 30 cycles, and (h) after 100 cycles on a mechanically-scratched Cu substrate, (i) before cycling, (j) after 1st charge, (k) after 30 cycles, and (l) after 100 cycles on a $FeCl_3$-etched Cu substrate.

Voltage profiling and cyclic voltammetry upon 100 cycles were conducted for the $FeCl_3$-etched sample. Figure 3.18a shows the cyclic voltammogram of the 100th cycle, and the inset plot is the charge-discharge curves corresponding to the former CV curve. During the charge (Li alloying) as shown in Figure 3.18, two peaks at 0.05 and 0.2 V were attributed to the phase transition between Li_xSi alloys and the formation of amorphous Li_xSi phase, respectively. In a similar manner, during the discharge (Li dealloying), two peaks at 0.3 and 0.5 V were attributed to the phase transition between Li_xSi alloys and the formation of amorphous Si by the delithiation step. Figure 3.18b presents stable reversible capacity with higher than 2000 mAh g^{-1} and Coulombic efficiency of 100% upon 100 cycles.

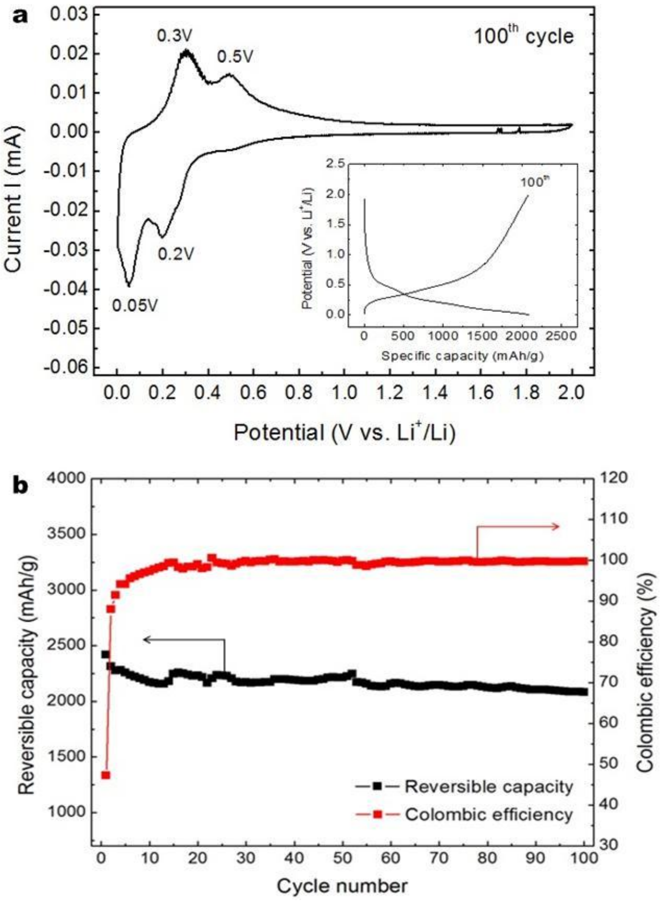

Figure 3.18 (a) Cyclic voltammogram (scanning rate, 0.2 mVs^{-1}) and (b) Cyclic performance of SiN_x anode on a $FeCl_3$-etched Cu cycled at 1C rate.

3.4.5 Thickness effect in the anode materials

The increase in film thickness is desired for practical uses in batteries. Figure 3.19 shows the cycling performance of 250 nm, 500 nm, and 1 μm PECVD nitride anodes deposited at 100 ℃ and 25 W RF power. The discharge capacity at the 100th cycle was 2100, 1880, and 1450 mAh g-^{1}, respectively. The samples were tested at 0.6 C. The 250 nm and 500 nm samples showed high capacity retention (~100%) upon 100 cycles compared to 1 μm nitrides (76%). Thick films showed a lower discharge capacity due to higher electrical resistance (and ohmic drop) [58, 105]. Thick films also showed a poor cycling performance that was associated with the stress induced material degradation.

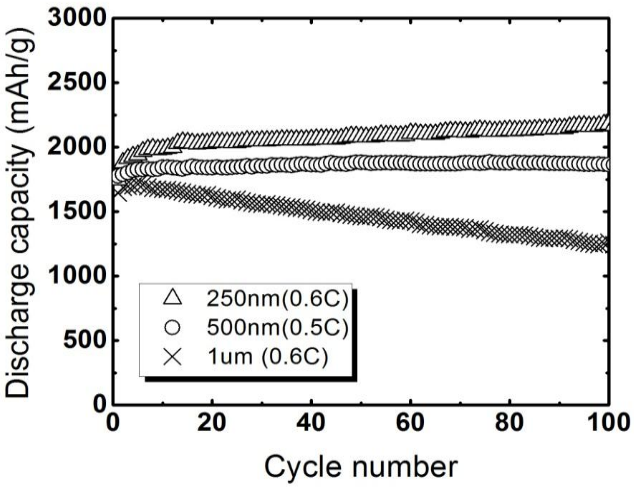

Figure 3.19 The cycling performances of 250 nm, 500 nm, and 1 μm PECVD nitride anodes during 100 cycles. All three films were deposited at 25 W power and 100 ℃.

Figure 3.20 shows SEM images of three different samples after 30, 100, and 300 cycles. The crack size became larger when increasing the thickness of film. In the 250 nm film, unlike the thicker films, the crack size did not change a lot upon 100 cycles. This revealed that the stress induced cracking rises due to the increase in film thickness. Thickness changes up to 1 µm did not exacerbate cycling stability in SiN_x films. We assume that the presence of nitrogen incorporated into the film creates a lithium inactive phase that anchors the substrate during cycling. In additional, the presence of nitrogen decreases the specific capacity of the anode material. Lower capacity decreases the strain associated with the stress induced cracking and reduces electrical contact loss at the interface with the substrate.

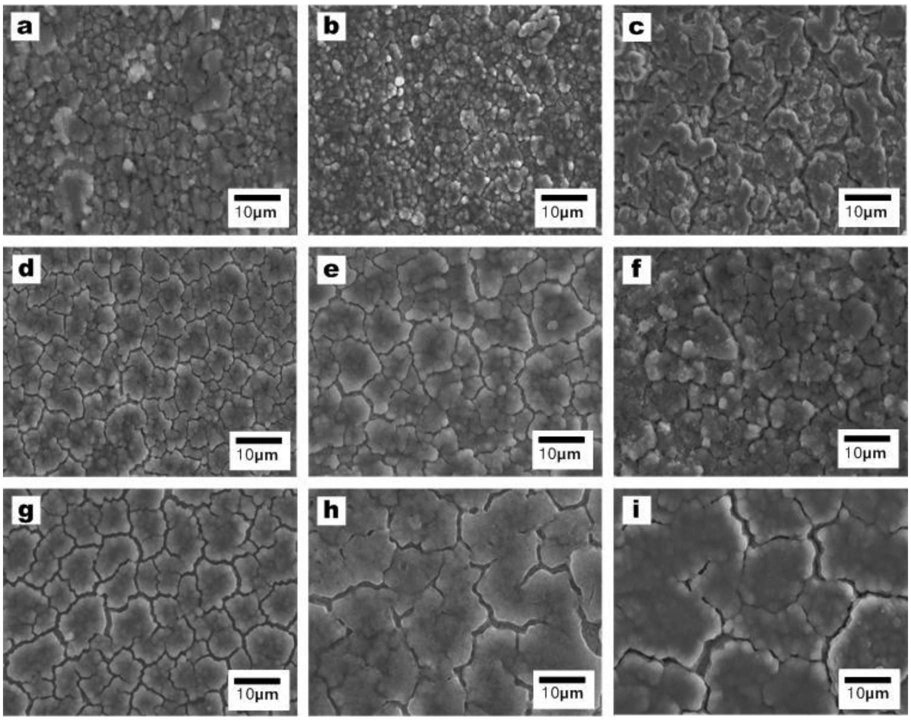

Figure 3.20 SEM images of (a) 250 nm SiN_x films after 30 cycles, (b) after 100 cycles, and (c) after 300 cycles, (d) 500 nm SiN_x films after 30 cycles, (e) after 100 cycles, and (f) after 300 cycles, (g) 1 µm SiN_x films after 30 cycles, (h) after 100 cycles, and (i) after 300 cycles. All the films were deposited on the etched Cu.

Figure 3.21 shows 500 nm SiN_x anode cycled at 0.5 and 1C rate. The film cycled at 0.5C showed higher initial capacity of 1775 mAh g^{-1} and stable cyclability. The capacity retention were 93 and 92 % for films cycled at 0.5 and 1C, respectively. However, the film cycled at 1C showed capacity fading at the end of cycles (200-300 cycle). This implies that the films cycled at higher cycling rate shorten the cycle life. High current rate might prevent full lithiation through the whole body of the film. Therefore, a longer time is required for the lithium ions to insert into the complete depth of the silicon film.

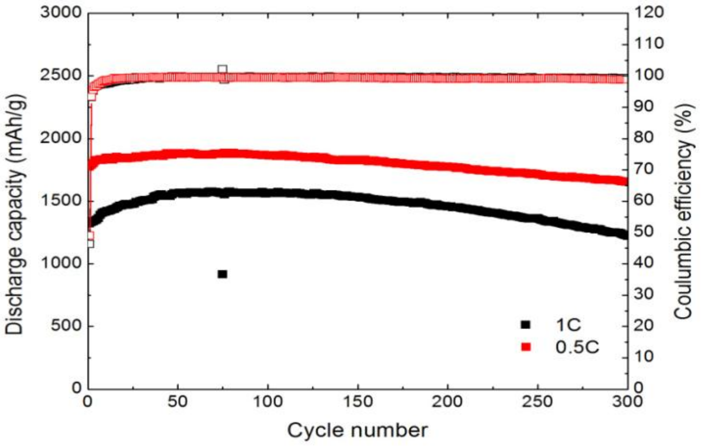

Figure 3.21 Cyclic performances of 500 nm SiN_x films depending on the C-rate (0.5C and 1C).

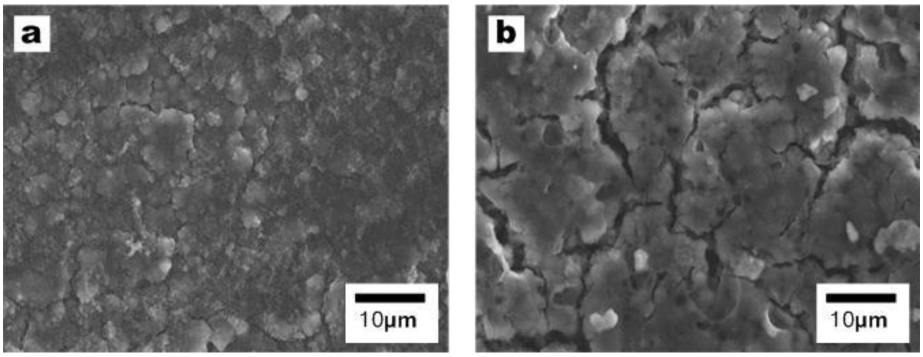

Figure 3.22 SEM images of 500 nm SiN_x films (a) tested at 0.5C, and (b) tested at 1C upon 300 cycles.

Figure 3.22 shows SEM images of 500nm films tested at 0.5C and 1C upon 300 cycles. When applying the higher current rate (1C), in Figure 3.22b, the film delaminates more actively than the film tested at lower cycling rate. There are different sizes in crack spacing among islands. The larger crack spacing it has, the more electrical contact loss arise.

The SEM results are corresponding to the cyclic performance plots. Increasing capacity at the beginning for the film cycled at 1C is attributed to cracking and island formation in surface layers, allowing uncycled silicon to become accessible to lithium ions. In addition, decreasing slope in capacity at the end is also due to electrical contact loss caused by the pulverization of the material and crack formation.

CHAPTER 4. DEVELOPMENT OF IN-SITU CHARACTERIZATION SYSTEMS

4.1 Literature review of the stress measurement in lithium ion battery anodes

In order to engineer better anode systems, understanding failure mechanisms of material is critical. Because silicon undergoes huge volume expansion and contraction upon lithiation/delithiation, study of the stress evolution becomes important [106]. While there have been many attempts to engineer new nanostructures and nanocomposites for the improvement of mechanical integrity and cycling performance [43, 66], the main challenge is the lack of techniques for in-situ characterization of lithiation and delithiation processes [107, 108]. The in-situ characterization techniques are critical for future energy storage because they enable the optimization of electrode configuration as well as the development of control algorithms.

In-situ monitoring of microstructure change during charge/discharge have been investigated in the literature [109, 110]. However, the studies provided limited quantitative information. For example, Lee and coworkers monitored the stress effect in Si anodes using a deflection of cantilevers that is coupled with single laser beam and an optical sensor [108]. An incident laser beam hit the surface of the sample/cantilever and reflected to a photo diode. The reflected beam spot changed its position due to the deflection of sample subjected to the film stress. The translation of the beam signal from the detector was then converted to the voltage signal. Figure 4.1 shows their voltage profile data and a corresponding stress profile. With the cantilever, they observed the, stress was induced at the lower voltage range, and therefore cyclic performance was improved by limiting the lower cut-off voltage to 0.1V. In Figure 4.1a, the compressive stress increased steeply at the initial stage of Li insertion when the cell voltage reached 0.3V. It was due to the formation of Li_2Si phase, having doubled volume expansion near the interface between the Si film and the electrolyte. In the voltage region between 0.3 and 0.1V, the compressive stress began to increase in a reduced slope indicating plastic deformation, due to the Li_2Si phase over the film. Under the cell voltage of 0.1V, the compressive stress started decreasing because the stress was relieved by the formation of $Li_{4.4}Si$ phase with its four times volume expansion causing the film to crack. In Figure 4.1b, after limiting the lower cut-off voltage to 0.1V, the stress variation was not observed, indicating that the lithiation process was done without film cracking. The study only showed the voltage signal of the photodetector vs time, which was only qualitative information.

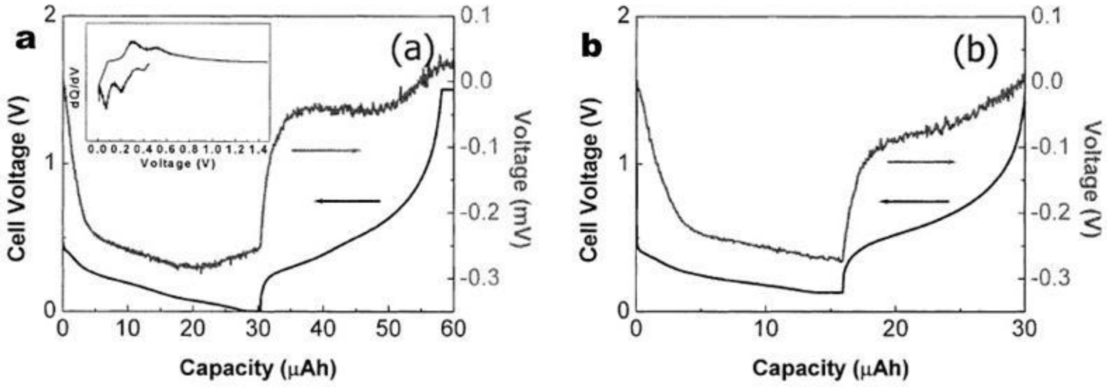

Figure 4.1 Voltage and stress profiles at cut-off voltages of (a) 0-1.5V, and (b) 0.1-1.5V. Inner box in (a) is cyclic voltammetry.

Alternative attempts have been made to replace the single-point beam deflection measurement with a multi-beam optical sensor (MOS) method [92, 107, 111-113]. A MOS system utilizes an array of parallel laser beams and measures the relative changes of the spacing distances between the beam spots. This method is less sensitive to vibrations compared to the conventional cantilever beam deflection system [114]. Guduru and coworkers demonstrated the stress evolution in Si anodes by monitoring the substrate curvature changes using the MOS system, as shown in Figure 4.2a [92]. The stress σ_f related to the substrate curvature K change is given by the Stoney's equation (equation 4.1),

$$\sigma_\mathrm{f} = \frac{E_\mathrm{s} h_\mathrm{s}^2 K}{6 h_f (1-v_\mathrm{s})} \qquad (4.1)$$

$$K = \frac{d-d_0}{d_0}\frac{1}{A_\mathrm{m}} \qquad (4.2)$$

where h_s and h_f are the substrate and film heights; E_s and v_s are the Young's modulus and the Poisson's ratio of the substrate, respectively. The Stoney's equation is only valid when the thickness of the film is much smaller than that of the substrate. Curvature K can be calculated from the distance changes between two adjacent laser spots divided by the mirror constant A_m (equation 4.2). Figure 4.2c shows the stress profile of the 250 nm thick *a*-Si cycled at C/4 rate. The compressive stress increased steeply during the initial charging process, and reached to -1.75 GPa, indicating the elastic limit of the film stress. Then the stress decreased with lithiation, reaching about -1 GPa at the lower cut-off voltage. Upon delithiation, the tensile stress response was similar to the compression. In their calculation, the final film thickness due to volume expansion had been taken into consideration. Their assumptions included that the film thickness in Si increased linearly with the state of charge and the maximum volume expansion was 370%. Therefore, the film thickness is $h_\mathrm{f} = h_\mathrm{f}^0(1+2.7z)$, where z is the state of charge and h_f^0 is the initial film thickness.

There were two issues about wafer curvature measurement. First, the measurement was based on the average stress of active materials on a wafer scale (50.8 mm diameter, 500 μm thick). Second, the stress measurement was not sensitive enough to distinguish the formation of solid-electrolyte interfaces (SEI) and that of silicon-lithium alloys, which is critical for the design of Si-based anodes.

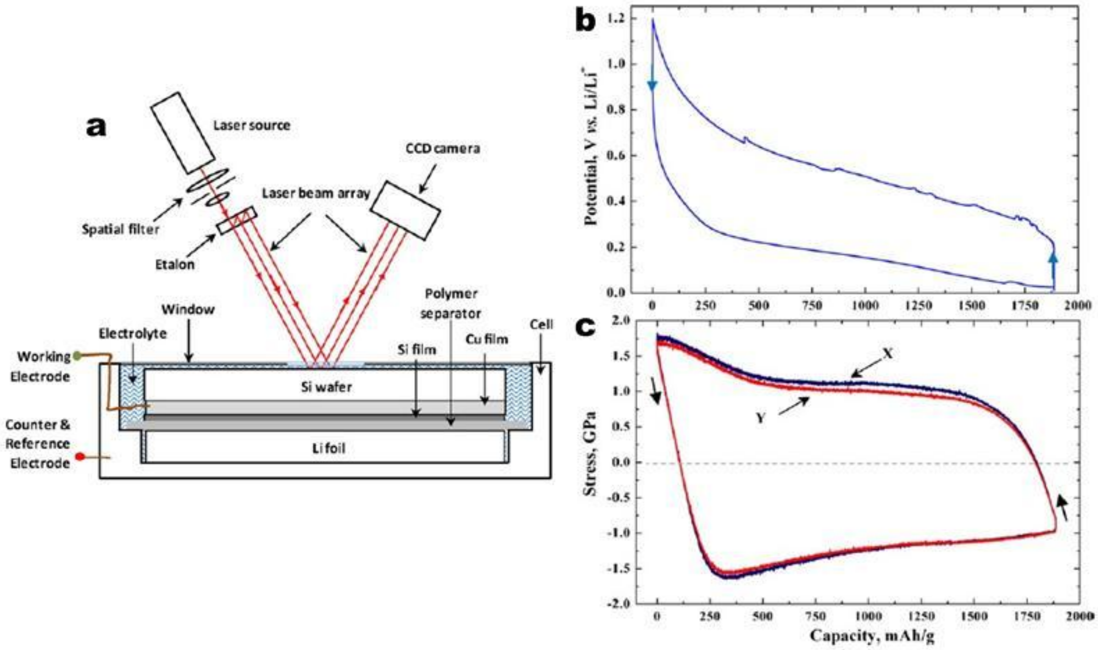

Figure 4.2 (a) A schematic diagram of the electrochemical cell and the MOS setup. (b) Voltage profiles and (c) stress variation profiles [92].

Since Guduru group investigated the stress evolution in Si thin films using MOS system, they have applied this technology to other electrode materials such as crystalline Si films and graphite powder anodes [111, 115]. Gao and coworkers previously reported patterning Si thin film electrodes up to critical sizes of the crack spacing in order to prevent further film cracking [46]. Likewise, after the successful improvement, Gao attempted to perform the in-situ stress measurement on the patterned electrodes using MOS system to see if better performances were able to be attributed to the stress accommodation due to the decrease in the maximum stress and the elimination of the plastic flow [112].

4.2 Measurement system (white light interferometry)

White light interferometry (WLI) is a traditional technique for optical profilometry. This optical measurement system has several advantages compared to the mechanical profilometry, including noncontact scanning of micro-scale features, superior height resolution, and high speed measurement [116]. A schematic diagram of the WLI system is shown in Figure 4.3 [117]. The incoming light source is split inside the interferometer. One beam goes to an internal reference and the other goes to the sample surface. After reflection, the beams combine inside the interferometer and experience constructive and destructive interference. Bright and dark fringe patterns (interference fringes) were generated by the difference of the optical path between the beams reflected from the reference and the sample. The fringe patterns are captured by a CCD camera, representing the surface topography of the sample.

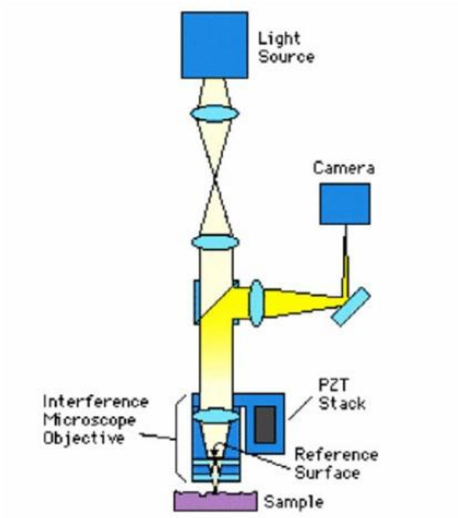

Figure 4.3 Schematic diagram of a WLI system [117].

4.3 Experimental

The fabrication of the bilayer cantilever structure includes two photolithography steps. Figure 4.4 illustrates the fabrication processes. (a) A 250 nm thick *a*-Si was deposited on the as-prepared copper foil using E-beam evaporation at room temperature. (b) The *a*-Si coated copper foil was glued to a silicon wafer using a photoresist (AZ4620, Hoechst). (c,d) A photoresist (S1811, Shipley) was spin-coated and patterned by photolithography. (e) An *a*-Si layer was etched using reactive ion etching (SF_6). (f,g) Afterward, photolithography was performed. (h) The copper foil was selectively etched by a copper etchant (APS100, Transene). The cantilever was released by removing photoresist using Acetone.

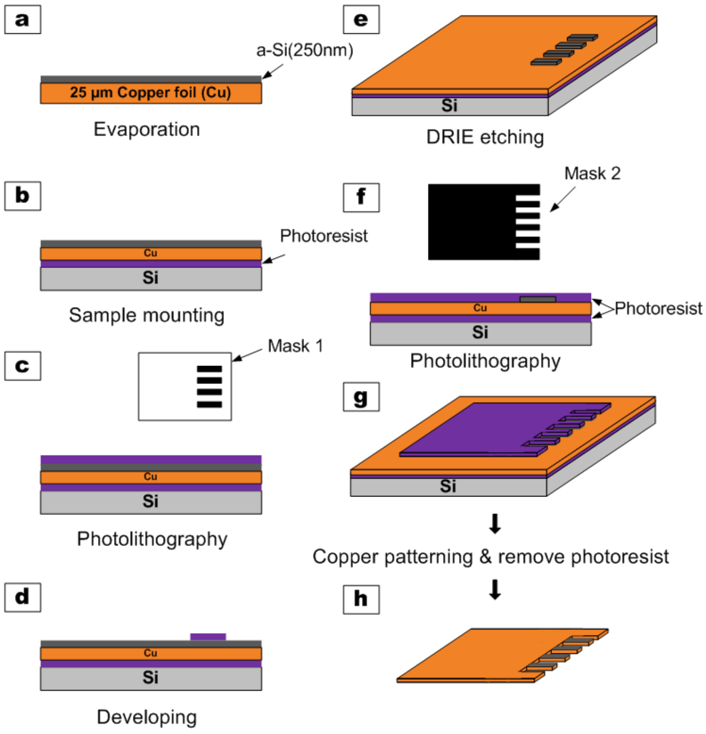

Figure 4.4 Fabrication process of the bilayered cantilever (*a*-Si on copper).

Figure 4.5 shows the measurement setup, where a WLI (ContourGT In-Motion Bruker) was used to measure the deformation of the cantilever during electrochemical cycles controlled by a potentiostat (Gamry G300). In the WLI setup, the measurement of the cantilever structure in liquid requires a compensation chamber [118]. The cantilever anode was mounted in the electrochemical cell (See Figure 4.5a and b). The active material (*a*-Si) was used as a working electrode, and faced lithium metal (as a counter and a reference electrode). A separator was placed between two electrodes in order to prevent a short circuit. A liquid electrolyte (1 mol $LiPF_6$ in ethylene carbonate (EC) and dimethyl carbonate (DMC) with 1:1 ratio) was used to fill in the cell.

The charge/discharge measurement was performed at a constant current density of 22 A/g equivalent to 1C rate and the voltage ranged from 0.02-2 V versus Li^+/Li at room temperature. After electrochemical cycling, we disassembled the cell and rinsed the material with dimethyl carbonate (DMC). The surface morphology of the silicon film was analyzed by SEM (JEOL JSM-6510LV) at a 15kV acceleration voltage.

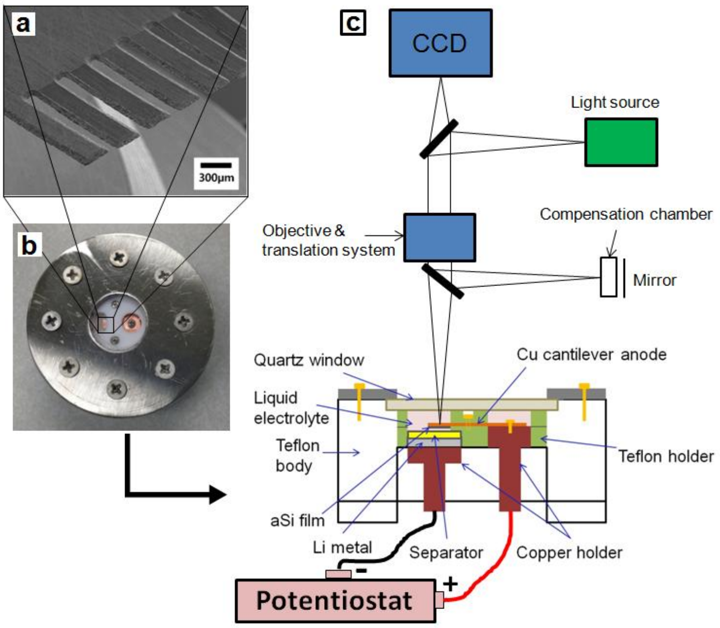

Figure 4.5 Measurement setup of the in-situ measurement system. (a) SEM of the cantilever anode, (b) Top view of the customized electrochemical cell, (c) White light interferometry and chronopotentiometry setup.

4.4 Analysis model

The stress of *a*-Si during charge and discharge was measured by in-situ monitoring of the curvature change of cantilevers caused by surface absorption and/or volume change of Si-Li alloy formation (as shown in Figure 4.5). Figure 4.6 illustrates the working principle of a bilayer cantilever that consists of an active material and a copper substrate. Copper has widely been used as a common current collector for the anode in lithium ion batteries. Copper is mechanically elastic with a high yield strength (116 MPa) [119]. The surface absorption and/or volume expansion of Si-Li alloys cause a free-standing cantilever to bend [120]. The bending of a bilayer cantilever was described by the Timoshenko beam theory.

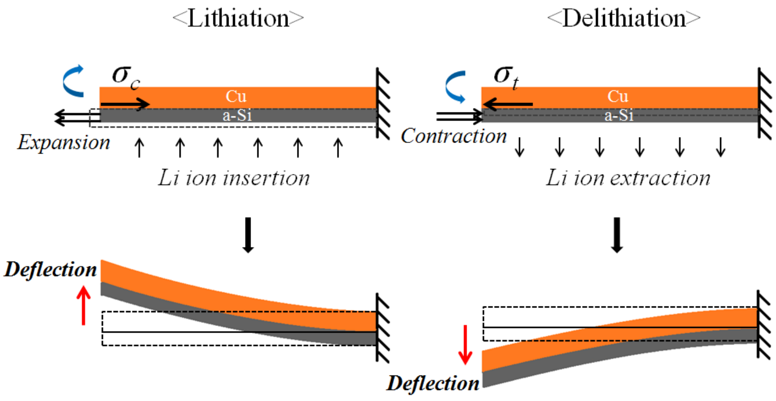

Figure 4.6 The bending of the bilayer cantilever during lithiation and delithiation. (σ_c: compressive stress, σ_t: tensile stress)

The deformed bilayer cantilever will create a curvature with a radius ρ after experiencing the stresses that contribute to the strains of the two films. In the case of the thermal expansion, the strains are determined by the temperature change ΔT and the difference of the thermal expansion coefficient between the two films $\Delta\alpha_\mathrm{f} = (\alpha_1 - \alpha_2)$ [103]. The curvature k can be expressed in terms of the thermal strain, $(\alpha_1 - \alpha_2) \cdot \Delta T$, as

$$k = \frac{1}{\rho} = \frac{6(1+m)^2 \cdot (\alpha_1 - \alpha_2) \cdot \Delta T}{h_\mathrm{t} \cdot [3(1+m)^2 + (1+mn) \cdot \left(m^2 + \frac{1}{mn}\right)]} \qquad (4.3)$$

where h_t is the total thickness of the bilayer cantilever, $n=E_1/E_2$, and $m=h_1/h_2$. E_1 and E_2 are elastic moduli of the deposited film and the substrate, respectively. In our study, the mechanical stress is induced by the volume changes during electrochemical cycling, the thermal strain, $(\alpha_1 - \alpha_2) \cdot \Delta T$, is replaced by the strain ε_f. The linear relationship between the strain and the stress σ_f can be expressed as $\sigma_\mathrm{f} = E\varepsilon_\mathrm{f}$, where E is the elastic modulus of the film.

The surface absorption and/or the volume expansion of a-Si cause a free-standing cantilever to bend. The analytic solution of a bilayer cantilever subjected to stress can be derived as a following equation,

$$\sigma_\mathrm{f} = \frac{k \cdot E_1 \cdot h_\mathrm{t}[3(1+m)^2 + (1+mn)\left(m^2 + \frac{1}{mn}\right)]}{6(1+m)^2} \qquad (4.4)$$

The assumptions include (1) the deformation of copper is within an elastic range. (2) the friction at the support is ignored, and (3) the width of a cantilever is small compared to its length [121]. The thickness of the active material depends on the state of charge, and is expressed as $h_\mathrm{si} = h_\mathrm{si}^0(1+\beta z)$, where z is the state of charge ($0<z<1$), and h_si^0 is the initial thickness of Si. The β is 2.7 when the maximum volume expansion is 370% for fully lithiated silicon ($Li_{3.75}Si$), equivalent to a specific capacity of 3579 $mAhg^{-1}$ [122, 123]. In this work, the quantity of the volume change was estimated by using Coulomb counting. Because of constraint by the substrate, only the height of the a-Si is assumed to change upon lithiation and delithiation. The Young's modulus of the a-Si film also varies depending on the state of charge. The Si-Li alloy is softer than the pure a-Si (90 GPa). According to the density function theory [120], the elastic modulus of the fully lithiated $Li_{3.75}Si$ has been calculated to be 34 GPa.

The interferometer enables the monitoring the three-dimensional deformation of the whole cantilever. The fidelity of the measurement is high compared to optical-lever detection used in Lee's work, which is single-point deflection [108]. 3D interferometry images of the cantilever before and after the 1st charge and discharge are shown in Figure 4.7. Typically maximum deflection of the tip of the cantilevers was ca. 3 µm after a full charge. During the

1st cycle, the beam curled up during the charge and curled down during the discharge. This implies that the volume expansion and contraction reversibly take place during each cycle.

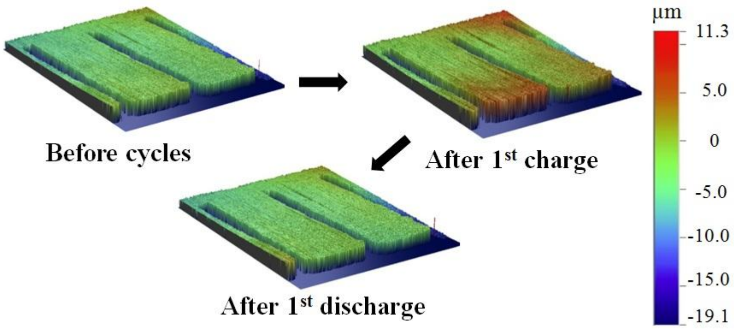

Figure 4.7 3D interferometry images of the cantilever anodes during the first cycle.

CHAPTER 5. IN-SITU NANOMECHANICAL CHARACTERIZATION OF SILICON THIN FILMS ON ROUGHENED CURRENT COLLECTORS FOR LITHIUM ION BATTERY APPLICATIONS

5.1 Introduction

The demand to increase the energy and power density in lithium ion batteries for consumer electronics and electric vehicles has attracted intense interests to develop high capacity electrodes. Silicon is an attractive candidate for anodes thanks to its high specific capacity (3579 mA g^{-1}) and low cost. However, the large volume expansion (~370%) associated with silicon-lithium (Si-Li) alloy formation causes pulverization of electrode material and poor cyclic performance. Recently, engineering nanostructures and thin films has been found an appealing approach to overcome material degradation [41, 44, 50, 106]. Silicon nanostructures have shown to accommodate large volume expansion and to mitigate mechanical stress [21, 42, 45, 47]. Nevertheless, the capacity retention of silicon-based anodes over many cycles is still problematic [39]. Two of the challenges include the loss of electrical contact among active materials and delamination of material from the substrate (current collector).

In order to minimize electrical contact loss between the silicon active material and the current collector, several studies have been conducted to optimize the architecture of current collectors, including roughening the substrates by mechanical or chemical treatments [80, 124-128] as well as three-dimensional substrates such as metal foams and porous copper [129-132]. The cyclic performance of silicon anodes has shown to be improved on the roughened substrates. The improvement was attributed to better adhesion between the active material and substrates. However, there has been no in-situ study to quantify how the roughened substrate accommodates the volume expansion of Si-Li alloy and mitigates the stress. Not surprisingly, there have been few tools for in-situ stress measurements in battery research.

Lee et al. adapted cantilevers to monitor 35 nm Si anodes during charge and discharge [108], but the study did not provide any quantitative information. Sethuraman et al. studied the stress evolution of thin film Si anode using the curvature change of substrates and Stoney's equation [92, 111]. They found that the compressive yield strength reaches -1.75 GPa and the Si film begins to flow plastically. With further lithiation, the stress eventually decreases to -1 GPa. However, the measured stress was an average value over a wafer-scale substrate. In their experiment, the stress variation is developed by the only lithiated Si and the profile includes elastic and plastic responses. To the best of our knowledge, all these measurements were not sensitive enough to distinguish critical electrochemical processes, such as solid-electrolyte interphase (SEI) and Si-Li alloy formation. SEI is a passivation layer that forms on the electrode surface during the first cycle due to the decomposition of electrolytes [22, 38]. On the other hand, SEI is electrically insulating and protects stored lithium atoms from electrolytes.

In this work, electrochemical processes of silicon active materials were evaluated on the pristine and roughened copper substrates during the charge and discharge. The processes are monitored using a bilayered cantilever made of silicon and copper. The mass of SEI layers and mechanical stress of Si-Li alloys cause the bending of cantilevers where the surface profiles of the beams are measured in real time using a white light interferometer.

5.2 Experimental

25μm thick copper foil was purchased from Lyon Industries Inc. The copper foil was first chemically etched by 0.1 M ferric chloride ($FeCl_3$) for 5 min. After etching, the copper foil was rinsed with DI water and isopropyl alcohol (IPA). The sample was dried on a heater at 70 ℃ for 5 min. The surface roughnesses before and after the chemical etching were characterized by an atomic force microscope (AFM, Veeco Dimension 3100). The average roughness was measured in a tapping mode and defined by the root mean square value from the profile. A 250 nm thick amorphous silicon (*a*-Si) was thermally evaporated by E-beam evaporation (Temescal BJD 1800) with a deposition rate of 2 Å sec^{-1}.

The electrochemical characteristics of the *a*-Si were measured by a half-cell configuration. All the cell assembly and electrochemical testing were performed in a glove box filled with ambient Argon. The cell was assembled using a CR2032 coin cell. Lithium metal (Alfa Aesar) was used as counter and reference electrodes. A polyethylene separator (Celgard 2320) was soaked overnight in the liquid electrolyte (1 mol $LiPF_6$ in ethylene carbonate (EC) and dimethyl carbonate (DMC) with a 1:1 ratio) over night. The charge and discharge tests were performed using a potentiostat (Maccor Model 4200) at a constant current density of 2 A/g and the cut-off voltage was set 0.02 V and 2 V versus Li^+/Li. After electrochemical tests, the cells were disassembled and then rinsed with DMC solvent. SEM (JEOL JSM-6510LV) was used to image surface morphologies of samples before and after cycling. The acceleration voltage was 15 kV in SEM.

Two kinds of copper foil (25 µm thick) were prepared: one was pristine, and the other was chemically etched ($FeCl_3$). For the fabrication of the cantilever, see Figure 4.4. A free-standing cantilever composed of copper (Cu) and active material (*a*-Si) was placed in a home-made liquid cell. The cantilever faced lithium metal covered by a separator (Celgard 2320) with a space filled with an electrolyte. The presence of the separator and a Teflon spacer prevents a short circuit between the anode and lithium metal. Copper serves as both a current collector and a mechanical support. During the lithiation (charging), Li ions are driven from lithium metal to anode through the electrolyte by the electrochemical potential differences between the two counter electrodes. A white light interferometry (ContourGT In-motion, Bruker) was used to measure the curvature of the cantilever during electrochemical cycling controlled by a potentiostat (Gamry G300).

5.3 Results and discussion

The roughnesses of copper before and after $FeCl_3$ etching were measured by AFM (Figure 3.2). The root-mean-square roughnesses (R_q) of the pristine and etched copper were 17 nm and 182 nm, respectively. The roughnesses of the samples after *a*-Si deposition became 16 nm and 187 nm, respectively, suggesting that *a*-Si was uniformly evaporated. Scotch tape tests were performed. The *a*-Si deposited on etched copper had better adhesion compared to that on pristine copper (Figure 5.1).

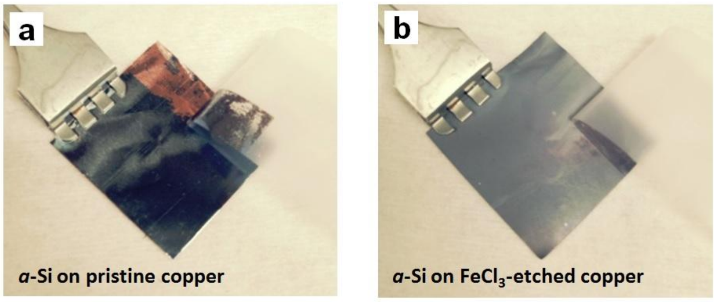

Figure 5.1 The adhesion tests (scotch tape) of the *a*-Si films on (a) the pristine copper and (b) $FeCl_3$-etched copper.

Figure 5.2 shows the first-cycle charge and discharge curves of 250 nm *a*-Si films deposited on the pristine and etched copper, and their corresponding stress profiles. During the initial lithiation, the voltage dropped rapidly until a voltage plateau appeared below 0.35 V. On the other hand, the stress was small when the voltage was above 0.35 V, but increased dramatically below 0.35 V. The stress profile indicates two distinct electrochemical processes at 0.35 V. It is known that solid-electrolyte interphases (SEI) formed on electrodes in the beginning of the first cycle [22, 38]. The passivation of SEI layers caused negligible stress, and protected lithium ions from electrolytes.

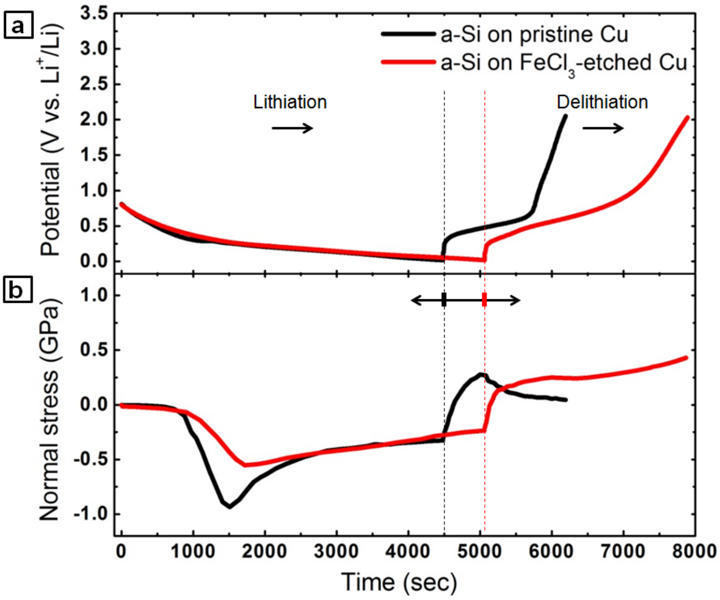

Figure 5.2 (a) The voltage and (b) in-situ stress profiles of the *a*-Si films on the pristine (black) and $FeCl_3$-etched copper (red) cantilevers in the liquid cell chamber.

Below 0.35 V, compressive stress increased rapidly. The insertion of lithium in silicon caused volume expansion, resulting in compressive stress. At the beginning of the Si-Li alloy formation, the stress began increasing linearly over time, where the strain was proportional to lithium concentration in Si. For *a*-Si on the pristine copper (black line), the compressive stress reached a maximum value of -0.94 GPa. The yield strength of lithiated silicon was reported to be ca. -1 GPa [85, 92]. With further lithiation, silicon began to flow plastically to accommodate additional volume changes. The stress eventually dropped to -0.33 GPa. Upon delithiation, the removal of lithium caused volume decrease, generating tensile stress. Initially, the tensile stress (black line) increased rapidly until it reached a maximum value of 0.28 GPa. The stress dropped rapidly with further delithiation due to Si fracture [133]. In a similar experiment, where the cantilever was flipped over to let Si face the glass, the stress dissipation was observed at a similar voltage (Figure 6.4). After cracking formation, the stress was relieved. In addition, the negligible stress above 0.7 V suggested that most Si lost electrical contact with copper.

The stress profile (red line) for *a*-Si on roughened copper was different from that on pristine copper. Above 0.35 V during lithiation, the stress profile of *a*-Si on roughened copper was shown to be similar to that on pristine copper. When Si started to react with Li below 0.35V, the compressive stress increased linearly but the slope was smaller than that of the pristine sample. The stress was reduced because the rough surfaces allowed the transverse coupling between in-plane and out-of-plane strains of silicon volume expansion [134, 135]. The stress reached a maximum value of -0.58 GPa, and gradually dropped to -0.25 GPa during the plastic deformation. Interestingly, the stress of *a*-Si on the pristine copper dropped faster than that on the roughened copper. Using SEM (Figure 5.6b), wrinkling of *a*-Si on the pristine copper was found. The compressive stress caused delamination and buckling of the *a*-Si films on the pristine copper. On the other hand, the *a*-Si adhered well to the roughened copper. Small *a*-Si islands (diameter 6-7 μm) were observed as shown in Figure 5.6c. These silicon islands had good electrical contact with copper, and the lithiation time was longer than the pristine sample. Upon delithiation, the tensile stress of the *a*-Si on the roughened copper initially increased, and began to flow plastically when the voltage was above 0.46 V. The stress eventually reached a maximum value of 0.4 GPa at the end of delithiation. The stress measurement suggested *a*-Si films were in good electrical contact with the roughened substrate. On the other hand, *a*-Si on pristine copper lost its electrical contact after the first cycle and no capacity was found. The delithiation time was approximately three times longer than the pristine sample.

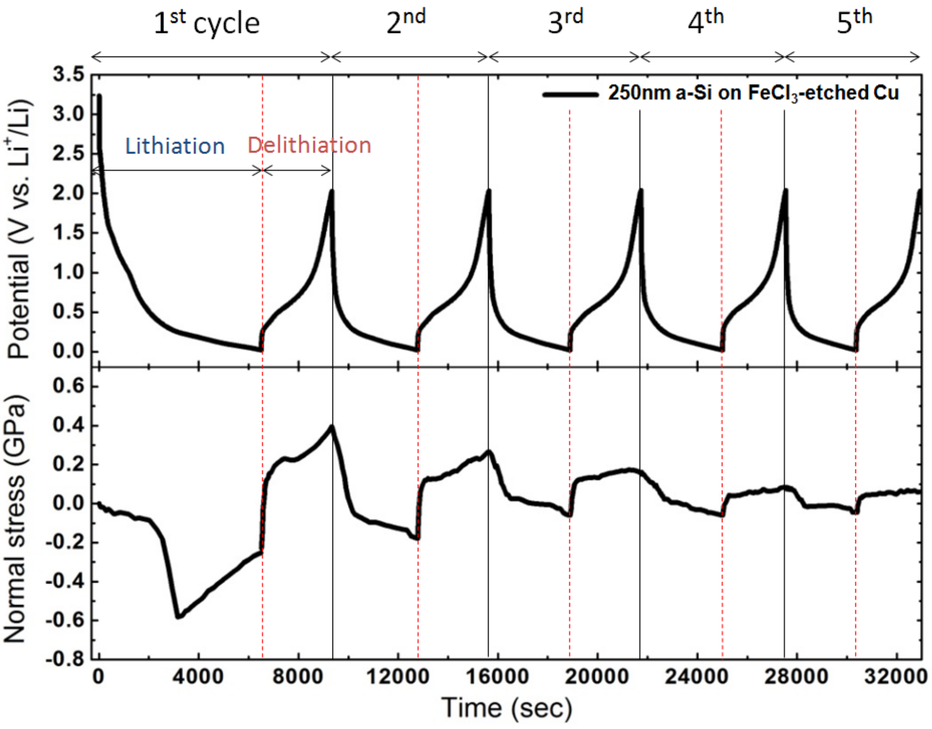

Figure 5.3 (top) The voltage and (bottom) in-situ stress profiles of the *a*-Si film on the $FeCl_3$-etched copper during 5 cycles.

Figure 5.3 shows the cell voltage and stress evolution of the roughened sample during the first five cycles. Upon the 2nd lithiation, compressive stress increased immediately, which indicates Si-Li alloy formation. This suggests that most SEI was formed during the first cycle. The stress increased linearly to -0.1 GPa, and slightly further increased to -0.13 GPa during plastic deformation. The compressive stress was much smaller than that of the first lithiation. Combined with SEM images, the study suggests that the major cracking occurred during the first lithiation, where the stress was relieved. The *a*-Si films were adhered strongly to the substrate after cracking and formed small Si islands. Because of the small disconnected islands, the stress was very small compared to the first cycle. Interestingly, the stress reached a maximum value of -0.2 GPa when the voltage was below 50 mV. The increase in stress was probably due to a phase transition of Si-Li alloy to a new crystalline phase, which has been demonstrated by XRD studies in the literature [38]. Upon the 2nd delithiation, the tensile stress reached nearly 0.13 GPa and further increased to 0.26 GPa. The stress evolution in the first five cycles was shown to have dynamic electrochemical processes over time. The stress was gradually relaxed over five cycles due to material degradation, and changes of morphology and chemical properties.

Figure 5.4 shows the SEM images of a-Si films on the pristine and roughened copper after cycling. The a-Si on the pristine copper was shown to have large disconnected islands after the first cycle (Figure 5.4a). Some islands were peeled off during the cell disassembly. In comparison, Si was still in contact with the roughened copper after 5 cycles (Figure 5.4b). Separated Si islands with smaller areas were observed on the roughened copper. The literature reported that there is a critical cracking size for a Si thin film electrode [46, 112],

$$L_{\mathrm{cr}} = \frac{2\sigma_{\mathrm{Y}}^{\mathrm{Si}}}{\tau_{\mathrm{cr}}^{\mathrm{int}}} h \qquad (5.2)$$

where h is the thickness of Si film, $\sigma_{\mathrm{Y}}^{\mathrm{Si}}$ (0.6-0.94 GPa) is the yield strength of Si, and $\tau_{\mathrm{cr}}^{\mathrm{int}}$ (40 MPa [136]) is the interfacial shear strength between the lithiated Si and the substrate. The calculated crack spacing for 250 nm thick Si film was 7.5–11.8 µm. However, experiments (Figure 5.4a) showed that the cracking size was approximately 30-40 µm. The error might be attributable to the overestimated interfacial shear strength between a-Si and the pristine copper due to its poor adhesion. On the other hand, the interfacial shear strength increases as the surface roughness increases, resulting in a smaller cracking size. The experiment showed the crack size of 250 nm a-Si on the roughened Cu was 6-7 µm after the first lithiation. This study suggests that the surface roughness of the current collector provides a major role on the mechanical properties.

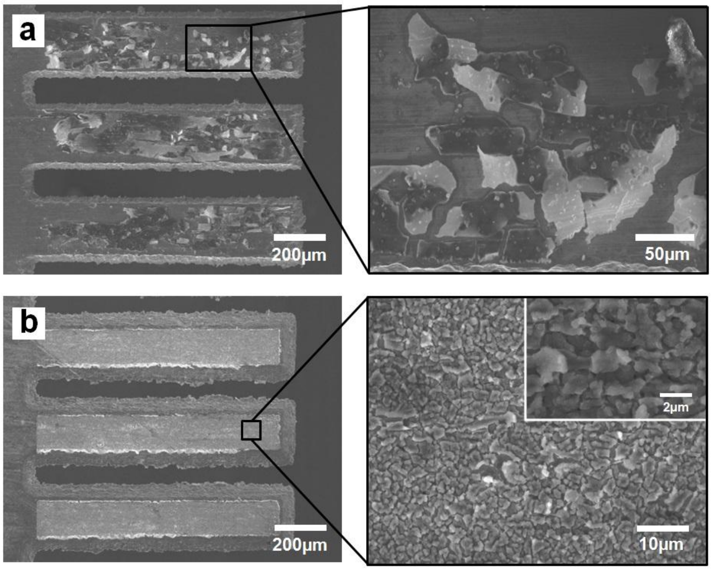

Figure 5.4 The SEM images of (a) the *a*-Si film on the pristine copper cantilever after 1 cycle and (b) the film on the FeCl$_3$-etched copper cantilevers after 5 cycles.

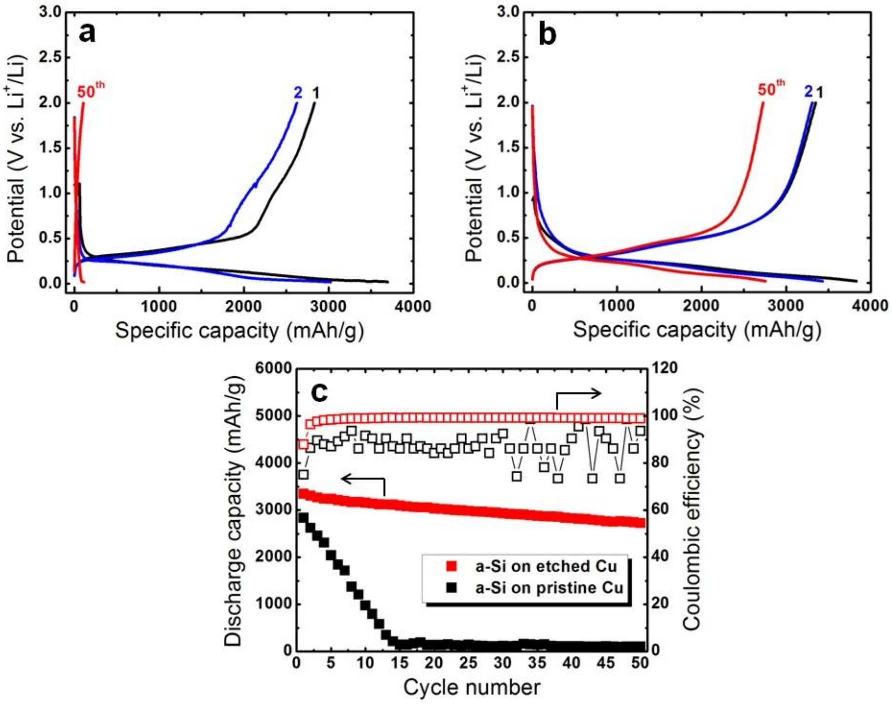

Figure 5.5 The electrochemical properties of the evaporated *a*-Si films on the (a) pristine copper , and (b) FeCl$_3$-etched copper, cycled at a rate of 2 A/g (1C) between 0.02 V and 2.0 V vs. Li$^+$/Li in the coin cell. (c) Cycle performances of the a-Si anodes on two different types of copper substrates upon 50 cycles.

The energy release rate is the energy dissipated during fracture per unit of newly created fracture surface area, and is independent from the applied loads and material geometry. By assuming interfacial sliding at the interface between the thin films and substrates, the energy release rate has been derived by Hu et al [137],

$$G = \left[\frac{\sigma}{3\tau_0} + F(\Sigma) \right] \frac{\sigma^2 h_f}{E_f} \qquad (5.1)$$

where σ, h_f ,and E_f are the normal stress (compression or tension), thickness and Young's modulus of the silicon film, respectively, $F(\Sigma)$ is a function of the Dundurs parameters, and τ_0 is the interfacial sliding strength (or shear strength) between silicon and copper. Dundurs parameter represents the elastic mismatch between the film and substrate. On the pristine copper, the silicon volume expansion tends to produce a sliding failure along a plane that is parallel to the direction of the force. The shear strength is often used to characterize the quality of adhesion between the material and substrate [138].

Although the τ_0 varies with boding of the interface, the value can be estimated using both the shear flow stress of Cu (40 MPa [139]) and the interfacial friction strength of the silicate composite (40.5 MPa [136]). The fracture was observed at the peak tensile stress in this work (Figure 6.4d). Thus, the tensile stress at the onset of the stress plateau was chosen for the value. Using a value of τ_0 = 40 MPa and $F(\Sigma)$ = 1.5 [133, 140], the fracture energy of the *a*-Si on the pristine copper was estimated to be 4.9 J m^{-2}. The interfacial sliding strength can be enhanced by roughening the copper. Therefore, the fracture energy of *a*-Si on the roughened copper was expected to be smaller.

The samples were tested in coin cells. Figure 5.5 shows the charge and discharge curves of evaporated *a*-Si films deposited on the (a) pristine and (b) $FeCl_3$-etched copper, and (c) their cycling performance. The films were cycled at 1C, which referred to one-hour charge. In this study, cathodic lithiation in the anode was referred to charge. After the initial

15 cycles, the discharge capacity of the *a*-Si on the pristine copper became negligible owing to the loss of electrical contact. In contrast, the *a*-Si on the $FeCl_3$-etched copper showed stable cyclability upon 50 cycles, resulting in capacity retention of 81%. Figure 5.6 summarizes the mechanical behaviors of *a*-Si films on the pristine and roughened copper. This study suggests that the surface treatment of the current collector also plays a role in the cycling performance of the battery materials.

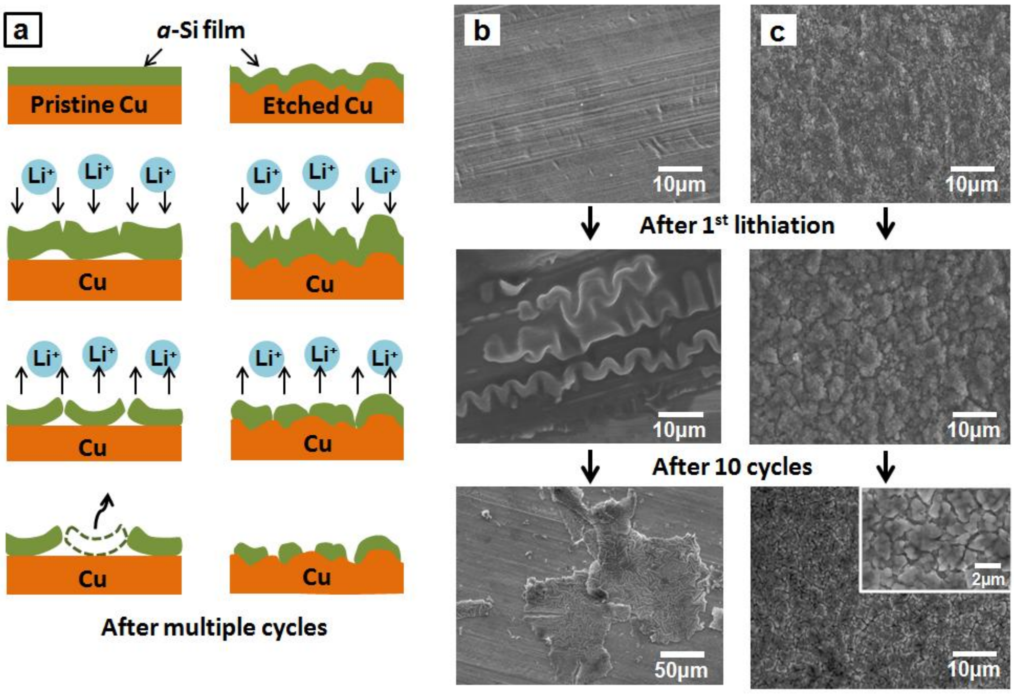

Figure 5.6 (a) A schematic diagram of degradation processes of the *a*-Si anodes. The SEM images of 250 nm evaporated *a*-Si films (b) on the pristine copper and (c) $FeCl_3$-etched copper before cycling, after 1st lithiation, and after 10 cycles.

CHAPTER 6. IN-SITU STRESS MEASUREMENTS WITH THE CRACK OBSERVATION

6.1 Introduction

The stress evolution in the *a*-Si anode was explored by an in-situ stress measurement technique as described in the previous chapter. The material failure subject to the stress induced cracking during electrochemical cycling were evaluated by the quantitative stress information. However, the detailed process of the material fracture has still remained unsolved. For instance, whether or not the material forms fracture under the compressive stress during lithiation or the tensile stress during delithiation has been an unclear issue. Moreover, the critical film thickness to avoid fracture has been widely studied by numerous literatures [46, 47, 85, 90, 141]. Those studies confirmed the existence of a critical film thickness for fracture when the thickness is below 50~200 nm.

In this chapter, the detailed process of material fracture during cycling was evaluated by the in-situ stress measurement with the crack observation using a white light interferometry. The 40 nm thick Si film was evaluated to verify the critical thickness for fracture. In addition, stress evolution depending on the potential window was discussed. The 250 nm and 500 nm thick Si film were also tested in order to clarify the thickness effect. The main focus of this work is to elucidate the relationship between the stress evolution and the fracture formation.

6.2 Experimental

For the fabrication of the cantilever, see Figure 4.4. The 40 nm, 250 nm, and 500 nm thick *a*-Si films were deposited on the cantilevers in order to investigate the stress evolution depending on the Si film thickness. Figure 6.1 shows the measurement setup for the in-situ stress measurement with the crack observation by using a WLI. The device was tested in a homemade electrochemical cell. The active material (*a*-Si) was used as a working electrode and it faced a lithium metal (as a counter and a reference electrode). Note that the *a*-Si film was placed on the top of the copper cantilever beam, so that the film cracks were able to be observed. A separator was placed between two electrodes in order to prevent a short circuit. A liquid electrolyte (1 mol $LiPF_6$ in ethylene carbonate (EC) and dimethyl carbonate (DMC) with 1:1 ratio) was filled in the cell. The WLI was used to measure the curvature of the cantilever beam during electrochemical cycles controlled by a potentiostat (Gamry G300). The white light 3D images before and after lithiation show that the beam was deformed by the compressive stress induced by the volume expansion of the *a*-Si. After electrochemical tests, the cells were disassembled and then rinsed with DMC solvent. SEM (JEOL JSM-6510LV) was used to image surface morphologies of samples before and after cycling. The acceleration voltage was 15 kV in SEM.

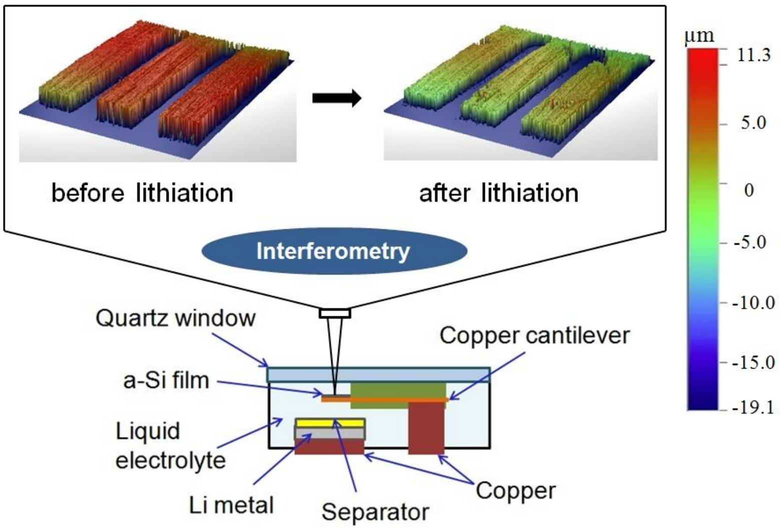

Figure 6.1 The measurement setup with the cell configuration and the 3D interferometry images before and after lithiation. Surface heights are depicted by the colors on the vertical height scale on the right side.

6.3 Results and discussion

Figure 6.2 shows the charge and discharge curve of the 40 nm *a*-Si film deposited on the pristine copper and its corresponding stress profile. The inset plot shows the cycling performance of the 40 nm thick *a*-Si upon 5 cycles. In order to investigate the stress evolution depending on the potential window, we set the cut-off voltage from 0.05 to 1 V and from 0.01 to 2 V during the first three cycles and the rest of cycles, respectively. During the first lithiation, the voltage gradually dropped until a voltage plateau appeared below 0.5 V and the magnitude of stress was relatively small, which indicates the SEI formation. Below 0.5 V, the compressive stress started to increase linearly indicating the film began to flow elastically, where the Si-Li alloy process occurred. The compressive stress reached a maximum value of -0.6 GPa when the voltage was 0.38 V. With further lithiation, silicon experienced plastic deformation in order to accommodate the additional volume expansion. The stress then gradually decreased to -0.25 GPa, which suggests that material delamination caused the stress relaxation during the lithiation process. The lithiated silicon was corresponded to $Li_{3.25}Si$ having a capacity of 3099 mAh g^{-1}. During the first delithiation, the silicon experienced tensile stress due to the volume contraction. Initially, the tensile stress increased rapidly to 0.4 GPa. With further delithiation, the stress reached 0.5 GPa, which was lower than that of the tensile yield strength of the 250 nm thick film (~1 GPa) when the cut-off voltage was set to 2 V. Note that the cut-off voltage here was 1 V. This suggests that the silicon was not fully delithiated and the volume did not return to the original state.

In the second cycle, the stress started to drop rapidly right after the end of the first delithiation. This implies that the initiated SEI formation during the first cycle was stable from the second cycle. The compressive stress began to flow plastically when the stress reached -0.25 GPa and the stress increased slightly to -0.27 GPa. The stress relaxation was not observed during the plastic deformation unlike the first cycle because the major material fracture occurred in the initial cycle and the controlled cut-off voltage (1 V) was subject to less stress induced cracking. The sequent stress profiles until the end of third cycle were similar to the previous cycle. In the inset plot, the delithiation capacity during the first three cycles were quite stable (~1700 mAh g^{-1}). With the narrow potential window (0.05-1 V), the volume changes associated with the stress induced cracking were minimized resulting in stable cyclability.

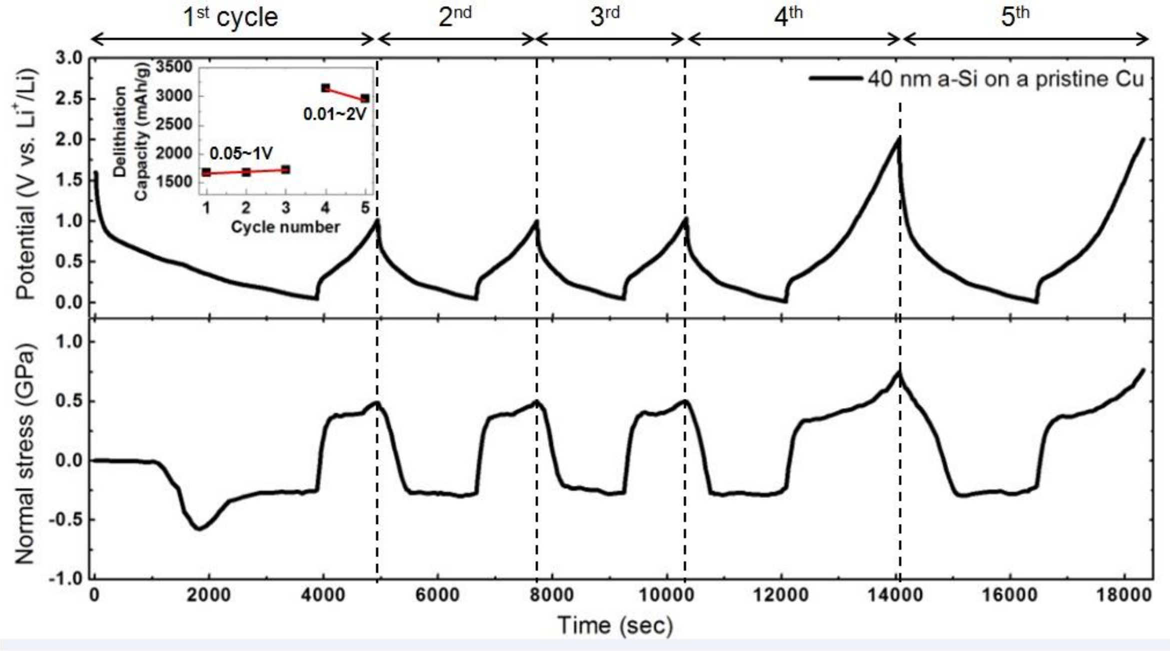

Figure 6.2 The voltage and in-situ stress profiles of a 40 nm thick *a*-Si film on a pristine Cu during 5 cycles. (inset) The cycling performance upon 5 cycles. During the initial three cycles, the potential window was set from 0.05 V to 1 V. During the rest of cycles, the potential window was set from 0.01 V to 2 V.

Upon the fourth lithiation (potential window: 0.01-2 V), the stress began to flow elastically like the previous cycle. At the end of the lithiation, the compressive stress was shown to have slight reduction from -0.29 GPa to -0.22 GPa when the voltage was below 0.05 V indicating the occurrence of additional material failure due to the promoted Si-Li alloying ($Li_{3.65}Si$) corresponding to a capacity of 3492 mAh g^{-1}. Although the fully lithiated silicon was reported to be $Li_{3.75}Si$ in the literature [122], such discrepancy might be attributed to different cycling rates and inhomogeneous structures in the interface between the film and the substrate. Upon the fourth delithiation, the tensile stress began to flow plastically when the stress reached 0.4 GPa. The stress reached a maximum value of 0.75 GPa at the end of delithiation indicating that the silicon was further delithiated when the cut-off voltage was set to 2 V compared to the first three cycles when the cut-off voltage was set to 1 V. Upon the fifth lithiation, the stress began to drop linearly and the slope was increased below 0.5 V, suggesting the breakup and the reformation of SEI due to the large tensile stress during the previous delithiation. The compressive stress reached -0.29 GPa at 0.26 V and the reduction of the stress (from -0.29 GPa to -0.22 GPa) was observed below 0.05 V. Upon the delithiation, the tensile stress was promoted to 0.76 GPa. In the inset plot in Figure 6.2, the delithiation capacity in the fourth and fifth cycles was reduced from 3143 mAh g^{-1} to 2968 mAh g^{-1}, which was attributable to the wide potential window (0.01-2 V) allowing further accommodation of volume changes resulting in the capacity fading.

With respect to stress analyses addressed by numerous papers [47, 137, 142, 143], one of the assumption was that the film is well bonded at the substrate in order to simplify the model analyses. Based on the assumption, the critical thickness of films to avoid fracture was derived as a function of the fracture toughness. The critical cracking size was expressed as [90],

$$h_c = 4\sqrt{2}\frac{G_c E}{\sigma^2(1-v^2)} \qquad (6.1)$$

where E, σ and v are Young's modulus, yield stress and Poisson's ratio, respectively. G_c is the cracking resistance which can be derived from the fracture toughness K_c divided by $E' = E$ for plain stress. Substituting the parameters with known values, the critical thickness is between

100 and 200 nm. Recently, Haftbaradaran et al. demonstrated the critical thickness for fracture could be decreased due to the nature of a slippery interface between the film and the substrate. They derived the critical cracking size as a function of the fracture toughness and the interfacial sliding strength as following [85],

$$h_{cr} = \frac{3E\tau_0\Gamma}{(1-\upsilon^2)\sigma_y^3} \qquad (6.2)$$

where τ_0 and Γ are the interfacial sliding strength and the fracture toughness, respectively. The estimated critical thickness was ca. 50 nm. In this thesis, the 40 nm thickness was chosen to avoid fracture and verify the above equation 6.2. However, in this experimental stress profile, the stress relaxation was observed during the plastic deformation, which suggests that the material fracture still exists in the 40 nm thick film. Figure 6.3 shows the SEM surface morphology of the 40 nm thick *a*-Si film after 5 cycles. Although most of films were still intact with the substrate, the silicon formed nanocracks with the size of ca. 200 nm.

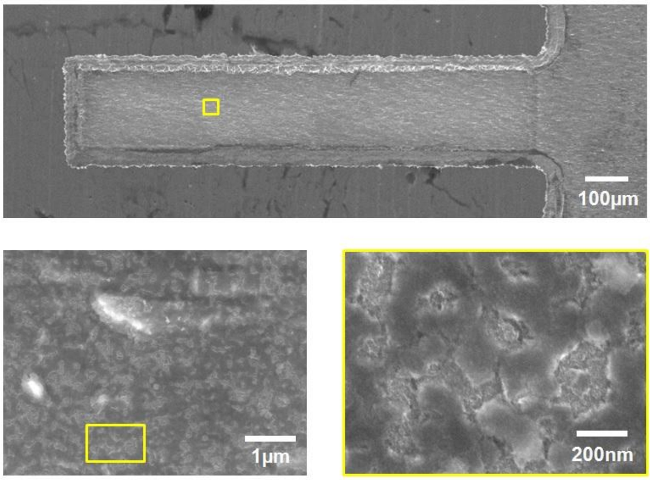

Figure 6.3 SEM images of the 40 nm thick *a*-Si film after 5 cycles.

The stress evolution with the increase in the film thickness was evaluated. Thicker silicon films are known to have larger stress induced cracking and high inherent resistance, which leads to a poor cycling performance. Figure 6.4 shows (left) the charge and discharge properties and the stress profile of the 250 nm thick *a*-Si film on the pristine copper during the first cycle, and (right) the corresponding optical images at certain state of charge and discharge. During the first lithiation, the voltage gradually dropped until a voltage plateau appeared below 0.35 V, which indicates the SEI formation. Below 0.35 V, the compressive stress began to increase linearly indicating the elastic deformation, where the Si-Li alloy process occurs. The compressive stress reached a maximum value of -0.82 GPa when the voltage was at 0.23 V, suggesting the more mass loading induced the larger yield stress compared to the 40 nm thick film (-0.6 GPa). With further lithiation, the compressive stress began to flow plastically. The stress then gradually decreased to -0.32 GPa, thus the relaxation of the compressive stress for the 250 nm thick film was 0.5 GPa. The stress relaxation was approximately twice larger than that of the 40 nm thick film, which suggests that more severe material failure results in the loss of contact, thereby relieving the stress during the lithiation process. The lithiated silicon was corresponded to $Li_{3.2}Si$ having a capacity of 3070 mAh g^{-1}.

The film delamination and fracture could be determined by the optical images from the white light interferometer. In the stress profile, position (a) was before the Si-Li alloying began and the corresponding optical image displayed the clean surface. The position (b) is where the compressive yield strength was reached. In the optical image (b), the dark surface on the cantilever beam represented the crumbled film after the silicon developed undulation caused by the volume expansion. The randomly distributed dark surface can be elucidated due to the inhomogeneous nature of the Si-Li alloying at the high cycling rate (1C). The dark surface in the position (c) became larger at the end of lithiation.

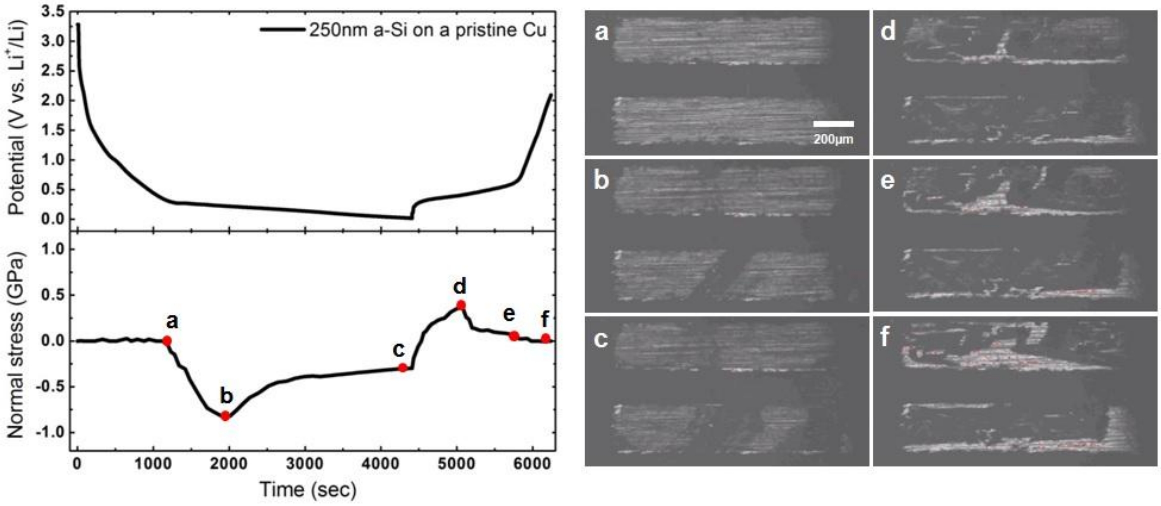

Figure 6.4 (left) Voltage and in-situ stress profiles of a 250 nm thick *a*-Si film on the pristine Cu during the first cycle. (right) Optical images corresponding to certain points (a-f) at state of charge and discharge. The potential window was set from 0.02 V to 2 V.

Upon delithiation, the silicon experienced tensile stress due to the volume contraction. Initially, the tensile stress increased rapidly to 0.4 GPa, when the voltage was 0.4 V. With further delithiation, the stress dissipation was observed, which was attributable to major film cracking in addition to plastic deformation. After the tensile stress reached near zero, the voltage began to increase steeply, which suggests that the Si islands storing Li ions lost their electrical contact, thereby losing electrons rapidly. The position (d) is where the tensile yield strength was reached. In other words, major film cracking occurred due to the promoted tensile stress induced by the volume reduction. In the optical image (d), most of the film became dark suggesting the film underwent loss of contact with the copper substrate (bright surface). At the position (e) and (f), the copper surface became larger with the shrinkage of the film during further delithiation.

The stress evolution with the 500 nm thick *a*-Si film was evaluated in the similar manner as shown in Figure 6.5. During the first lithiation, the voltage gradually dropped until a voltage plateau appeared below 0.2 V, which indicates the SEI formation. The plateau voltage was lower than the 250 nm film due to higher electrical resistance of the thick film and the longer diffusion length, which takes longer time for Li ions to react with silicon. Below 0.2 V, the compressive stress began to increase linearly indicating the elastic deformation, where the Si-Li alloy process occurs. The compressive stress reached a maximum value of -1.1 GPa when the voltage was at 0.14 V, suggesting the more mass loading induced the larger yield stress compared to the 250 nm thick film (-0.82 GPa). With further lithiation, the compressive stress began to flow plastically. The stress then gradually decreased to -0.55 GPa. The lithiated silicon was corresponded to $Li_{3.1}Si$ having a capacity of 2945 mAh g^{-1}. Lower charge capacity compared to the 250 nm thick film (3070 mAh g^{-1}) was attributable to the longer diffusion length of the thicker film leading to the limited access of Li ions at high cycling rate (1C).

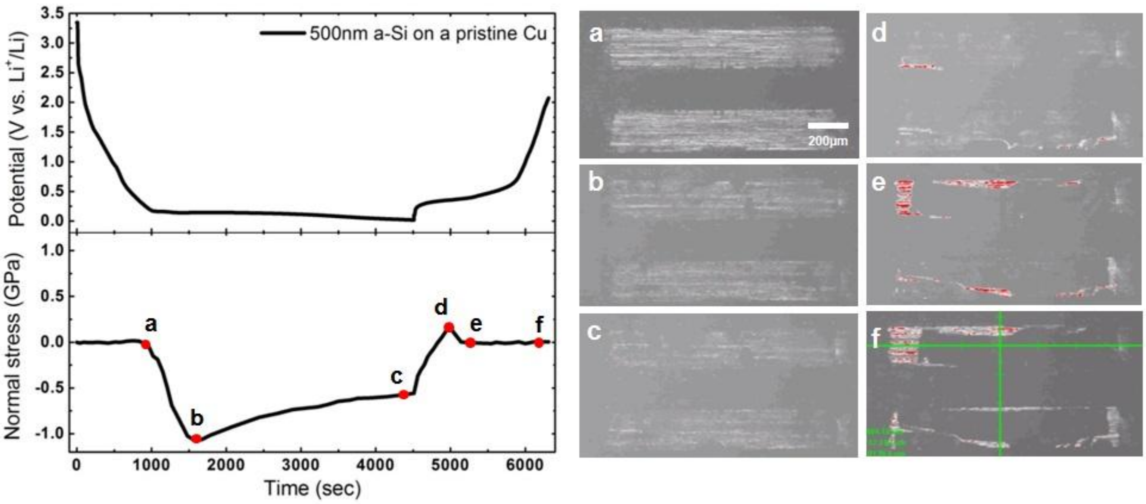

Figure 6.5 (left) Voltage and in-situ stress profiles of a 500 nm thick *a*-Si film on the pristine Cu during the first cycle. (right) Optical images corresponding to certain points (a-f) at state of charge and discharge. The potential window was set from 0.02 V to 2 V.

The optical images during lithiation were similar to the 250 nm sample. Upon delithiation, the silicon experienced tensile stress due to the volume contraction. Initially, the tensile stress increased rapidly to 0.2 GPa, when the voltage was 0.35 V. With further delithiation, the stress dissipation was observed, which was attributable to material fracture in addition to plastic deformation. The position (d) is where the tensile yield strength was reached. In the optical image (d), most of the film became dark suggesting the film underwent loss of contact with the copper substrate. At the position (e) and (f), the copper surface became larger with the further delithiation. Compared to the 250 nm thick film, the 500 nm film had larger area of cracks and specially showed severe shrinkage of the film during the volume contraction. Therefore, the interfacial sliding strength of the thicker film is expected to be smaller than the thinner film. The lower tensile yield strength of the 500 nm thick film converges to the equation 6.2 that the interfacial sliding strength is proportional to the yield stress.

CHAPTER 7. IN-SITU MONITOR ELECTROCHEMICAL PROCESSES IN BATTERIES USING VIBRATING MICROCANTILEVERS

7.1 Introduction

A lithium ion battery is an electrochemical cell in which lithium ions move from the negative electrode (anode) to the positive electrode (cathode) during discharge, and vice versa during charge. Recently, there are intense interests to develop next-generation battery materials [95, 144]. However, the main challenge is to maintain the stable electrode and electrolyte interface. For example, silicon is a promising candidate of anode materials due to its high specific capacity (4200 mAh g^{-1}). The capacity of silicon is ten folds of graphite (372 mAh g^{-1}). However, the major drawback of silicon is the huge volume expansion (~up to 400%) upon insertion and extraction of lithium ions [21, 30]. The large volume change causes significant mechanical stress, material degradation and loss of electrical contact. Solid-electrolyte interphase (SEI) layers are passivation layers formed on electrodes during the electrochemical cycles as a result of electrolyte decomposition. On the other hand, SEI layers also protect stored lithium atoms from electrolytes. The SEI formation in silicon anodes is hypothesized as an inhomogeneous and a dynamic process. Due to the fracture of silicon electrodes, SEI may break and re-grow during electrochemical cycles [41, 43]. Nevertheless, there are very limited tools to in-situ monitor the formation and degradation of SEI layers during the charge and discharge.

This thesis represents in-situ monitoring of electrochemical processes of lithium ion batteries by measuring the frequency shift of vibrating micro-cantilevers made of a bilayer structure (battery materials on copper). The electrochemical processes, including SEI formation and lithiation are quantified by monitoring the shift of resonant frequency. The mass changes of battery materials during charge and discharge cause frequency shift of cantilevers. This method provides more kinetic and dynamic information of interfaces between the electrode and electrolyte that are currently not accessible by other methods.

7.2 Experimental

Figure 7.1 shows the measurement setup for the vibration test. The device was tested in a homemade electrochemical cell. The active material (*a*-Si) was used as a working electrode and it faced a lithium metal (as a counter and a reference electrode). A separator was placed between two electrodes in order to prevent a short circuit. A liquid electrolyte (1 mol $LiPF_6$ in ethylene carbonate (EC) and dimethyl carbonate (DMC) with 1:1 ratio) was filled in the cell. A laser vibrometer (OFV534 Polytec) was used to measure the vibration of the cantilever during electrochemical cycles controlled by a potentiostat (Gamry G300).

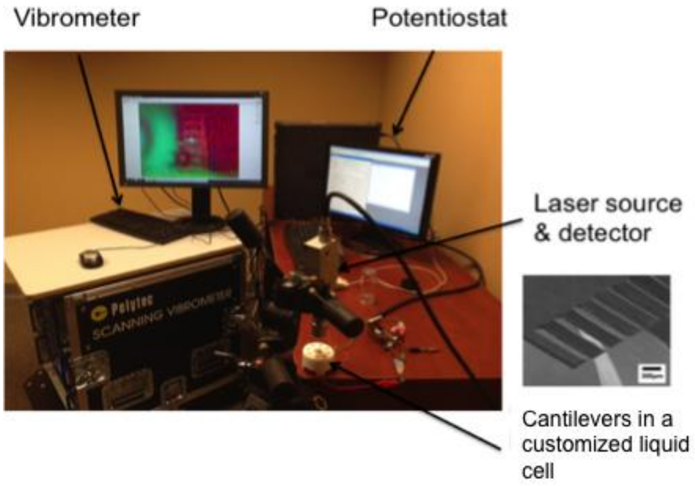

Figure 7.1 The measurement setup of the vibration test.

7.3 Design

Figure 7.2 shows the operational principle of the conventional LIBs (top) and proposed in-situ monitoring technique for the frequency shift of vibrating microcantilevers. In a commercial LIB, graphite is an anode and $LiCoO_2$ is a cathode. A separator is placed inbetween to prevent a short contact. During the charge process (Li insertion), lithium ions move from the cathode to the anode through the electrolyte. The electron flows from the cathode to the anode through an external circuit. During the discharge process (Li extraction), lithium ion moves back to the cathode and reverse reactions occur. In graphite anodes, the SEI layer is formed during the first charging (lithium insertion). A stable SEI prevents another decomposition of electrolyte, contributing to a longer cycle life.

In the bottom of Figure 7.2, a microcantilever was vibrated by piezoelectric actuator that was embedded under the cantilevers. As an approximation, Hook's law ($F=k\cdot y$) is applied to the cantilever. We assume the tip displacement is directly proportional to the force on the cantilever, and the spring constant (k) is given by $k = \frac{Ewt^3}{4l^3}$, where E is the modulus of elasticity, and l, w, t are length, width and thickness of the cantilever, respectively. The fundamental resonant frequency in the absence of dimpling can be approximated by $f_0 = \frac{1}{2\pi}\sqrt{\frac{k}{m_0}}$, where m_o is an effective suspended mass, and m_0 equals 0.24 times total mass of suspended portion of the cantilever. The additive SEI mass (Δm) can be determined by the shift of resonant frequency (Δf) using $\Delta m = -2\frac{m_0}{f_0}\Delta f$. In liquid electrolytes, the cantilever becomes heavily fluid loaded and generally exhibits overdamped responses. The quality factor (Q-factor) is introduced to account for the energy dissipation, and is defined by $Q = \frac{(\Delta f)_{FWHM}}{f_0}$, where f_0 is the resonant frequency and Δf_{FWHM} is the full width at half maximum of the resonant peak (bandwidth). Q determines the smallest frequency shift that can be measured and thus decides the minimum detectable mass shift of a resonator. The Q value in liquid is typically low. It is critical to improve Q in order to improve the mass resolution.

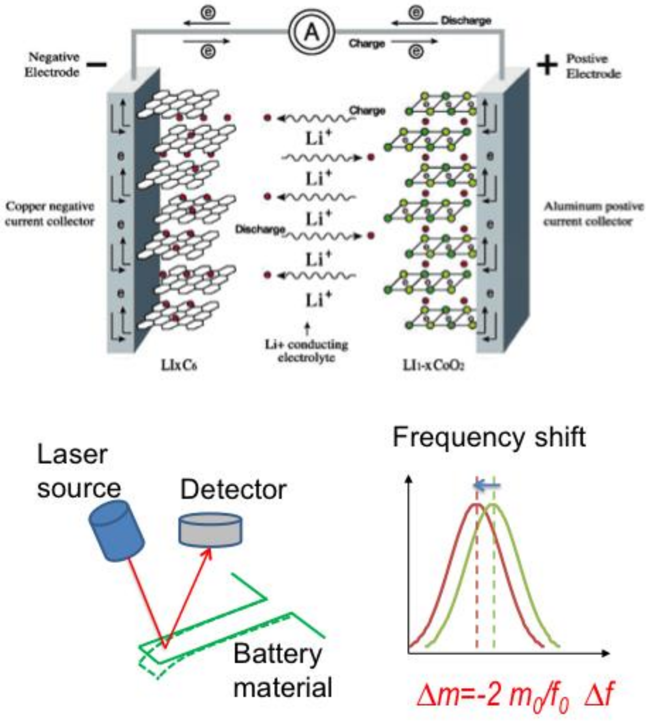

Figure 7.2 (top) Working principle of a conventional LIB (bottom) In-situ monitoring the frequency shift of vibrating microcantilevers made of battery materials on cooper.

7.4 Results and discussion

Figure 7.3 shows the frequency response of the *a*-Si anode over a wide range of frequencies (~200kHz). There were a couple of resonant frequencies. The quality factor of cantilevers in an electrolyte was less than 10. Therefore, there is a need to change the microstructures in order to get a higher Q. Figure 7.4 shows the voltage vs time for the first charging process and corresponsing frequency measurements in a half-cell configuration. We applied constant current (2 A/g) to Li metal. The voltage started from open circuit voltage and dropped to near 0 V with time. The cut-off voltage was set at 0.02 V. The vibration test scan was performed at every 200 sec. During the first lithiation, we observed that there were two distinct regions: when voltage was higher than 0.35 V and when the voltage was less than 0.35V. The voltage between 0.35-0.7 V was attributed to the SEI formation due to electrolyte decomposition. Voltage plateau at (0.02-0.3V) represents the transformation from *a* -Si to Li_xSi phase, which is associated with volume expansion.

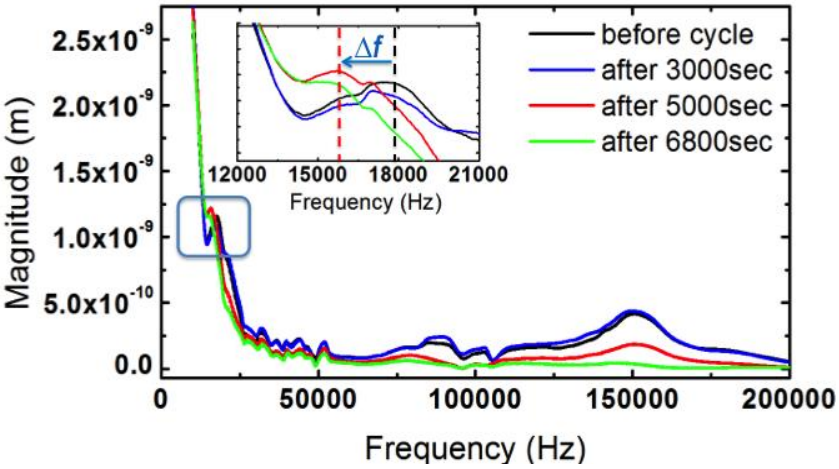

Figure 7.3 The vibration magnitude at different charge times. The first mode was 18kHz shift to 16kHz during the first charge.

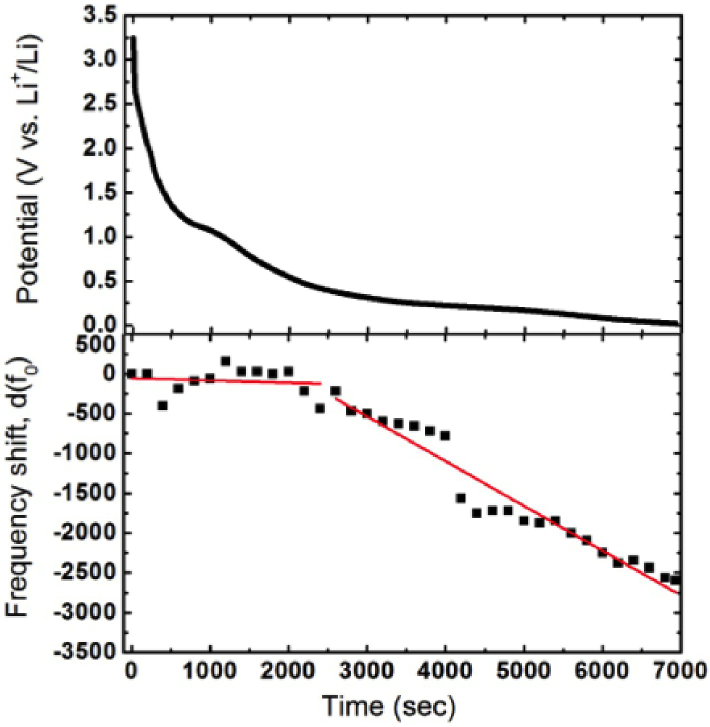

Figure 7.4 (top) The first charge curve of a silicon anode (bottom) The in-situ measurement by monitoring the frequency shift caused by the mass changes.

At a lower voltage (<0.35 V), the slope of the frequency change was much larger, indicating a different electrochemical process (Si-Li alloy formation). We also monitored the deflection of cantilevers using a white light interferometer to characterize the stress profile that was caused by Si-Li alloys [7]. The maximum stress was obtained around 230 mV, at which the electrode experienced a plastic deformation and possibly fractures and degradation. Interestingly, we observed a jump of frequency at a similar voltage using vibrating cantilevers. After the cracking of electrodes, the new Si surfaces were exposed to the electrolyte. New SEI layers were formed where additional mass changes occurred. The initial resonant frequency f_0 before cycling was found at 18,400 Hz. At the cut-off voltage (0.02 V), the frequency was shifted to 16,800 Hz due to SEI and Si-Li alloy formation. Considering the total initial mass of the cantilever (43.35 μg), we estimated that the Li ions stored in the silicon anode was approximately 7.89 μg. This in-situ study provides key information how the electrodes degrades with time upon cycling. This method provides more kinetic and dynamic information of interfaces between the electrode and electrolyte that are currently not accessible by other methods.

CHAPTER 8. CONCLUSIONS AND FUTURE SUGGESTIONS

8.1 Conclusions

In this thesis, we developed high performance negative electrodes using silicon nitride thin films. Moreover, in order to quantify the material failure mechanism, we developed a novel in-situ characterization techniques focusing on (1) the stress induced cracking, (2) mass change of SEI and lithiated *a*-Si, and (3) surface roughness effect of current collectors.

In Chapter 3, we adapted a PECVD process using SiH_4 and N_2 to deposit silicon nitride for a lithium ion battery anode. PECVD nitride deposited at low RF power exhibited a higher reversible capacity than bare *a*-Si. The incorporation of nitrogen reduced the specific capacity of the anode but dramatically improved the cyclic stability. Silicon nitride was converted into silicon with the formation of Li_3N by a conversion reaction. TEM of nitride after 300 cycles confirms that silicon nanocrystals were uniformly embedded in a conductive Li_3N matrix which prevented aggregation of the Si nanoparticles, resulting in stable cyclability. In the future, we anticipate nitride can be made into powders for lithium ion battery industry.

In Chapter 4, we presented a new in-situ monitoring approach for the mechanical stress measurement of a Si thin film anode. The electrode is a bilayer MEMS cantilever with an *a*-Si thin film thermally evaporated on the Cu substrate. The fabricated MEMS cantilever was then mounted in the customized liquid cell in order to measure the deformation using WLI system. The stress value was then derived according to our analysis model based on a Timoshenko beam theory. This work is critical to the future development of energy storage because it not only provides the guideline for optimizing electrode configurations/structures but also enables the development of a control algorithm for a battery operation in order to prevent material fractures.

In Chapter 5, we demonstrated an in-situ mechanical analysis on the surface effect of the current collectors for lithium ion battery anodes. The films were grown on the pristine and the $FeCl_3$-etched copper. The lower Coulombic efficiency of the pristine sample was due to the stress induced cracking caused by large volume changes. On the other hand, the roughened surface of the $FeCl_3$-etched sample enhanced the adhesion at the interface between the film and the copper current collector, which maintained structural stability against the volumetric increase of the *a*-Si. The capacity fading of the *a*-Si on the pristine copper was attributable to poor adhesion and severe fracture of the film caused by a promoted tensile stress (0.28 GPa) during the delithiation process, where the stress dissipated. However, the tensile stress of the *a*-Si on $FeCl_3$-etched copper was retained and further promoted to 0.4 GPa, which suggests that the film is still intact with the substrate. The stress measurements allowed quantifying the fracture energy of lithiated *a*-Si. The fracture energies of $Li_{3.0}Si$ on the pristine and roughened copper were estimated to be 4.9 J m^{-2} and 3.8 J m^{-2}, respectively, at the peak tensile stress where the film began to flow plastically.

In Chapter 6, we demonstrated in-situ stress measurements with the crack observation by using a white light interferometry. The 40 nm thick *a*-Si film was evaluated for the critical thickness to avoid fracture. Even the film with the thickness below 50 nm forms fracture with the size of 200 nm crack spacing, which the conventional study does not converge to the experimental result. The 250 nm and 500 nm thick film show the compressive yield strength of -0.82 GPa and -1.1 GPa, respectively. This suggests that larger yield stress stems from more mass loading. In the optical images where the compressive yield stress was applied, dark surface became larger representing the crumbled film after the silicon develops undulation, which was induced by the volume expansion. The maximum tensile yield strength of the 250 nm and 500 nm thick film reached 0.4 GPa and 0.2 GPa, respectively. The yield stress can be dependent on the occurrence of the fracture. In the optical images where the tensile yield stress was applied, most of the film became dark and shrank with further delithiation.

In Chapter 7, we presented a new in-situ monitoring technique to measure the mass changes of a Si thin film anode. The cantilever was actuated by a built-in piezoelectric actuator, and its resonant frequency was measured using a laser vibrometer. For the Si anode, during the SEI formation (>0.35 V), the mass change was small. At the lower voltage range (<0.35 V), the mass was significantly increased, indicating Si-Li alloying process followed by huge volume expansion. Estimated Li ions stored in the *a*-Si thin film anode during the first charging (lithiation) was approximately 7.89 μg.

8.2 Future suggestions

8.2.1 Development of silicon nitride anodes

As thin film nitride deposited by PECVD have been revealed as a promising alternative candidate for the LIB anode material, the investigation has to be made into the commercially available applications such as powder-type anodes. Although the Si-N composite thin film was shown to have a long-lasting high gravimetric capacity, it still shows lack of the volumetric capacity due to its thickness limit. In this respect, two suggestions can be made to adapt Si-N composition to the power-type anodes. First, PECVD nitride deposition can be performed onto the surface of either synthesized Si particles or carbonaceous particles. Second, prior to the material syntheses, Si or C particles can be treated by a plasma nitriding, which ionize the flown gas (N_2). A gas nitriding is another option to diffuse nitrogen into heated target material. If the chemical composition of Si and N can be controlled by those methods, the optimal nitride anodes are anticipated to serve in the LIB industries.

8.2.2 In-situ characterization technologies

In this thesis, microcantilevers were standardized for in-situ characterization techniques. Si thin films were uniformly coated on the cantilever beam. In order to adapt any other type of anode into the cantilever devices, advanced processes are required for the anode fabrication. For example, powder-type anodes such as graphite and Si particles can hardly be patterned by using a MEMS technique. A laser cutting is a conceivable option to pattern and shape such a thick film.

An in-situ cell chamber is likely imperfect design particularly when the cell is operated outside of the glove box because oxygen may result in side reaction leading to low Coulombic efficiency. Another reason is that the configuration of the in-situ cell chamber is not identical as that of the coin cell because the surface of the cantilever anode is not under the pressure unlike the coin cell. The optimal cell design is further required to improve Coulombic efficiency which enhances the accuracy of the quantified information.

From a characterization perspective, further investigations need to be developed such as thermal effects on the stress variation. The safety issue is the major concern due to the heat generated within the cell, which results in degradation and ageing problems. To the best of our knowledge, in-situ studies on the thermal effects have not been performed experimentally. In this thesis, the model analysis uses Timoshenko beam theory, which can derive the strain induced by the thermal expansion. It will be very interesting to investigate the stress evolution by selectively heating the cell using a micro-heater.

We hope in-situ characterization analyses presented in this thesis to provide guidance for better design of silicon electrodes as well as directions for future modeling of lithiated silicon. Moreover, the fracture mechanism depending on the cycling potential window and thicknesses of active material will provide guidelines to engineer the electrode material as well as cycling methods in order to minimize the material degradation. Finally, the practical uses of high capacity Si electrodes are expected to be achieved for consumers’ needs in the near future.

BIBLIOGRAPHY

[1] S. M. Lukic, J. Cao, R. C. Bansal, F. Rodriguez, and A. Emadi, "Energy storage systems for automotive applications," *Ieee Transactions on Industrial Electronics,* vol. 55, pp. 2258-2267, Jun 2008.

[2] W. Kempton and S. E. Letendre, "Electric vehicles as a new power source for electric utilities," *Transportation Research Part D-Transport and Environment,* vol. 2, pp. 157-175, Sep 1997.

[3] A. Khaligh and Z. H. Li, "Battery, Ultracapacitor, Fuel Cell, and Hybrid Energy Storage Systems for Electric, Hybrid Electric, Fuel Cell, and Plug-In Hybrid Electric Vehicles: State of the Art," *Ieee Transactions on Vehicular Technology,* vol. 59, pp. 2806-2814, Jul 2010.

[4] C. C. Chan, "The state of the art of electric and hybrid vehicles," *Proceedings of the Ieee,* vol. 90, pp. 247-275, Feb 2002.

[5] C. C. Chan, "The state of the art of electric, hybrid, and fuel cell vehicles," *Proceedings of the Ieee,* vol. 95, pp. 704-718, Apr 2007.

[6] K. C. Divya and J. Ostergaard, "Battery energy storage technology for power systems-An overview," *Electric Power Systems Research,* vol. 79, pp. 511-520, Apr 2009.

[7] B. Dunn, H. Kamath, and J. M. Tarascon, "Electrical Energy Storage for the Grid: A Battery of Choices," *Science,* vol. 334, pp. 928-935, Nov 18 2011.

[8] N. Terada, T. Yanagi, S. Arai, M. Yoshikawa, K. Ohta, N. Nakajima, A. Yanai, and N. Arai, "Development of lithium batteries for energy storage and EV applications," *Journal of Power Sources,* vol. 100, pp. 80-92, Nov 30 2001.

[9] G. Pancaldi, "Electricity and Life - Volta Path to the Battery," *Historical Studies in the Physical and Biological Sciences,* vol. 21, pp. 123-160, 1990.

[10] M. R. Palacin, "Recent advances in rechargeable battery materials: a chemist's perspective," *Chemical Society Reviews,* vol. 38, pp. 2565-2575, 2009.

[11] M. Durr, A. Cruden, S. Gair, and J. R. McDonald, "Dynamic model of a lead acid battery for use in a domestic fuel cell system," *Journal of Power Sources,* vol. 161, pp. 1400-1411, Oct 27 2006.

[12] E. Karden, S. Ploumen, B. Fricke, T. Miller, and K. Snyder, "Energy storage devices for future hybrid electric vehicles," *Journal of Power Sources,* vol. 168, pp. 2-11, May 25 2007.

[13] M. A. Fetcenko, S. R. Ovshinsky, B. Reichman, K. Young, C. Fierro, J. Koch, A. Zallen, W. Mays, and T. Ouchi, "Recent advances in NiMH battery technology," *Journal of Power Sources,* vol. 165, pp. 544-551, Mar 20 2007.

[14] J. M. Tarascon and M. Armand, "Issues and challenges facing rechargeable lithium batteries," *Nature,* vol. 414, pp. 359-367, Nov 15 2001.

[15] J. B. Goodenough and Y. Kim, "Challenges for Rechargeable Li Batteries," *Chemistry of Materials,* vol. 22, pp. 587-603, 2010.

[16] G. Girishkumar, B. McCloskey, A. C. Luntz, S. Swanson, and W. Wilcke, "Lithium - Air Battery: Promise and Challenges," *Journal of Physical Chemistry Letters,* vol. 1, pp. 2193-2203, Jul 15 2010.

[17] S. E. Cheon, K. S. Ko, J. H. Cho, S. W. Kim, E. Y. Chin, and H. T. Kim, "Rechargeable lithium sulfur battery - I. Structural change of sulfur cathode during discharge and charge," *Journal of the Electrochemical Society,* vol. 150, pp. A796-A799, Jun 2003.

[18] S. S. Zhang, "Liquid electrolyte lithium/sulfur battery: Fundamental chemistry, problems, and solutions," *Journal of Power Sources,* vol. 231, pp. 153-162, Jun 1

2013.

[19] D. Aurbach, Y. Talyosef, B. Markovsky, E. Markevich, E. Zinigrad, L. Asraf, J. S. Gnanaraj, and H. J. Kim, "Design of electrolyte solutions for Li and Li-ion batteries: a review," *Electrochimica Acta,* vol. 50, pp. 247-254, Nov 30 2004.

[20] L. Yang and B. L. Lucht, "Inhibition of Electrolyte Oxidation in Lithium Ion Batteries with Electrolyte Additives," *Electrochemical and Solid State Letters,* vol. 12, pp. A229-A231, 2009.

[21] R. Teki, M. K. Datta, R. Krishnan, T. C. Parker, T. M. Lu, P. N. Kumta, and N. Koratkar, "Nanostructured Silicon Anodes for Lithium Ion Rechargeable Batteries," *Small,* vol. 5, pp. 2236-2242, 2009.

[22] M. Winter, J. O. Besenhard, M. E. Spahr, and P. Novak, "Insertion electrode materials for rechargeable lithium batteries," *Advanced Materials,* vol. 10, pp. 725-763, Jul 9 1998.

[23] D. Aurbach, B. Markovsky, I. Weissman, E. Levi, and Y. Ein-Eli, "On the correlation between surface chemistry and performance of graphite negative electrodes for Li ion batteries," *Electrochimica Acta,* vol. 45, pp. 67-86, 1999 1999.

[24] S. Flandrois and B. Simon, "Carbon materials for lithium-ion rechargeable batteries," *Carbon,* vol. 37, pp. 165-180, 1999 1999.

[25] E. Peled, C. Menachem, D. BarTow, and A. Melman, "Improved graphite anode for lithium-ion batteries - Chemically bonded solid electrolyte interface and nanochannel formation," *Journal of the Electrochemical Society,* vol. 143, pp. L4-L7, Jan 1996.

[26] M. S. Whittingham, "Lithium batteries and cathode materials," *Chemical Reviews,* vol. 104, pp. 4271-4301, Oct 2004.

[27] H. Maleki, G. P. Deng, A. Anani, and J. Howard, "Thermal stability studies of Li-ion

cells and components," *Journal of the Electrochemical Society,* vol. 146, pp. 3224-3229, Sep 1999.

[28] M. Armand and J. M. Tarascon, "Building better batteries," *Nature,* vol. 451, pp. 652-657, Feb 7 2008.

[29] B. Scrosati, "Battery Technology - Challenge of Portable Power," *Nature,* vol. 373, pp. 557-558, Feb 16 1995.

[30] A. Magasinski, P. Dixon, B. Hertzberg, A. Kvit, J. Ayala, and G. Yushin, "High-performance lithium-ion anodes using a hierarchical bottom-up approach," *Nature Materials,* vol. 9, pp. 353-358, 2010.

[31] J. Wang, H. L. Zhao, J. C. He, and C. M. Wang, "Nano-sized SiOx/C composite anode for lithium ion batteries," *Journal of Power Sources,* vol. 196, pp. 4811-4815, 2011.

[32] S. Xun, X. Song, M. E. Grass, D. K. Roseguo, Z. Liu, V. S. Battaglia, and G. Liu, "Improved Initial Performance of Si Nanoparticles by Surface Oxide Reduction for Lithium-Ion Battery Application," *Electrochemical and Solid State Letters,* vol. 14, pp. A61-A63, 2011 2011.

[33] R. G. Lv, J. Yang, J. L. Wang, and Y. N. NuLi, "Electrodeposited porous-microspheres Li-Si films as negative electrodes in lithium-ion batteries," *Journal of Power Sources,* vol. 196, pp. 3868-3873, 2011.

[34] J. Y. Eom and H. S. Kwon, "Preparation of Single-Walled Carbon Nanotube/Silicon Composites and Their Lithium Storage Properties," *Acs Applied Materials & Interfaces,* vol. 3, pp. 1015-1021, 2011.

[35] A. L. M. Reddy, M. M. Shaijumon, S. R. Gowda, and P. M. Ajayan, "Coaxial MnO2/Carbon Nanotube Array Electrodes for High-Performance Lithium Batteries," *Nano Letters,* vol. 9, pp. 1002-1006, 2009.

[36] Z. Edfouf, F. Cuevas, M. Latroche, C. Georges, C. Jordy, T. Hezeque, G. Caillon, J. C. Jumas, and M. T. Sougrati, "Nanostructured Si/Sn-Ni/C composite as negative electrode for Li-ion batteries," *Journal of Power Sources,* vol. 196, pp. 4762-4768, 2011.

[37] F. Q. Yang, "Criterion for insertion-induced microcracking and debonding of thin films," *Journal of Power Sources,* vol. 196, pp. 465-469, Jan 1 2011.

[38] T. D. Hatchard and J. R. Dahn, "In situ XRD and electrochemical study of the reaction of lithium with amorphous silicon," *Journal of the Electrochemical Society,* vol. 151, pp. A838-A842, 2004.

[39] W. J. Zhang, "A review of the electrochemical performance of alloy anodes for lithium-ion batteries," *Journal of Power Sources,* vol. 196, pp. 13-24, Jan 1 2011.

[40] P. Verma, P. Maire, and P. Novak, "A review of the features and analyses of the solid electrolyte interphase in Li-ion batteries," *Electrochimica Acta,* vol. 55, pp. 6332-6341, Sep 1 2010.

[41] J. R. Szczech and S. Jin, "Nanostructured silicon for high capacity lithium battery anodes," *Energy & Environmental Science,* vol. 4, pp. 56-72, 2011.

[42] C. K. Chan, H. Peng, G. Liu, K. McIlwrath, X. F. Zhang, R. A. Huggins, and Y. Cui, "High-performance lithium battery anodes using silicon nanowires," *Nature Nanotechnology,* vol. 3, pp. 31-35, Jan 2008.

[43] L. B. Chen, J. Y. Xie, H. C. Yu, and T. H. Wang, "An amorphous Si thin film anode with high capacity and long cycling life for lithium ion batteries," *Journal of Applied Electrochemistry,* vol. 39, pp. 1157-1162, Aug 2009.

[44] A. S. Arico, P. Bruce, B. Scrosati, J. M. Tarascon, and W. Van Schalkwijk, "Nanostructured materials for advanced energy conversion and storage devices,"

Nature Materials, vol. 4, pp. 366-377, May 2005.

[45] W. Wang and P. N. Kumta, "Nanostructured Hybrid Silicon/Carbon Nanotube Heterostructures: Reversible High-Capacity Lithium-Ion Anodes," *Acs Nano,* vol. 4, pp. 2233-2241, 2010.

[46] X. Xiao, P. Liu, M. W. Verbrugge, H. Haftbaradaran, and H. Gao, "Improved cycling stability of silicon thin film electrodes through patterning for high energy density lithium batteries," *Journal of Power Sources,* vol. 196, pp. 1409-1416, Feb 1 2011.

[47] J. Graetz, C. C. Ahn, R. Yazami, and B. Fultz, "Highly reversible lithium storage in nanostructured silicon," *Electrochemical and Solid State Letters,* vol. 6, pp. A194-A197, Sep 2003.

[48] L. Y. Beaulieu, K. W. Eberman, R. L. Turner, L. J. Krause, and J. R. Dahn, "Colossal reversible volume changes in lithium alloys," *Electrochemical and Solid State Letters,* vol. 4, pp. A137-A140, Sep 2001.

[49] J. H. Ryu, J. W. Kim, Y. E. Sung, and S. M. Oh, "Failure modes of silicon powder negative electrode in lithium secondary batteries," *Electrochemical and Solid State Letters,* vol. 7, pp. A306-A309, 2004.

[50] U. Kasavajjula, C. S. Wang, and A. J. Appleby, "Nano- and bulk-silicon-based insertion anodes for lithium-ion secondary cells," *Journal of Power Sources,* vol. 163, pp. 1003-1039, Jan 1 2007.

[51] V. Baranchugov, E. Markevich, E. Pollak, G. Salitra, and D. Aurbach, "Amorphous silicon thin films as a high capacity anodes for Li-ion batteries in ionic liquid electrolytes," *Electrochemistry Communications,* vol. 9, pp. 796-800, Apr 2007.

[52] J. P. Maranchi, A. F. Hepp, A. G. Evans, N. T. Nuhfer, and P. N. Kumta, "Interfacial properties of the a-Si/Cu : active-inactive thin-film anode system for lithium-ion

batteries," *Journal of the Electrochemical Society,* vol. 153, pp. A1246-A1253, 2006.

[53] S. Ohara, J. Suzuki, K. Sekine, and T. Takamura, "A thin film silicon anode for Li-ion batteries having a very large specific capacity and long cycle life," *Journal of Power Sources,* vol. 136, pp. 303-306, 2004.

[54] G. X. Wang, J. H. Ahn, J. Yao, S. Bewlay, and H. K. Liu, "Nanostructured Si-C composite anodes for lithium-ion batteries," *Electrochemistry Communications,* vol. 6, pp. 689-692, Jul 2004.

[55] A. A. Arie, O. M. Vovk, and J. K. Lee, "Surface-Coated Silicon Anodes with Amorphous Carbon Film Prepared by Fullerene C-60 Sputtering," *Journal of the Electrochemical Society,* vol. 157, pp. A660-A665, 2010.

[56] H. F. Xiang, K. Zhang, G. Ji, J. Y. Lee, C. J. Zou, X. D. Chen, and J. S. Wu, "Graphene/nanosized silicon composites for lithium battery anodes with improved cycling stability," *Carbon,* vol. 49, pp. 1787-1796, 2011.

[57] S. L. Chou, J. Z. Wang, M. Choucair, H. K. Liu, J. A. Stride, and S. X. Dou, "Enhanced reversible lithium storage in a nanosize silicon/graphene composite," *Electrochemistry Communications,* vol. 12, pp. 303-306, Feb 2010.

[58] S. W. Song, K. A. Striebel, R. P. Reade, G. A. Roberts, and E. J. Cairns, "Electrochemical studies of nanoncrystalline Mg2Si thin film electrodes prepared by pulsed laser deposition," *Journal of the Electrochemical Society,* vol. 150, pp. A121-A127, Jan 2003.

[59] I. Kim, P. N. Kumta, and G. E. Blomgren, "Si/TiN nanocomposites - Novel anode materials for Li-ion batteries," *Electrochemical and Solid State Letters,* vol. 3, pp. 493-496, Nov 2000.

[60] Y. He, X. Q. Yu, Y. H. Wang, H. Li, and X. J. Huang, "Alumina-Coated Patterned

Amorphous Silicon as the Anode for a Lithium-Ion Battery with High Coulombic Efficiency," *Advanced Materials,* vol. 23, pp. 4938-4941, Nov 9 2011.

[61] J. P. Maranchi, A. F. Hepp, and P. N. Kumta, "High capacity, reversible silicon thin-film anodes for lithium-ion batteries," *Electrochemical and Solid State Letters,* vol. 6, pp. A198-A201, Sep 2003.

[62] S. Huang and T. Zhu, "Atomistic mechanisms of lithium insertion in amorphous silicon," *Journal of Power Sources,* vol. 196, pp. 3664-3668, 2011.

[63] T. Zhang, L. J. Fu, H. Takeuchi, J. Suzuki, K. Sekine, T. Takamura, and Y. P. Wu, "Studies of the structure of vacuum deposited silicon films on metal substrates as anode materials for Li-ion batteries," *Journal of Power Sources,* vol. 159, pp. 349-352, 2006.

[64] C. K. Chan, R. Ruffo, S. S. Hong, and Y. Cui, "Surface chemistry and morphology of the solid electrolyte interphase on silicon nanowire lithium-ion battery anodes," *Journal of Power Sources,* vol. 189, pp. 1132-1140, 2009.

[65] M. T. McDowell, S. W. Lee, I. Ryu, H. Wu, W. D. Nix, J. W. Choi, and Y. Cui, "Novel Size and Surface Oxide Effects in Silicon Nanowires as Lithium Battery Anodes," *Nano Letters,* vol. 11, pp. 4018-4025, Sep 2011.

[66] X. L. Chen, K. Gerasopoulos, J. C. Guo, A. Brown, C. S. Wang, R. Ghodssi, and J. N. Culver, "Virus-Enabled Silicon Anode for Lithium-Ion Batteries," *Acs Nano,* vol. 4, pp. 5366-5372, Sep 2010.

[67] L. F. Cui, R. Ruffo, C. K. Chan, H. L. Peng, and Y. Cui, "Crystalline-Amorphous Core-Shell Silicon Nanowires for High Capacity and High Current Battery Electrodes," *Nano Letters,* vol. 9, pp. 491-495, Jan 2009.

[68] N. Dimov, S. Kugino, and M. Yoshio, "Carbon-coated silicon as anode material for

lithium ion batteries: advantages and limitations," *Electrochimica Acta,* vol. 48, pp. 1579-1587, May 15 2003.

[69] L. W. Ji and X. W. Zhang, "Evaluation of Si/carbon composite nanofiber-based insertion anodes for new-generation rechargeable lithium-ion batteries," *Energy & Environmental Science,* vol. 3, pp. 124-129, 2010.

[70] P. C. Chen, J. Xu, H. T. Chen, and C. W. Zhou, "Hybrid silicon-carbon nanostructured composites as superior anodes for lithium ion batteries," *Nano Research,* vol. 4, pp. 290-296, 2011.

[71] X. L. Yang, Z. Y. Wen, X. J. Zhu, and S. H. Huang, "Preparation and electrochemical properties of silicon/carbon composite electrodes," *Electrochemical and Solid State Letters,* vol. 8, pp. A481-A483, 2005.

[72] S. H. Ng, J. Z. Wang, D. Wexler, K. Konstantinov, Z. P. Guo, and H. K. Liu, "Highly reversible lithium storage in spheroidal carbon-coated silicon nanocomposites as anodes for lithium-ion batteries," *Angewandte Chemie-International Edition,* vol. 45, pp. 6896-6899, 2006.

[73] A. A. Arie, J. O. Song, and J. K. Lee, "Structural and electrochemical properties of fullerene-coated silicon thin film as anode materials for lithium secondary batteries," *Materials Chemistry and Physics,* vol. 113, pp. 249-254, 2009.

[74] W. Wang, R. Epur, and P. N. Kumta, "Vertically aligned silicon/carbon nanotube (VASCNT) arrays: Hierarchical anodes for lithium-ion battery," *Electrochemistry Communications,* vol. 13, pp. 429-432, 2011.

[75] J. C. Guo, A. Sun, X. L. Chen, C. S. Wang, and A. Manivannan, "Cyclability study of silicon-carbon composite anodes for lithium-ion batteries using electrochemical impedance spectroscopy," *Electrochimica Acta,* vol. 56, pp. 3981-3987, 2011.

[76] J. H. Kim, H. J. Sohn, H. Kim, G. Jeong, and W. Choi, "Enhanced cycle performance of SiO-C composite anode for lithium-ion batteries," *Journal of Power Sources,* vol. 170, pp. 456-459, Jul 10 2007.

[77] P. J. Zuo, W. G. Yang, X. Q. Cheng, and G. P. Yin, "Enhancement of the electrochemical performance of silicon/carbon composite material for lithium ion batteries," *Ionics,* vol. 17, pp. 87-90, 2011.

[78] A. Veluchamy, C.-H. Doh, D.-H. Kim, J.-H. Lee, D.-J. Lee, Y.-H. Ha, H.-M. Shin, B.-S. Jin, H.-S. Kim, S.-I. Moon, and C.-W. Park, "Improvement of cycle behaviour of SiO/C anode composite by thermochemically generated Li(4)SiO(4) inert phase for lithium batteries," *Journal of Power Sources,* vol. 188, pp. 574-577, Mar 15 2009.

[79] M. Uehara, J. Suzuki, K. Tamura, K. Sekine, and T. Takamura, "Thick vacuum deposited silicon films suitable for the anode of Li-ion battery," *Journal of Power Sources,* vol. 146, pp. 441-444, 2005.

[80] T. Takamura, S. Ohara, M. Uehara, J. Suzuki, and K. Sekine, "A vacuum deposited Si film having a Li extraction capacity over 2000 mAh/g with a long cycle life," *Journal of Power Sources,* vol. 129, pp. 96-100, Apr 15 2004.

[81] S. Bourderau, T. Brousse, and D. M. Schleich, "Amorphous silicon as a possible anode material for Li-ion batteries," *Journal of Power Sources,* vol. 81, pp. 233-236, Sep 1999.

[82] H. J. Jung, M. Park, Y. G. Yoon, G. B. Kim, and S. K. Joo, "Amorphous silicon anode for lithium-ion rechargeable batteries," *Journal of Power Sources,* vol. 115, pp. 346-351, Apr 10 2003.

[83] M. Miyachi, H. Yamamoto, H. Kawai, T. Ohta, and M. Shirakata, "Analysis of SiO anodes for lithium-ion batteries," *Journal of the Electrochemical Society,* vol. 152, pp.

A2089-A2091, 2005.

[84] H. Takezawa, K. Iwamoto, S. Ito, and H. Yoshizawa, "Electrochemical behaviors of nonstoichiometric silicon suboxides (SiOx) film prepared by reactive evaporation for lithium rechargeable batteries," *Journal of Power Sources*, vol. 244, pp. 149-157, Dec 15 2013.

[85] S. P. V. Nadimpalli, V. A. Sethuraman, G. Bucci, V. Srinivasan, A. F. Bower, and P. R. Guduru, "On Plastic Deformation and Fracture in Si Films during Electrochemical Lithiation/Delithiation Cycling," *Journal of the Electrochemical Society*, vol. 160, pp. A1885-A1893, 2013.

[86] T. L. Kulova, A. M. Skundin, Y. V. Pleskov, E. I. Terukov, and O. I. Kon'kov, "Lithium insertion into amorphous silicon thin-film electrodes," *Journal of Electroanalytical Chemistry*, vol. 600, pp. 217-225, Feb 2007.

[87] J. J. Nguyen, K. Evanoff, and W. J. Ready, "Amorphous and nanocrystalline silicon growth on carbon nanotube substrates," *Thin Solid Films*, vol. 519, pp. 4144-4147, Apr 2011.

[88] M. W. Forney, R. A. DiLeo, A. Raisanen, M. J. Ganter, J. W. Staub, R. E. Rogers, R. D. Ridgley, and B. J. Landi, "High performance silicon free-standing anodes fabricated by low-pressure and plasma-enhanced chemical vapor deposition onto carbon nanotube electrodes," *Journal of Power Sources*, vol. 228, pp. 270-280, Apr 2013.

[89] S. O. Kim, H. T. Shim, and J. K. Lee, "Electrochemical performance of silicon thin film anodes covered by diamond-like carbon with various surface coating morphologies," *Journal of Solid State Electrochemistry*, vol. 14, pp. 1247-1253, Jul 2010.

[90] J. C. Li, A. K. Dozier, Y. C. Li, F. Q. Yang, and Y. T. Cheng, "Crack Pattern Formation in Thin Film Lithium-Ion Battery Electrodes," *Journal of the Electrochemical Society,* vol. 158, pp. A689-A694, 2011.

[91] Y. He, X. Q. Yu, G. Li, R. Wang, H. Li, Y. L. Wang, H. J. Gao, and X. J. Huang, "Shape evolution of patterned amorphous and polycrystalline silicon microarray thin film electrodes caused by lithium insertion and extraction," *Journal of Power Sources,* vol. 216, pp. 131-138, Oct 15 2012.

[92] V. A. Sethuraman, M. J. Chon, M. Shimshak, V. Srinivasan, and P. R. Guduru, "In situ measurements of stress evolution in silicon thin films during electrochemical lithiation and delithiation," *Journal of Power Sources,* vol. 195, pp. 5062-5066, Aug 1 2010.

[93] A. M. Wilson and J. R. Dahn, "LITHIUM INSERTION IN CARBONS CONTAINING NANODISPERSED SILICON," *Journal of the Electrochemical Society,* vol. 142, pp. 326-332, Feb 1995.

[94] K. Hanai, Y. Liu, N. Imanishi, A. Hirano, M. Matsumura, T. Ichikawa, and Y. Takeda, "Electrochemical studies of the Si-based composites with large capacity and good cycling stability as anode materials for rechargeable lithium ion batteries," *Journal of Power Sources,* vol. 146, pp. 156-160, Aug 2005.

[95] J. Yang, Y. Takeda, N. Imanishi, C. Capiglia, J. Y. Xie, and O. Yamamoto, "SiOx-based anodes for secondary lithium batteries," *Solid State Ionics*, vol. 152, pp. 125-129, Dec 2002.

[96] D. Ahn, C. Kim, J. G. Lee, and B. Park, "The effect of nitrogen on the cycling performance in thin-film Si1-xNx anode," *Journal of Solid State Chemistry,* vol. 181, pp. 2139-2142, Sep 2008.

[97] H. Huang, K. J. Winchester, A. Suvorova, B. R. Lawn, Y. Liu, X. Z. Hu, J. M. Dell, and L. Faraone, "Effect of deposition conditions on mechanical properties of low-temperature PECVD silicon nitride films," *Materials Science and Engineering a-Structural Materials Properties Microstructure and Processing,* vol. 435, pp. 453-459, Nov 5 2006.

[98] J. Z. Wang, C. Zhong, S. L. Chou, and H. K. Liu, "Flexible free-standing graphene-silicon composite film for lithium-ion batteries," *Electrochemistry Communications,* vol. 12, pp. 1467-1470, Nov 2010.

[99] J. K. Lee, K. B. Smith, C. M. Hayner, and H. H. Kung, "Silicon nanoparticles-graphene paper composites for Li ion battery anodes," *Chemical Communications,* vol. 46, pp. 2025-2027, 2010.

[100] S. K. Sharma, S. Barthwal, V. Singh, A. Kumar, P. K. Dwivedi, B. Prasad, and D. Kumar, "PECVD based silicon oxynitride thin films for nano photonic on chip interconnects applications," *Micron,* vol. 44, pp. 339-346, Jan 2013.

[101] U. V. Alpen, A. Rabenau, and G. H. Talat, "Ionic-Conductivity in Li3n Single-Crystals," *Applied Physics Letters,* vol. 30, pp. 621-623, 1977.

[102] W. Li, G. T. Wu, C. M. Araujo, R. H. Scheicher, A. Blomqvist, R. Ahuja, Z. T. Xiong, Y. P. Feng, and P. Chen, "Li+ ion conductivity and diffusion mechanism in alpha-Li3N and beta-Li3N," *Energy & Environmental Science,* vol. 3, pp. 1524-1530, 2010.

[103] W. L. Fang, H. C. Tsai, and C. Y. Lo, "Determining thermal expansion coefficients of thin films using micromachined cantilevers," *Sensors and Actuators a-Physical,* vol. 77, pp. 21-27, Sep 28 1999.

[104] J. Cho, "Porous Si anode materials for lithium rechargeable batteries," *Journal of Materials Chemistry,* vol. 20, pp. 4009-4014, 2010.

[105] M. Yoshio, T. Tsumura, and N. Dimov, "Electrochemical behaviors of silicon based anode material," *Journal of Power Sources,* vol. 146, pp. 10-14, Aug 26 2005.

[106] S. D. Beattie, D. Larcher, M. Morcrette, B. Simon, and J. M. Tarascon, "Si electrodes for li-ion batteries - A new way to look at an old problem," *Journal of the Electrochemical Society,* vol. 155, pp. A158-A163, 2008.

[107] V. A. Sethuraman, M. J. Chon, M. Shimshak, N. Van Winkle, and P. R. Guduru, "In situ measurement of biaxial modulus of Si anode for Li-ion batteries," *Electrochemistry Communications,* vol. 12, pp. 1614-1617, Nov 2010.

[108] S. J. Lee, J. K. Lee, S. H. Chung, H. Y. Lee, S. M. Lee, and H. K. Baik, "Stress effect on cycle properties of the silicon thin-film anode," *Journal of Power Sources,* vol. 97-8, pp. 191-193, Jul 2001.

[109] F. Decker, R. Pileggi, S. Passerini, and B. Scrosati, "A Comparison of the Electrochromic Behavior and the Mechanical-Properties of Wo3 and Niox Thin-Film Electrodes," *Journal of the Electrochemical Society,* vol. 138, pp. 3182-3186, Nov 1991.

[110] S. I. Pyun, K. H. Kim, and J. N. Han, "Analysis of stresses generated during hydrogen extraction from and injection into Ni(OH)(2)/NiOOH film electrode," *Journal of Power Sources,* vol. 91, pp. 92-98, Dec 2000.

[111] M. J. Chon, V. A. Sethuraman, A. McCormick, V. Srinivasan, and P. R. Guduru, "Real-Time Measurement of Stress and Damage Evolution during Initial Lithiation of Crystalline Silicon," *Physical Review Letters,* vol. 107, Jul 21 2011.

[112] S. K. Soni, B. W. Sheldon, X. Xiao, M. W. Verbrugge, D. Ahn, H. Haftbaradaran, and H. Gao, "Stress Mitigation during the Lithiation of Patterned Amorphous Si Islands," *Journal of the Electrochemical Society,* vol. 159, pp. A38-A43, 2012.

[113] H. Li, B. W. Sheldon, A. Kothari, Z. G. Ban, and B. L. Walden, "Stress evolution in nanocrystalline diamond films produced by chemical vapor deposition," *Journal of Applied Physics,* vol. 100, Nov 1 2006.

[114] J. W. Shin and E. Chason, "Compressive Stress Generation in Sn Thin Films and the Role of Grain Boundary Diffusion," *Physical Review Letters,* vol. 103, Jul 31 2009.

[115] V. A. Sethuraman, N. Van Winkle, D. P. Abraham, A. F. Bower, and P. R. Guduru, "Real-time stress measurements in lithium-ion battery negative-electrodes," *Journal of Power Sources,* vol. 206, pp. 334-342, May 15 2012.

[116] B. Bowe and V. Toal, "White light interferometric surface profiler," *Optical Engineering,* vol. 37, pp. 1796-1799, Jun 1998.

[117] C. O'Mahony, M. Hill, M. Brunet, R. Duane, and A. Mathewson, "Characterization of micromechanical structures using white-light interferometry," *Measurement Science & Technology,* vol. 14, pp. 1807-1814, Oct 2003.

[118] J. Reed, J. Schmit, S. Han, P. Wilkinson, and J. K. Gimzewski, "Interferometric profiling of microcantilevers in liquid," *Optics and Lasers in Engineering,* vol. 47, pp. 217-222, Feb 2009.

[119] D. Y. W. Yu and F. Spaepen, "The yield strength of thin copper films on Kapton," *Journal of Applied Physics,* vol. 95, pp. 2991-2997, Mar 15 2004.

[120] V. B. Shenoy, P. Johari, and Y. Qi, "Elastic softening of amorphous and crystalline Li-Si Phases with increasing Li concentration: A first-principles study," *Journal of Power Sources,* vol. 195, pp. 6825-6830, Oct 1 2010.

[121] S. Timoshenko, "Analysis of bi-metal thermostats," *Journal of the Optical Society of America and Review of Scientific Instruments,* vol. 11, pp. 233-255, Sep 1925.

[122] M. N. Obrovac and L. Christensen, "Structural changes in silicon anodes during

lithium insertion/extraction," *Electrochemical and Solid State Letters*, vol. 7, pp. A93-A96, 2004.

[123] M. N. Obrovac and L. J. Krause, "Reversible cycling of crystalline silicon powder," *Journal of the Electrochemical Society,* vol. 154, pp. A103-A108, 2007.

[124] Y. L. Kim, Y. K. Sun, and S. M. Lee, "Enhanced electrochemical performance of silicon-based anode material by using current collector with modified surface morphology," *Electrochimica Acta,* vol. 53, pp. 4500-4504, May 20 2008.

[125] J. T. Yin, M. Wada, K. Yamamoto, Y. Kitano, S. Tanase, and T. Sakai, "Micrometer-scale amorphous Si thin-film electrodes fabricated by electron-beam deposition for Li-ion batteries," *Journal of the Electrochemical Society,* vol. 153, pp. A472-A477, 2006.

[126] C. M. Hwang, C. H. Lim, J. H. Yang, and J. W. Park, "Electrochemical properties of negative SiMox electrodes deposited on a roughened substrate for rechargeable lithium batteries," *Journal of Power Sources,* vol. 194, pp. 1061-1067, Dec 1 2009.

[127] D. Reyter, S. Rousselot, D. Mazouzi, M. Gauthier, P. Moreau, B. Lestriez, D. Guyomard, and L. Roue, "An electrochemically roughened Cu current collector for Si-based electrode in Li-ion batteries," *Journal of Power Sources,* vol. 239, pp. 308-314, Oct 1 2013.

[128] C. C. Nguyen and S. W. Song, "Interfacial structural stabilization on amorphous silicon anode for improved cycling performance in lithium-ion batteries," *Electrochimica Acta,* vol. 55, pp. 3026-3033, Mar 1 2010.

[129] G. F. Yang, J. S. Song, H. Y. Kim, and S. K. Joo, "Metal Foam as Positive Electrode Current Collector for LiFePO4-Based Li-Ion Battery," *Japanese Journal of Applied Physics,* vol. 52, Oct 2013.

[130] Q. N. Sa and Y. Wang, "Ni foam as the current collector for high capacity C-Si composite electrode," *Journal of Power Sources,* vol. 208, pp. 46-51, Jun 15 2012.

[131] X. Y. Fan, F. S. Ke, G. Z. Wei, L. Huang, and S. G. Sun, "Sn-Co alloy anode using porous Cu as current collector for lithium ion battery," *Journal of Alloys and Compounds,* vol. 476, pp. 70-73, May 12 2009.

[132] W. Xu, N. L. Canfield, D. Y. Wang, J. Xiao, Z. M. Nie, X. A. H. S. Li, W. D. Bennett, C. C. Bonham, and J. G. Zhang, "An Approach to Make Macroporous Metal Sheets as Current Collectors for Lithium-Ion Batteries," *Journal of the Electrochemical Society,* vol. 157, pp. A765-A769, 2010.

[133] M. Pharr, Z. G. Suo, and J. J. Vlassak, "Measurements of the Fracture Energy of Lithiated Silicon Electrodes of Li-Ion Batteries," *Nano Letters,* vol. 13, pp. 5570-5577, Nov 2013.

[134] A. Li, V. Ji, J. L. Lebrun, and G. Ingelbert, "Surface-Roughness Effects on Stress Determination by the X-Ray-Diffraction Method," *Experimental Techniques,* vol. 19, pp. 9-11, Mar-Apr 1995.

[135] O. Ergincan, G. Palasantzas, and B. J. Kooi, "Influence of random roughness on cantilever curvature sensitivity (vol 96, 041912, 2010)," *Applied Physics Letters,* vol. 96, May 31 2010.

[136] Q. Y. Li and K. S. Kim, "Micromechanics of friction: effects of nanometre-scale roughness," *Proceedings of the Royal Society a-Mathematical Physical and Engineering Sciences,* vol. 464, pp. 1319-1343, May 8 2008.

[137] M. S. Hu and A. G. Evans, "The Cracking and Decohesion of Thin-Films on Ductile Substrates," *Acta Metallurgica,* vol. 37, pp. 917-925, Mar 1989.

[138] R. W. Carpick, N. Agrait, D. F. Ogletree, and M. Salmeron, "Variation of the

interfacial shear strength and adhesion of a nanometer-sized contact," *Langmuir,* vol. 12, pp. 3334-3340, Jun 26 1996.

[139] K. J. Frutschy and R. J. Clifton, "High-temperature pressure-shear plate impact experiments on OFHC copper," *Journal of the Mechanics and Physics of Solids*, vol. 46, pp. 1723-1743, Oct 1998.

[140] J. L. Beuth, "Cracking of Thin Bonded Films in Residual Tension," *International Journal of Solids and Structures,* vol. 29, pp. 1657-1675, 1992.

[141] R. Ballarini, R. L. Mullen, Y. Yin, H. Kahn, S. Stemmer, and A. H. Heuer, "The fracture toughness of polysilicon microdevices: A first report," *Journal of Materials Research,* vol. 12, pp. 915-922, Apr 1997.

[142] M. S. Hu, M. D. Thouless, and A. G. Evans, "The Decohesion of Thin-Films from Brittle Substrates," *Acta Metallurgica,* vol. 36, pp. 1301-1307, May 1988.

[143] S. K. Soni, B. W. Sheldon, X. C. Xiao, A. F. Bower, and M. W. Verbrugge, "Diffusion Mediated Lithiation Stresses in Si Thin Film Electrodes," *Journal of the Electrochemical Society,* vol. 159, pp. A1520-A1527, 2012.

[144] R. C. de Guzman, J. H. Yang, M. Ming-Cheng, S. O. Salley, and K. Y. S. Ng, "A silicon nanoparticle/reduced graphene oxide composite anode with excellent nanoparticle dispersion to improve lithium ion battery performance," *Journal of Materials Science*, vol. 48, pp. 4823-4833, Jul 2013.

ABSTRACT

DEVELOPMENT OF SILICON-BASED ANODES AND IN-SITU CHARACTERIZATION TECHNIQUES FOR LITHIUM ION BATTERIES

by

JINHO YANG

August 2014

Advisor: Dr. Mark Ming-Cheng Cheng

Major: Electrical Engineering

Degree: Doctor of Philosophy

Development of lithium ion batteries (LIBs) with higher capacity has been booming worldwide, as growing concerns about environmental issues and increasing petroleum costs. The demands for the LIBs include high energy and power densities, and better cyclic stability in order to meet a wide range of applications, such as portable devices and electric vehicles. Silicon has recently been explored as a promising anode material due to its low discharge potential (<0.4 V) and high specific capacity (4200 mAh g^{-1}). The capacity of silicon potentially exceeds more than 10 times of the conventional graphite anode (372 mAh g^{-1}). However, the silicon anode experiences huge volume expansion (400%) and contraction during electrochemical cycles, resulting in pulverization and disintegration of the active material. For the improvement of the battery performance, understanding of the failure mechanism associated with the stress evolution during cycling is critical.

This study aims (1) to develop high performance anode materials and (2) to analyze the mechanism of the capacity fading using a novel in-situ characterization technique in order to optimize the electrode design for better operation of the battery. The silicon nitride thin film anodes were investigated for the improvement of cycling performance. In addition, the

rate performance was enhanced by controlling the parameters in film deposition. Si-based thin films undergo large stresses induced by the volume changes, which results in material degradation and capacity fading. Hence, the in-situ measurement of the electrochemical processes is critical to clarify how the electrode degrades with time under cycling. For the in-situ measurement, a white light interferometry (WLI) and laser vibrometer were used to gather quantitative data. Amorphous silicon (*a*-Si) was explored for the stress measurement.

AUTOBIOGRAPHICAL STATEMENT

JINHO YANG

Education:

2010~2014 Doctor of Philosophy, Wayne State University, Detroit, MI, USA

2008~2010 Master Degree in Engineering, Ajou University, Suwon, S. Korea

2006~2008 Bachelor Degree in Engineering, Ajou University, Suwon, S. Korea

2003~2005 Associate of Art in Mathematics, Santa Rosa Junior College, Santa Rosa, CA, USA

Selected Journal Publications

1. Yang, J.; de Guzman, R.; Salley, S.; Ng, S.; Cheng, M., PLASMA ENHANCED VAPOR DEPOSITION SILICON NITRIDE FOR A HIGH-PERFORMANCE LITHIUM ION BATTERY ANODE. Journal of Power Sources, 2014
2. de Guzman, R.; Yang, J.; Cheng, M.; Salley, S.; Ng, S., HIGH CAPACITY SILICON NITRIDE-BASED COMPOSITE ANODE FOR LITHIUM ION BATTERIES. Journal of Materials Chemistry A, 2014.
3. de Guzman, R.; Yang, J.; Cheng, M.; Salley, S.; Ng, S., EFFECTS OF GRAPHENE AND CARBON MODIFICATIONS ON ELECTROCHEMICAL PERFORMANCE OF SILICON NANOPARTICLE/GRAPHENE COMPOSITE ANODE. Journal of Power Sources, 2014.
4. Yoon H.; Jun D.; Yang J.; Zhou Z.; Yang S.; Cheng M., CARBON DIOXIDE GAS SENSOR USING A GRAPHENE SHEET. Sensors and Actuators B, 2011.